MODIFIED TITANIUM DIOXIDE FOR WATER DETOXIFICATION AND DISINFECTION

DOU HAIQING

NATIONAL UNIVERSITY OF SINGAPORE

2011

MODIFIED TITANIUM DIOXIDE FOR WATER DETOXIFICATION AND DISINFECTION

DOU HAIQING

(B.Eng, XJTU)

A THESIS SUBMITTED

FOR THE DEGREE OF MASTER OF ENGINEERING

DEPARTMENT OF CHEMICAL AND BIOMOLECULAR ENGINEERING

NATIONAL UNIVERSITY OF SINGAPORE

2011

Acknowledgement

It is a pleasant aspect that now I have the opportunity to express my deep gratitude to all of the people who have assisted me throughout the whole length of my Master candidature.

First and foremost, I would like to convey my very special thanks to my supervisor, Assoc. Prof. Zhao X. S., George, who has provided me with invaluable guidance, continuous encouragement, patience and understanding during the past three years. This thesis project has been a tough but enriching experience for me in research. I would like to express my heartfelt thanks to Prof. Zhao for his guidance on writing this Master thesis.

I also would like to thank all my group members for their assistance, suggestions, and insightful discussions. It's my pleasure to work with a group of brilliant, warm-hearted and lovely people, Dr. Lv Lu, Dr. Bai Peng, Dr. Wang Likui, Dr. Lee Fang Yin, Dr. Tian Xiaoning, Dr. Liu Jiajia, Ms. Zhang Li Li, Ms. Wu Pingping, Mr. Cai Zhongyu, Mr. Zhang Jintao, Dr. Lei Zhibin, Dr. Pan Jia Hong, Dr. Xiong Zhigang, Ms. Ma Jizhen, Mr. Wan Yong, Mr. Xu Chen, Dr. Luo Yiqun, Ms. Han Su Mar, Mr. Han Gang, Mr. Yu Yong, Dr. Nikolay Christov, Mr. Zhou Rui, Ms. Zhao Shanyu, Ms. Hoang Do Quyen and Mr. Fan Haitao.

My sincere appreciation also goes to the Department of Chemical and Biomolecular Engineering for offering me the research scholarship, and all the laboratory and administrative staffs, especially Ms. Wan Foon Kiew Sylvia, Ms. Siew Woon Chee Jamie, Mr. Chia Phai Ann, Dr. Yuan Ze Liang, Mr. Mao Ning, Mr. Liu Zhicheng, Ms. Fam Hwee Koong Samantha, Ms. Tay Kai Si Alyssa, Ms. Xu Yanfang,

Mr. Ang Wee Siong, Mr. Boey Kok Hong, Mr. Chan Chuin Mun Alistair and Ms. How Yoke Leng Doris.

Finally, I want to thank my beloved parents, my fiancée, Chen Xiang, younger sisters and my friends. It is no exaggeration to say that I could not complete my Master work without their generous help, boundless love, encouragement and support.

Table of Contents

Acknowledgement I

Table of Contents III

Summary VII

Nomenclature VIII

List of Tables X

List of Figures XI

CHAPTER 1 INTRODUCTION 1

1.1 Background 1

1.2 Semiconductor photocatalysis for water detoxification and disinfection 3

1.3 Objectives of the project 9

1.4 Structure of thesis 10

CHAPTER 2 LITERATURE REVIEW 11

2.1 Modification of pristine TiO_2 11

2.1.1 Phase junction effect of bi-crystalline TiO_2 12

2.1.2 Synthesis of traditional bi-crystalline TiO_2 photocatalyst 13

2.1.3 Novel bi-crystalline anatase-TiO_2(B) photocatalysts 16

2.2 Modifying TiO_2 photocatalysts by doping strategies or depositing noble metal nanoparticles 17

2.2.1 Doped TiO_2 photocatalysts 18

2.2.2 Noble metal-TiO_2 composite photocatalysts 22

2.3 Porous TiO_2-based photocatalysts 28

2.3.1 Template methods 28

2.3.2 Self-organization of nanobuilding blocks.....33

2.3.3 Etching route to hollow structures under hydrothermal conditions.....36

2.3.4 Topotactic transition 37

2.3.5 Porous industrial photocatalysts 39

2.4 Novel TiO_2-Graphene nanocomposite photocatalysts.....45

CHAPTER 3 EXPERIMENTAL SECTION.....48

3.1 Reagents and apparatus.....48

3.2 Synthesis route of modified TiO_2-based photocatalysts.....50

3.2.1 Hydrothermal synthesis of mesoporous tri-crystalline TiO_2 photocatalysts 50

3.2.2 One-pot hydrothermal synthesis of visible-light-activated TiO_2-Au nanotubes 51

3.3 Characterization.....51

3.3.1 Thermogravimetric analysis (TGA).....51

3.3.2 X-ray diffraction (XRD) 52

3.3.3 Physical adsorption of N_2 52

3.3.4 Field-emission scanning electron microscope (FESEM).....53

3.3.5 Transmission electron microscope (TEM).....53

3.3.6 X-ray photoelectron spectroscopy (XPS) 53

3.3.7 Diffusive reflectance UV-Vis spectrophotometer (DR-UV) 54

3.4 Evaluation of photocatalytic activity and antibacterial property 54

3.4.1 Semi-batch swirl flow reactor.....54

3.4.2 SGY-II Photoreactor: Open thermostatic batch reactor.....56

3.4.3 Recycle test.....56

3.4.4 Evaluation of photocatalytic antibacterial property.....57

CHAPTER 4 SYNTHESIS, CHARACTERIZATION AND HIGHLY PHOTOCATALYTIC PERFORMANCE OF MESOPOROUS TRI-CRYSTALLINE TiO_2 58

4.1 Introduction 58

4.2 Characterization and photocatalytic activity of mesoporous tri-crystalline TiO_2 61

4.2.1 TGA investigation 61

4.2.2 N_2 adsorption/desorption analysis 62

4.2.3 X-ray Diffraction results 64

4.2.4 FESEM and TEM investigation 66

4.2.5 XPS results 67

4.2.6 Photocatalytic properties under UV light irradiation 69

4.3 Parameters affecting the phase content 71

4.3.1 The effect of urea and other additive (TTEA) 71

4.3.2 The effect of $TiCl_4$ 75

4.3.3 The effect of calcination temperature 77

4.4 Discussion of mesoporous tri-crystalline TiO_2 photocatalysts 81

4.4.1 Synthesis route and evolution of phase composition 81

4.4.2 The mechanism of photocatalytic degradation of Orange II 82

4.4.3 The relationship between the phase content and photocatalytic activity 85

4.5 Summary 88

CHAPTER 5 ONE-POT FABRICATION AND CHARACTERIZATION OF TiO_2–Au NANOTUBES WITH VISIBLE-LIGHT-RESPONSE 89

5.1 Introduction 89

5.2 Characterization and photocatalytic activity of TiO_2-Au nanotubes 92

5.2.1 Morphology of samples 92

5.2.2 N_2 adsorption/desorption analysis 92

5.2.3 X-ray Diffraction results 95

5.2.4 XPS results 97

5.2.5 Optical property 99

5.2.6 Photocatalytic degradation of azo dyes under visible light irradiation 101

5.2.7 Photocatalytic antibacterial activity under visible light irradiation 103

5.2.8 Separation and cyclic usage test 105

5.3 Summary 108

CHAPTER 6 CONCLUSIONS AND RECOMMENDATIONS 109

6.1 Conclusions 109

6.2 Recommendations 110

REFERENCES 112

APPENDIX 129

Summary

Among various wastewater treatment technologies, semiconductor photocatalysis is gaining increasing attention because of its many unique features, such as its capability of achieving a complete mineralization of organic wastes, easy operation, and environmentally friendly process. Titanium dioxide (TiO_2) is the most widely studied semiconductor photocatalyst for wastewater treatment.

However, there are a couple of problems associated with TiO_2 photocatalysts. First, the large energy bandgap of TiO_2 requires ultraviolet (UV) light to activate it, resulting in a low energy efficiency and high cost. Second, the high recombination rate of the photo-generated electrons and holes leads to a poor photocatalytic efficiency of the process. Third, the non-porous nature of commercially available TiO_2 determines its low surface area for adsorption of organic pollutants, thus low photocatalytic efficiency.

In this thesis work, several methods were used to modify TiO_2 photocatalysts with a primary objective of enhancing its photocatalytic performance under UV light irradiation or developing visible-light-responsive TiO_2-based photocatalysts. The results showed that the mesoporous tri-crystalline TiO_2 photocatalysts with tuneable phase compositions, fabricated by a simple soft-template method, displayed a high photocatalytic activity towards oxidation of Orange II, a non-biodegradable synthetic dye, under UV light irradiation. Besides, a facile one-pot hydrothermal synthesis route under strong basic environment was developed to synthesize Au-loaded TiO_2 nanotubes with enhanced visible light absorption capability as well as better photocatalytic performance towards oxidation of Orange II dye and killing *E.Coli* under visible light illumination.

Nomenclature

AOPs	Advanced Oxidation Processes
BET	Brunauer-Emmett-Teller
C	Concentration (mg/L)
CNTs	Carbon Nanotubes
C_0	Initial concentration (mg/L)
D	Dimensional
DR-UV	Diffusive Reflectance UV-Vis
DT	Dodecyl amine
e^-	Electron
eV	Electron Volt
E_{bg}	Bandgap energy (eV)
EISA	Evaporation-Induced Self-Assembly
FESEM	Field Emission Scanning Electron Microscopy
FWHM	Full Width at Half Maximum
G	Graphene
GO	Graphene oxide
GR	Reduced graphene oxide
h^+	Hole
I_A	Intensity of anatase peak
I_B	Intensity of brookite peak
I_R	Intensity of rutile peak
k	Rate constant
K	Langmuir adsorption constant (L/mol)
K_{app}	Kinetic parameter of photoreaction (h^{-1})
MCM-41	Mobil Composite matters of number 41

mL	Mille liter
NHE	Normal Hydrogen Electrode
NPs	Nanoparticles
NTs	Nanotubes
P25	a commercial product of titanium dioxide (TiO_2) from Degussa
r	Initial rate of photooxidation
s	Weight of urea
S_{BET}	BET surface area (m^2/g)
SBA-15	Silica with hexagonal pore structure (Santa Barbara recipe)
SC	Supercritical water
SEM	Scanning Electron Microscopy
t	Time (min or h)
TEM	Transmission Electron Microscopy
TGA	Thermogravimetric analysis
TOC	Total Organic Carbons
TTEA	Tetraethylammonium hydroxide
TTIP	Titanium tetraisopropoxide
UV	Ultraviolet
UV/Vis	Ultraviolet Visible
w	Weight
x%	Molar ratio of Au/Ti
XPS	X-Ray Photoelectron Spectroscopy
XRD	X-ray Diffraction
λ_{bg}	Threshold wavelength of a photon (nm)

List of Tables

Chapter 3

Table 3.1 Reagents used for synthesis of TiO_2-based photocatalysts

Table 3.2 Apparatus used in this master thesis project

Chapter 4

Table 4.1 Preparation conditions of TiO_2 photocatalysts involved in this work

Table 4.2 Textural and structural parameters of TiO_2-s (s=0-5)

Table 4.3 Weight fractions of each phase in tri-crystalline or bi-crystalline samples TiO_2-s (s=0-5)

Table 4.4 Atomic concentration data of the samples TiO_2-s (s=0-5)

Table 4.5 Comparison of weight fraction in TiO_2-TT, TiO_2-Ur-TT and TiO_2-0

Table 4.6 Textural and structural parameters of TiO_2-TT and TiO_2-Ur-TT

Table 4.7 Textural and structural parameters of TiO_2-2 (450) and TiO_2-2 (550)

Table 4.8 Comparison of weight fraction in TiO_2-2 (350), TiO_2-2 (450) and TiO_2-2 (550)

Chapter 5

Table 5.1 Textural and structural parameters of $H_2Ti_3O_7$ NTs, $H_2Ti_3O_7$-Au-0.5% NTs and TiO_2-Au-*x*% NTs

Table 5.2 Phase compositions TiO_2(B)/anatase of TiO_2-Au-*x*% NTs

List of Figures

Chapter 1

Figure 1.1 Membrane bioreactor treatment systems for direct conversion to portable water (Shannon et al., 2008).

Figure 1.2 Band positions of several semiconductors in contact with aqueous electrolyte at pH=1 (Grätzelare, 2001).

Figure 1.3 Schematic photoexcitation in a solid followed by deexcitation events (Linsebigler et al., 1995).

Figure 1.4 A schematic illustration of the generation of electron-hole pairs and the corresponding redox reactions taking place on the semiconductor surface when illuminated with appropriate wavelength of light (Palmisano and Sclafani, 1997).

Chapter 2

Figure 2.1 Representations of the TiO_2 anatase, rutile, and brookite forms (Dambournet et al., 2010).

Figure 2.2 Dependence of the bulk rutile content and surface anatase content on the calcination temperature (Zhang et al., 2008a).

Figure 2.3 (a) Photocatalytic decomposition of the organic dye sulforhodamine B (SRB) with different fibril Anatase/TiO_2(B) photocatalysts under UV irradiation; (b) possible electron-hole separation mechanism of mixed-phase nanofibers during photocatalysis driven by UV light illumination (Yang et al., 2009).

Figure 2.4 (A) Optical absorption spectra of $TiO_{2-x}N_x$ and TiO_2; (B) CO_2 evolution as a function of irradiation time (light on at zero) during the photodegradation of acetaldehyde gas under UV light and visible light over $TiO_{2-x}N_x$ (solid circles) and pristine TiO_2 (open squares), respectively (Asahi et al., 2001).

Figure 2.5 Various schemes illustrating the possible changes that might occur to the band gap electronic structure of anatase TiO_2 on doping with various non-metallic elements (Serpone, 2006).

Figure 2.6 Photoinduced charge separation and storage in Ag/TiO_2 core-shell structure (Hirakawa and Kamat, 2004).

Figure 2.7 (a) SEM image of the Au/TiO_2 precursor before hydrothermal treatment. (b-d) SEM, TEM and Au size distribution pattern of the Au/TiO_2. The insets are the TEM and SAED images (Bian et al., 2009).

Figure 2.8 Schematic diagram of the in-situ route to deposit noble metal nanoparticles onto TiO_2 and the TEM image of Pt-TiO_2 (Xie et al., 2009).

Figure 2.9 Upper: A scheme illustrating the synchronous assembly of titanate oligomers due to the hydrolysis of titanium isopropoxide (TIPO) and silicate species because of the hydrolysis of tetraethyl orthosilicate (TEOS) in the presence of P123 template to form a highly ordered mesoporous TiO_2-SiO_2 composite; TEM (a) and HRTEM (b-d) images of ordered 2D hexagonal mesoporous TiO_2-SiO_2 composite calcined at 700 °C for 4 h (a-c) and at 800 °C for 2 h (d) (Dong et al., 2007).

Figure 2.10 Schematic diagram of CASH method (Lee et al., 2008).

Figure 2.11 Schematic illustration of the formation of hierarchical rutile TiO_2 nanoarchitectures (top); SEM image (a) of TiO_2 microspheres consisting of rutile nanorods synthesized in water-chloroform emulsions; HRTEM image (b) of a single rutile nanorod as well as its 2D Fourier transform pattern (inset) (Xu et al., 2007).

Figure 2.12 SEM (a) and TEM (b) images for hierarchically mesoporous F-TiO_2 hollow microspheres; insert of (a): magnified corresponding to (a); Methyl blue (MB) and TOC removal (c), and membrane flux (d) over mesoporous F-TiO_2 hollow microspheres and Degussa P25. Insert of (d): Schematic diagram of membrane fouling caused by photocatalysts (Pan et al., 2008).

Figure 2.13 TEM (a) and radial and axial cross-sectional HRTEM images (b) of TiO_2 nanotubes synthesized via an alkaline hydrothermal treatment of anatase TiO_2 in 10 M NaOH solution at 120-140^{o}C (Bavykin et al., 2004).

Figure 2.14 (a) SEM micrograph and (b) TEM micrograph of P25 adsorbed on sepiolites fibers, scale bar in (b) is 100 nm ; Plot representing (c) PNP concentration and (d) MB concentration versus irradiation time in solutions containing pristine P25 or SS-P25 composites (Nieto-Suarez et al., 2009).

Figure 2.15 (a) Typical TEM image of P25-GR; (b) Schematic structure of P25-GR and tentative processes of the photodegradation of methylene blue (MB) over P25-GR; Photodegradation of methylene blue under (c) UV light and (d) visible light (λ>400 nm) over (1) P25, (2) P25-CNTs, and (3) P25-GR photocatalysts, respectively (Zhang et al., 2010).

Chapter 3

Figure 3.1 Schematic diagram of the photodegradation experimental set-up I: Semi-batch swirl flow reactor.

Chapter 4

Figure 4.1 TGA spectrum of TiO_2-0.

Figure 4.2 (a-f) Nitrogen adsorption-desorption isotherms and corresponding BJH pore size distribution curves (inset) of TiO_2-s (s=0-5).

Figure 4.3 Wide-angle X-Ray diffraction patterns of TiO_2-s (s=0-5).

Figure 4.4 FESEM image (A), TEM image (B), HRTEM (C) and selected area electron diffraction pattern (D) of the sample TiO_2-2.

Figure 4.5 Broad-scan XPS spectra and narrow-scan N1s XPS spectra (inset) obtained for TiO_2-0.

Figure 4.6 Photocatalytic degradation of Orange II over TiO_2-2 with time under UV irradiation (Phillips, HPR 125 W, wavelength centered on 365nm). Experiment condition: semi-batch swirl flow reactor; light intensity: 110w/m^2; catalyst amount: 0.6 g/L; initial concentration of orange II: 20 mg/L.

Figure 4.7 Comparison of the Orange II photodegradation activity over TiO_2-s (s=0-5). Experiment condition: semi-batch swirl flow reactor; light intensity: 110w/m^2; catalyst amount: 0.6 g/L; initial concentration of orange II: 20 mg/L.

Figure 4.8 Wide-angle XRD patterns of (a) TiO_2-0, (b) TiO_2-Ur-TT, and (c) TiO_2-TT.

Figure 4.9 Nitrogen adsorption-desorption isotherms and corresponding BJH pore size distribution curves (inset) of (a) TiO_2-TT and (b) TiO_2-Ur-TT.

Figure 4.10 XRD pattern of TiO_2-6 (No $TiCl_4$).

Figure 4.11 Nitrogen adsorption-desorption isotherm and corresponding BJH pore size distribution curves (inset) of of TiO_2-6 (No $TiCl_4$).

Figure 4.12 Nitrogen adsorption-desorption isotherms and corresponding BJH pore size distribution curves (inset) of (a) TiO_2-2 (450) and (b) TiO_2-2 (550).

Figure 4.13 XRD patterns of TiO_2-2 (350), TiO_2-2 (450) and TiO_2-2 (550).

Figure 4.14 Comparison of the Orange II photodegradation activity over TiO_2-2 (350), TiO_2-2 (450) and TiO_2-2 (550). Experiment condition: semi-batch swirl flow reactor; light intensity: 110w/m^2; catalyst amount: 0.6 g/L; initial concentration of orange II: 20 mg/L.

Figure 4.15 Chemical structure of Orange II (Bhattacharyya et al., 2004).

Figure 4.16 Comparison of photocatalytic degradation and TOC degradation of orange II over TiO_2-2. Experiment condition: semi-batch swirl flow reactor; light intensity: 110w/m^2; catalyst amount: 0.6 g/L; initial concentration of orange II: 20 mg/L.

Figure 4.17 Variation in K_{app} as a function of anatase weight percentage and (inset) variation in the residual Orange II concentration as a function of UV-radiation exposure time for several samples.

Figure 4.18 DR absorbance spectra obtained for the samples TiO_2-s (s=0-5) and (inset) enlarged view of highlighted rectangle.

Chapter 5

Figure 5.1 TEM images of TiO_2-Au-0.5% nanotubular photocatalyst.

Figure 5.2 Nitrogen adsorption-desorption isotherms and corresponding BJH pore size distribution curves (inset) of (a) $H_2Ti_3O_7$ NTs, (b) $H_2Ti_3O_7$-Au-0.5% NTs and (c-h) TiO_2-Au-*x*% NTs (x=0, 0.05, 0.1, 0.25, 0.5 and 1).

Figure 5.3 XRD patterns of (a) $H_2Ti_3O_7$- Au-0.5% NTs, (b) pure TiO_2 NTs, (c) TiO_2-Au-0.05% NTs, (d) TiO_2-Au-0.1% NTs, (e) TiO_2-Au-0.25% NTs, (f) TiO_2-Au-0.5% NTs, (g) TiO_2-Au-1% NTs.

Figure 5.4 (a) Broad-scan XPS spectra and (b) high-resolution XPS spectra of Au 4f for the resulted TiO_2-Au-1% nanotubular photocatalyst.

Figure 5.5 Comparison of DR absorbance spectra of (a) TiO_2 NTs, $H_2Ti_3O_7$ NTs TiO_2-Au-0.05% NTs, and $H_2Ti_3O_7$-Au-0.05% NTs, and (b) TiO_2-Au-*x*% NTs (x=0, 0.05, 0.1, 0.25 and 0.5).

Figure 5.6 Comparison of the photocatalytic activity over TiO_2-Au-*x*% NTs towards oxidation of Orange II. Experiment condition: batch reactor; light source: 350W Xenon light equipped with a 420nm cut-off filter; catalyst amount: 1 g/L; initial concentration of Orange II: 5 ppm.

Figure 5.7 Effect of Au loading on the photocatalytic degradation of Orange II in aqueous solution.

Figure 5.8 Photocatalytic inactivation of *E.coli* in solution containing (a) no catalyst, (b) TiO_2 NTs, and (c) TiO_2-Au-0.25% NTs under visible light irradiation. Experiment condition: batch reactor; light source: 350W Xenon light equipped with a 420nm cut-off filter; photocatalyst amount: 0.025g; initial concentration of *E.coli*: 10^8-10^9 CFU/mL.

Figure 5.9 Sedimentation test of water solution containing photocatalysts TiO_2-Au-0.25% NTs, TiO_2 NTs and Degussa P25 at (a) t = 0 h and (b) t = 5h.

Figure 5.10 Cyclic usage experiments for photo-degradation of Orange II over TiO_2-Au-0.25% NTs under visible light illumination. Experiment condition: batch reactor; light source: 350W Xenon light equipped with a 420nm cut-off filter; catalyst amount: 1 g/L; initial concentration of Orange II: 5 ppm.

CHAPTER 1

INTRODUCTION

1.1 Background

Water is the source of life and every human being needs a regular supply of drinking water in order to survive. In recent years, people in the whole world are suffering from increasingly serious environmental pollution and the lack of sufficient clean drinking water. Due to the rapid urban and industrial development, on one hand, the increasing population of the world demands more and more clean water resources. On the other hand, large quantities of water are consumed by various industries while toxic organic effluents and other contaminants are released to the rivers, lakes and groundwater. Particularly seriously, e.g., microbial contaminations (bacteria, virus, pathogenic microorganisms and so on) in the unsafe drinking water causes millions of peoples die annually-3,900 children a day (Shannon et al., 2008).

Although traditional methods used for water purification, e.g. chemical degradation, achieved some of success, they cannot completely accomplish the purpose of removing all the organic pollutants and killing all the microbial contaminations. Therefore, it is of much concern to seek for and establish more efficient and robust water purification methods with low cost and less energy.

Fortunately, a flurry of recent fruitful research offers hope in completely solving the problems mentioned above. For example, the water purification system shown in Figure 1.1, which consists of ultrafiltration (UF), reverse osmosis (RO) and ultraviolet (UV) disinfection, can produce potable use water and gains industrial application (as can be seen in the NEWater Plant in Singapore).

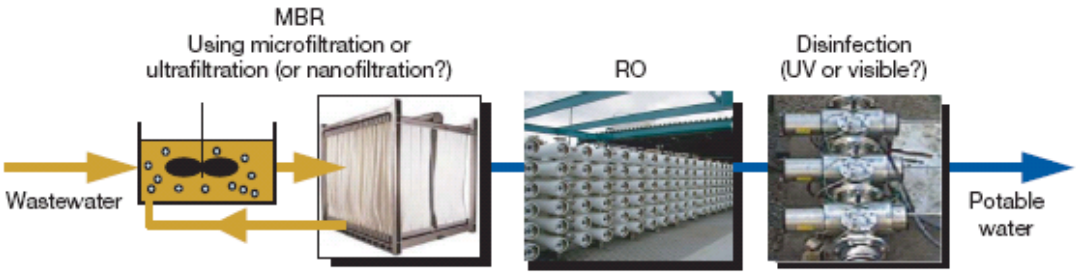

Figure 1.1 Membrane bioreactor treatment systems for direct conversion to portable water (Shannon et al., 2008).

UV disinfection is gaining popularity as shown in Figure 1.1 because of its many advantages over other technologies. Firstly, it can penetrate the cell wall of microorganisms, leading to break up of the C=C carbon bond of the microorganism components, thus causing cellular death and rendering the growing and multiplying of microorganism (Oguma et al., 2002). Secondly, it is easy to install and operate, without producing any unwanted disinfection byproducts (DBPs). However, a serious problem with UV disinfection is that the time of UV irradiation is very short in the industry and cannot inactive emerging viruses, spores, and cysts completely (Butkus et al. 2005), and the re-activation of some inactivated organisms may occur sometimes. Besides, if the time of UV irradiation is prolonged, then the cost will increase significantly. Thus it is wise to develop advanced oxidation processes (AOP), which successfully combine light energy (e.g. UV light) and other efficient techniques e.g H_2O_2, O_3, TiO_2 (also known as semiconductor photocatalysis) and so on, to completely remove all the toxic organic pollutants.

Since the discovery of the photo-splitting of water into H_2 and O_2 on the TiO_2 electrode by Honda and Fujishima in 1972 (Fujishima and Honda, 1972), photocatalysis by TiO_2 and others semiconductors has been widely investigated in order to efficiently convert light energy (UV or solar energy) into reliable chemical energy. Then the environmental applications, such as removal of highly toxic and

non-biodegradable organic pollutants, killing the bacterial and virus in the wastewater and so on, have attracted the most attention among all its potential applications in the past several decades (Hoffmann et al., 1995; Gayaa and Abdullah, 2008).

1.2 Semiconductor photocatalysis for water detoxification and disinfection

1.2.1 Semiconductor photocatalysis and photocatalysts

Photocatalysis refers to the catalytic reactions, in which the catalysts are activated by light rather than by heat. Therefore, light irradiation and catalysts (semiconductors) are two prerequisites. Unlike metals, semiconductors possess unique electronic structures, which make them suitable candidates for photocatalysis. In semiconductors, the term "band gap energy" (E_{bg}, the band gap positions of some semiconductors are shown in Figure 1.2) is defined as the energy differences between the top of the valence band (green colour in Figure 1.2), which is occupied by electron, and the bottom of the conduction band (red colour in Figure 1.2), which is unoccupied. The electron can achieve transition from valence band to conduction band by absorbing either a phonon (heat) or a photon (light) with the energy equal to or larger than the band gap energy E_{bg}. Thus the threshold wavelength of light irradiation, λ_{bg}, can be expressed according to the equation

$$\lambda_{bg}(nm) = 1240 / E_{bg}(eV) \tag{1.1}$$

where λ_{bg} is the threshold wavelength of a photon.

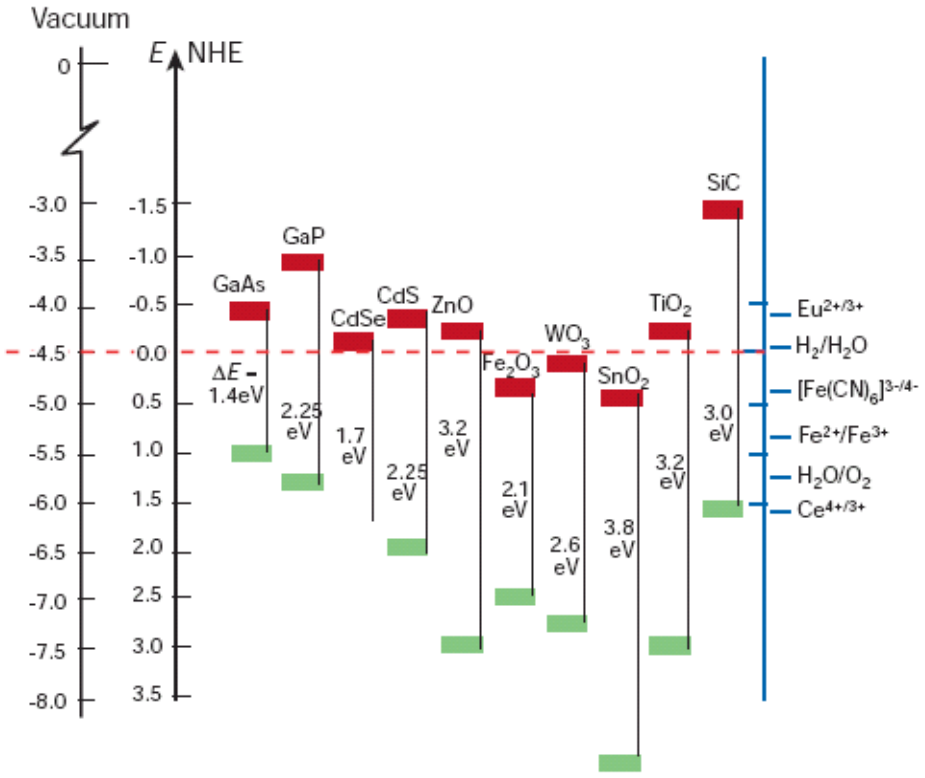

Figure 1.2 Band positions of several semiconductors in contact with aqueous electrolyte at pH=1 (Grätzelare, 2001).

Yates' group (Linsebigler et al., 1995) offered a description of photoexcitation in a solid semiconductor in detail, as illustrated in Figure 1.3. Upon excitation by light irradiation, the electrons will be transferred to the conduction band, leaving holes in the valence band, generating the electron-hole pairs, which have sufficient time and will move to the surface.

$$TiO_2 + hv(\geq E_{bg}) \rightarrow e^- + h^+ \qquad (1.2)$$

There are four possible deexcitation pathways for the separated electron and holes. On the surface, the semiconductor can donate electrons to reduce the electron acceptor (Figure 1.3, Pathway C). When a hole migrates to the surface, it may accept an electron from electron donors, causing oxidation of the donor species (Figure 1.3, Pathway D). In competition with charge transfer to adsorbed species is electron and

hole recombination with release of heat. Pathway A and B (Figure 1.3) refer to the recombination on the surface and in the bulk phase of the semiconductors, respectively.

$$e^- + h^+ \rightarrow heat \tag{1.3}$$

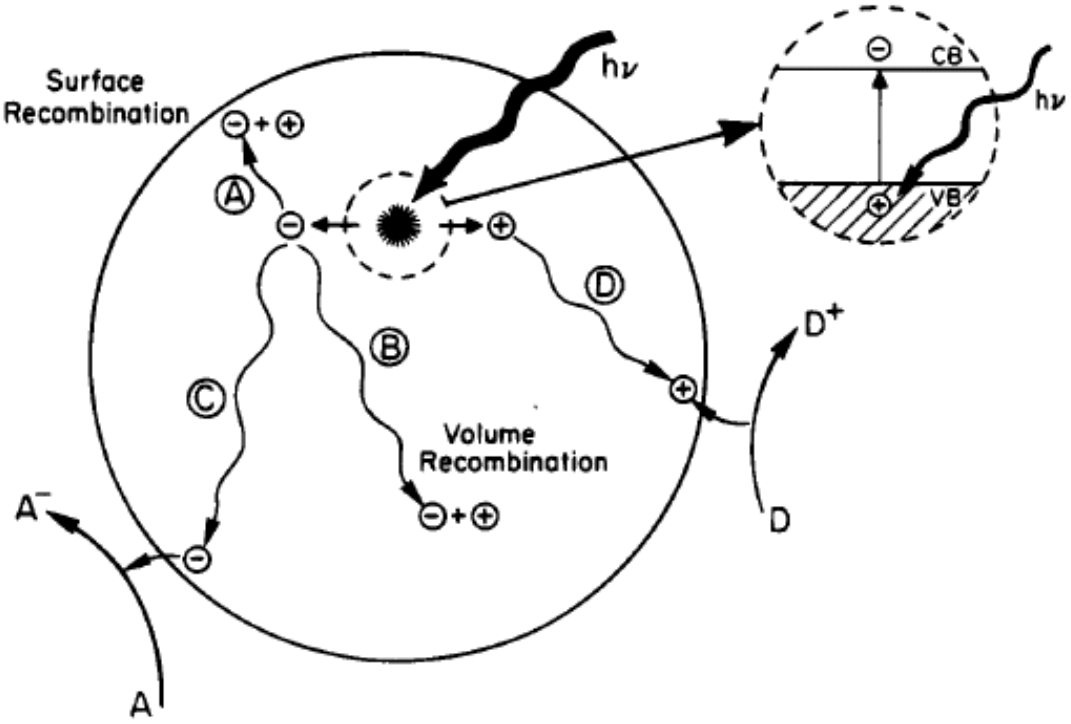

Figure 1.3 Schematic photoexcitation in a solid followed by deexcitation events (Linsebigler et al., 1995).

1.2.2 Titanium dioxide photocatalysts

Of various semiconductor photocatalysts shown in Figure 1.2, TiO_2 is believed to be the best candidate for environmental applications, especially water purification, due to its many desirable properties. It is very cheap, long-term biologically and chemically stable, nontoxic and highly efficient, which can be used for photo-oxidation and removal of a wide range of organic contaminants (Hoffmann et al., 1995; Gayaa and Abdullah, 2008).

1.2.3 Mechanism of TiO_2-assited photocatalytic degradation

In principle, a photocatalytic reaction proceeds on the surface of a semiconductor (e.g. TiO_2) via several steps as illustrated in Figure 1.4. The initial process for heterogeneous photocatalysis of organic compounds by TiO_2 is the generation of holes and electrons in the TiO_2 particles (Equation 1.2) when it is illuminated with appropriate wavelength of light (wavelength<385nm).

The holes and electrons are very important for photocatalytic degradation. If the combination of separated electrons and holes occurs (Equation 1.3), the photocatalysis efficiency will decrease significantly. However, this recombination process can be reduced greatly if the electrons and holes can be trapped by absorbed species and other sites on the surface. After a series of reaction listed below (Hoffmann et al., 1995; Gayaa and Abdullah, 2008), H_2O_2 and highly reactive radicals, such as $OH^{\bullet}$, $O_2^{\bullet}$ and so on, will generate.

$$e^- + O_2 \rightarrow O_2^- \quad (1.4)$$

$$h^+ + H_2O \rightarrow H^+ + OH^{\bullet} \quad (1.5)$$

$$2O_2^- + 2H^+ \rightarrow 2OH^{\bullet} + O_2 \quad (1.6)$$

$$O_2^- + H^+ \rightarrow HO_2^{\bullet} \quad (1.7)$$

$$H^+ + HO_2^{\bullet} \rightarrow H_2O_2 + h^+ \quad (1.8)$$

These reactive species can react with organic pollutants (Eqs1.9-1.12), forming CO_2 and H_2O completely (Figure 1.4).

$$OP(aq) \rightarrow OP^+(aq) + OP^-(aq) \quad \text{aqueous dissociation of organic pollutant} \quad (1.9)$$

$$OP^-(aq) + h^+ \rightarrow OP^{\bullet} \quad (1.10)$$

$$OP^{\bullet} + OH^{\bullet} / HO_2^{\bullet} \rightarrow M_n^{\bullet} \quad (1.11)$$

$$M_n^{\bullet} + OH^{\bullet} / HO_2^{\bullet} \rightarrow \cdots CO_2 + H_2O \quad (1.12)$$

where OP^+ and OP^- are organic cation and anion, respectively; and M_n are intermediates in the path to complete mineralization of the organic pollutants.

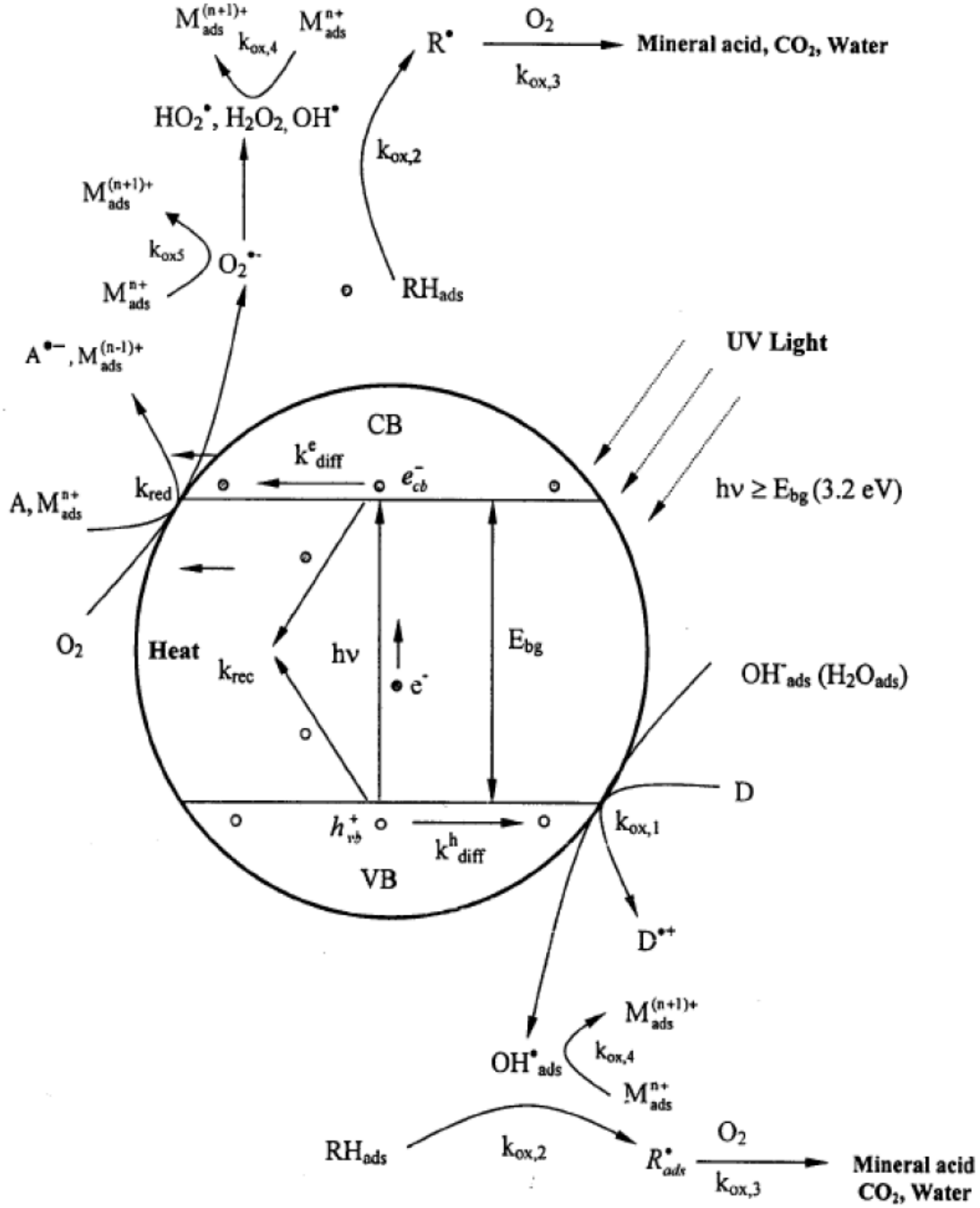

Figure 1.4 A schematic illustration of the generation of electron-hole pairs and the corresponding redox reactions taking place on the semiconductor surface when illuminated with appropriate wavelength of light (Palmisano and Sclafani, 1997).

1.2.4 Kinetics of TiO_2-assited photocatalytic degradation

Generally, the kinetic of TiO_2-assited photocatalytic degradation of organic waste follows a Langmuir-Hinshelwood modal (Herrmann, 1999; Gayaa and Abdullah, 2008)

$$r = -\frac{dC}{dt} = k(\frac{KC}{1+KC}) \tag{1.13}$$

where r is initial rate of photooxidation, C the concentration of organic waste, t the irradiation time, k the rate constant, and K is the adsorption coefficient of the organic compound.

For the dilute solution, $KC<<1$. Then the equation can be simplified to

$$r = -\frac{dC}{dt} = kKC \tag{1.14}$$

After integration, the relationship of C and t is obtained as following equation

$$\ln(\frac{C}{C_0}) = kKt = K_{app}t \tag{1.15}$$

Therefore, K_{app} is an important parameter to evaluate the photocatalytic performance of TiO_2-based photocatalysts.

1.2.5 Mechanism of TiO_2-assited photocatalytic disinfection

UV is employed to kill bacteria in the industry as mentioned above. It is very interesting that TiO_2 itself has been also found to exhibit antibacterial properties under UV light irradiation in the work published by Matsunaga and co-workers (1985). Recently, TiO_2-assited photocatalytic disinfection has attracted more and more

attention and gained great success. Meanwhile, three competing mechanisms are proposed in the literature and summarized as below (Page et al., 2009):

(1) Direct oxidation of coenzyme A (CoA), which inhibits cell respiration, ultimately leading to cell death;

(2) Cell wall decomposition and disorder in cell permeability;

(3) Cell wall damage followed by cytoplasmic membrane damage.

1.3 Objectives of the project

There are a couple of problems associated with TiO_2 photocatalysts although semiconductor photocatalysis has been widely accepted as a promising method to figure out the current problems in the wastewater treatment system. Firstly, the large energy band gap of TiO_2 requires ultraviolet (UV) light to activate it (Figure 1.3), largely inhibiting its overall efficiency under natural solar light, which consists of only 5% UV, 43% visible, and 52% infrared (Chen and Burda, 2008). Secondly, the high recombination rate of the photoinduced electrons and holes (Equation 1.3) leads to a poor photocatalytic efficiency of the process. Thirdly, the non-porous nature of commercially available TiO_2 determines its low surface area for adsorption of organic pollutants, thus low photocatalytic efficiency. Under such a background, the targets of this thesis work are aimed to:

- develop more efficient, stable and low-cost TiO_2-based photocatalysts under UV light by modification strategies, like metallic/non-metallic species doping method, porous TiO_2 and so on;
- explore efficient visible-light-activated TiO_2-based photocatalysts by doping/depositing strategy (e.g. Au nanoparticles depositing);

- evaluate and optimize the photocatalytic or antibacterial properties of the materials under UV light or visible light.

1.4 Structure of thesis

The thesis consists of six chapters. With a brief introduction to semiconductor photocatalysis and a summary of the objectives of this project in Chapter 1, an extensive literature review on the strategies how to develop more efficient or to explore visible-light-activated TiO_2-based photocatalysts is given in Chapter 2. The details of chemicals, experimental methods, conditions and characterization techniques used are provided in Chapter 3, followed by the main works of the thesis in Chapter 4 and 5. In Chapter 4, the synthesis of highly effective tri-crystalline mesoporous TiO_2 photocatalysts and the effects of experimental conditions on phase compositions and photocatalytic properties are discussed. Chapter 5 describes the one-pot hydrothermal fabrication and the visible-light photocatalytic performance of Au nanoparticles-loaded TiO_2 nanotubes composites (TiO_2-Au-*x*% NTs). Finally, conclusions of the present work and recommendations for future work are presented in Chapter 6.

CHAPTER 2

LITERATURE REVIEW

Highly efficient use of TiO_2 photocatalysts is now suffering from several problems as mentioned in Chapter 1. In recent years, a flurry of research interests have focused on improving the photocatalytic efficiency of TiO_2 photocatalyst by various modification methods, the design strategies of which can be roughly divided into three categories: (1) enhancing the separation of electron-hole pairs in TiO_2 and decreasing the recombination rate; (2) shifting light absorption from the UV region into the visible light region by doping/coupling non-metallic/metallic species; (3) improving the quantum yield by designing novel architectures. In this chapter, several successful attempts and recent progress will be reviewed.

2.1 Modification of pristine TiO_2

For pristine TiO_2, many factors affect its photocatalytic performance, such as crystalline phase, surface area, and density of surface hydroxyl groups, among which the crystalline phase plays the most important role in photocatalytic reaction (Ding et al., 2000). TiO_2 exists naturally in four polymorphs: anatase (tetragonal, space group I41/amd), rutile (tetragonal, space group P42/mnm), brookite (orthorhombic, space group Pbca), and TiO_2(B) (monoclinic, space group C2/m). Each phase possesses different properties and applications. It is well documented that the anatase polymorph has the higher photoactivity compared to rutile polymorph (Hoffmann et al., 1995). Rutile is thermodynamically stable than the other three polymorphs under ambient conditions. But when particle diameters are below ca. 14nm, anatase is more

stable than rutile (Zhang and Banfield, 2000). Brookite has been reported to be a high-pressure TiO_2 phase and can be synthesized from aqueous or organic media via hydrothermal preparation (Nagase et al., 1999). Compared with anatase and rutile, the photocatalytic study of brookite is quite limited, partly because that its synthesis route is rather difficult. The frameworks of anatase, rutile and brookite were shown in Figure 2.1. TiO_2(B), a metastable monoclinic modification of TiO_2, was firstly discovered in nature in 1991 (Banfield et al., 1991). Recent studies have proved that brookite itself exhibits photocatalytic activity (Iskandar et al, 2007) while TiO_2(B) can contribute to the photocatalytic applications when it is involved in the binary mixture of TiO_2 polymorphs (Yang et al., 2009).

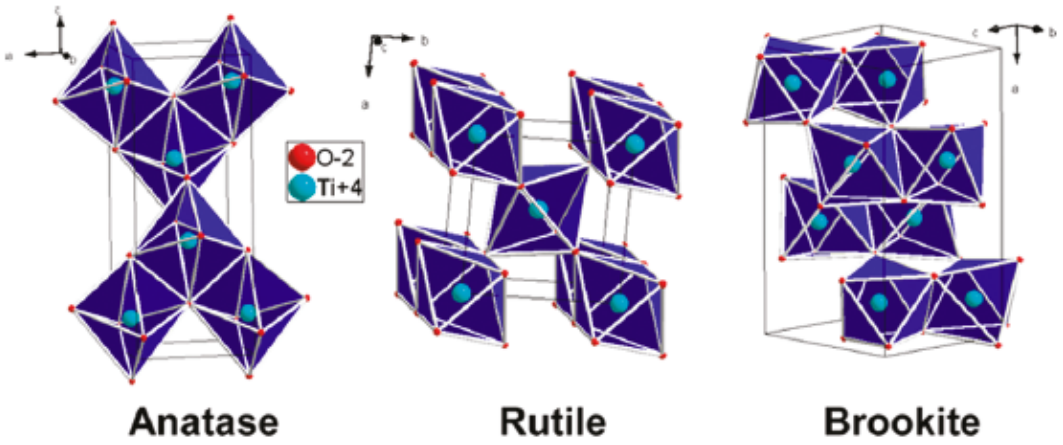

Figure 2.1 Representations of the TiO_2 anatase, rutile, and brookite forms (Dambournet et al., 2010).

2.1.1 Phase junction effect of bi-crystalline TiO_2

It is widely accepted that pure anatase polymorphs shows better photocatalytic performance than pure rutile due to its higher organic infinity (Hoffmann et al., 1995). However, some researchers showed that rutile was more suitable than anatase as photocatalysts (Mills et al., 2003). A very interesting phenomenon is that Degussa

P25, a commercial product with anatase and rutile polymorphs (80/20, w/w), showed higher photocatalytic activity than pure anatase or pure rutile in several cases (Ding et al., 2000).

As to the mechanism of bicrystalline TiO_2 photocatalysts, Bacsa and Kiwi (1998) indicated that the mesoporosity and wide pore size distribution induced by rutile phase were responsible for the higher photocatalytic activity of anatase-rutile mixture. However, it does not have universal significance. Soon afterwards, Kawahara et al. (2002) synthesized patterned anatase-rutile bi-crystalline thin film on quartz substrate by a combination method of sputter deposition and subsequent sol-gel processing. This film showed better photoactivity for decomposition of CH_3CHO than pure anatase and pure rutile under UV light irradiation. By subsequent investigation of photodeposition of Ag on such patterned bi-crystalline thin film, they proposed that: (1) photoinduced electrons can transfer to conduction band (CB) of rutile at phase junction due to the CB of rutile is less than that of anatase; (2) such energy barrier can also contribute to the suppression of back electrons transfer. Thus, “phase junction effect” is responsible for the better photocatalytic performance of bi-crystalline TiO_2 photocatalysts. This study offered a good explanation and has been accepted by most of the researchers.

2.1.2 Synthesis of traditional bi-crystalline TiO_2 photocatalyst

Due to phase junction effect just mentioned, synthesizing highly efficient bi-crystalline TiO_2 photocatalysts has attracted increasing attention during the past decade. Traditional bi-crystalline TiO_2 consists of anatase-rutile mixture, anatase-brookite mixture and rutile-brookite mixture.

Generally, the synthesis routes of anatase-rutile mixture can be roughly classified into three ways: (1) sol-gel method; (2) hydrothermal/solvothermal method; (3) calcination of Ti precursors at high temperatures. Luo et al. (2003) successfully synthesized mesoporous bicrystalline anatase-rutile mixture with fine control the phase content and tri-crystalline framework by a facile sol-gel method. They found that the framework can be easily tuned by varying the solvents. Interestingly, it is the first time that mesoporous tri-crystalline framework has been successfully fabricated. Chen et al. (2007) prepared a series of mesoporous anatase-rutile mixtures with different phase composition by tuning the molar ratio of Ti precursors ($TiCl_4$/$Ti(OBu)_4$). The sample with anatase/rutile (82:18, w/w), which is very similar to phase content of Degussa P25 (80/20, w/w), exhibited the highest activity for phenol photodegradation. Scotti et al. (2008) also successfully achieved fine control of bi-crystalline framework by tuning PH value through adding water or HCl. However, one of the major problems with the above works is the high temperature employed in order to obtain good crystalline TiO_2, leading to low specific surface area. Yan et al. (2005) tuned the phase content of anatase-rutile mixture by varying the proportion of anion in the aqueous phase of microemulsion. The specific surface area of titania was found to be 113-169 m^2/g and the sample with 74.2% anatase showed the best photocatalytic activity. Tian et al. (2008) synthesized anatase-rutile mixture photocatalysts with a specific surface area as high as 276 m^2/g through hydrothermal treatment and subsequent treatment with ethylenediamine. The phase composition was controlled by calcination temperature. Besides, Zhang et al. (2008a) suggested that the surface phases have a direct effect on the photocatalytic activity of TiO_2 and they synthesized anatase-rutile mixture with different surface phase composition by direct calcination of Ti precursor at different temperatures (Figure 2.2). It is of high

significance that their work provided direct evidence to support the phase junction effect of bi-crystalline TiO_2 photocatalysts.

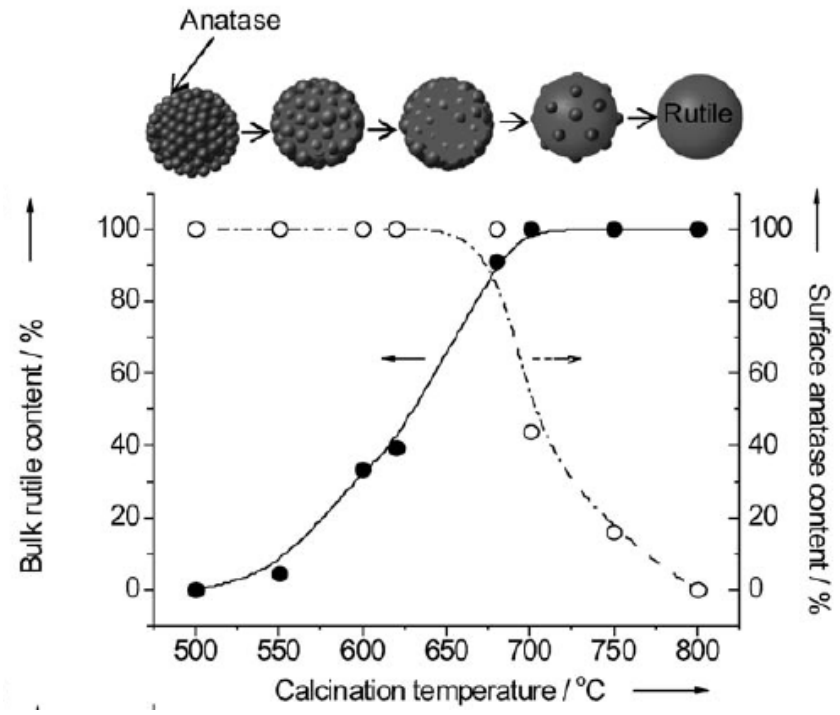

Figure 2.2 Dependence of the bulk rutile content and surface anatase content on the calcination temperature (Zhang et al., 2008a).

Bi-crystalline anatase-brookite framework was firstly synthesized by employing sonochemical sol-gel method and was found to exhibit higher photocatalytic activity than pure anatase TiO_2 and Degussa P25 (Yu et al., 2001; Yu et al., 2002b). Afterwards, Ozawa et al. (2005) reported the low-temperature preparation route of bi-crystalline anatase-brookite mixture. The photocatalytic activity of anatase-brookite mixture with its optimal phase content (65/35, w/w) for the gas-phase oxidation of CH_3CHO was 5.4 times greater than that of pure anatase. Besides, it is reported that anatase-brookite mixture (70/30, w/w), fabricated by hydrothermal method, showed excellent activity in photo-degradation of NO_x, photo-oxidation of 2-chlorophenol (Ardizzone et al., 2007). As to bi-crystalline rutile-brookite frameworks, they were synthesized via thermolysis of $TiCl_4$ in diluted HCl solutions (Di Paola et al., 2008) or

via hydrothermal method by employing $TiCl_3$, NaCl and methylcellulose (Wei et al., 2007).

2.1.3 Novel bi-crystalline anatase-TiO_2(B) photocatalysts

In recent years, the photocatalytic activity of pure-phase TiO_2(B) attracts great attention due to its unique crystallographic structure (Li et al., 2008c; Zhang et al., 2008b; Chakraborty et al., 2009). The photocatalytic activity of pure-phase TiO_2(B) in decomposing organic compound was not as high as the anatase in general (Zhang et al., 2008b). However, owing to the phase junction effect, the bi-crystalline anatase-TiO_2(B) revealed higher photocatalytic efficiency (Li et al., 2008c; Bai et al., 2009; Yang et al., 2009). Generally, the synthesis routes of bi-crystalline anatase-TiO_2(B) are classified into two categories and thus resulted in two interesting opposite core-shell structures, anatase/TiO_2(B) core-shell nanofibers and TiO_2(B)/anatase core-shell nanofibers.

Anatase/TiO_2(B) core-shell nanofibers has been prepared by three consecutive processes, including preparation of alkali metal titanates, $A_2Ti_nO_{2n+1}$ (A = Na, K, Cs; $3 \leq n \leq 6$), by solid state reaction between TiO_2 and alkali metal carbonates at high temperature above 800^oC, subsequent proton exchange between alkali metal titanates and dilute HCl acid, and the last calcination at proper temperatures, which significantly affects the phase content (Li et al., 2008c; Bai et al., 2009). It is reported that Pt-loaded anatase/TiO_2(B) core-shell nanofibers showed better photoactivity than Pt-loaded P25 in decomposition of organic wastes (Bai et al., 2009).

TiO_2(B)/anatase core-shell nanofibers has been fabricated via two consecutive partial phase transition processes, hydrothermal reaction and heating treatment (Yang et al., 2009). In this work, $H_2Ti_3O_7$ nanofibers were first produced via hydrothermal

reaction between anatase and concentrated NaOH solution, and subsequent ion exchange. In the first partial phase transition, $H_2Ti_3O_7$ nanofibers partially reacted with dilute HNO_3, generating a thin anatase shell. The following heating treatment converted the $H_2Ti_3O_7$ core into TiO_2(B) core at 450°C. The phase content can be tuned by control the reaction time of $H_2Ti_3O_7$ nanofibers and dilute HNO_3. This novel bicrystalline structure with the optimal composition (Anatase:TiO_2(B)=74:26), which is similar to the phase content of Degussa P25, showed highest photocatalytic activity, even better than P25 (Figure 2.3a). As graphically illustrated by the authors, phase junction effect, and the resulting unidirectional electron transfer and low electron-hole recombination rate were responsible for this enhanced photoactivity of bi-crystalline TiO_2 frameworks (Figure 2.3b).

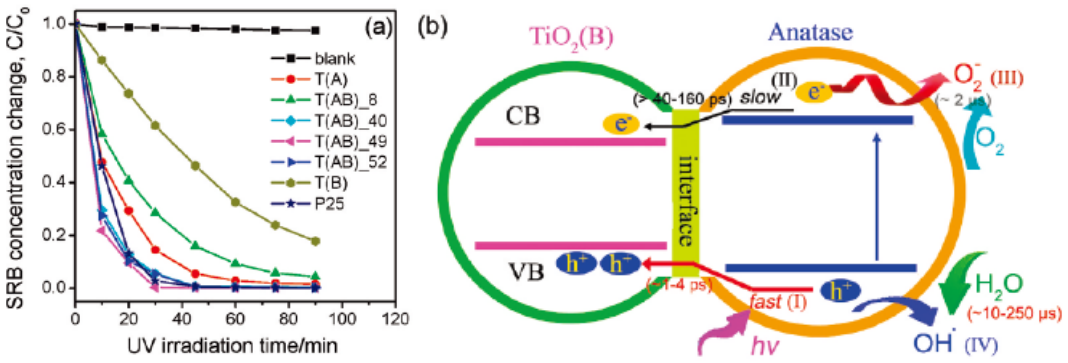

Figure 2.3 (a) Photocatalytic decomposition of the organic dye sulforhodamine B (SRB) with different fibril Anatase/TiO_2(B) photocatalysts under UV irradiation; (b) possible electron-hole separation mechanism of mixed-phase nanofibers during photocatalysis driven by UV light illumination (Yang et al., 2009).

2.2 Modifying TiO_2 photocatalysts by doping strategies or depositing noble metal nanoparticles

One of the challenges about pristine TiO_2 photocatalysts is that they can only absorb UV light, a small portion of solar light (5%), due to its wide band gap (3.2eV).

In order to exploit the more abundant energy source of solar light, especially the visible light (46%), doping TiO_2 by metal or non-metallic species ionic species is an efficient and promising method to obtain visible light activity by changing the electronic structures. Besides, depositing TiO_2 with noble metal or metal oxide nanoparticles or synthesizing noble metal-TiO_2 composites also achieve great success to absorb visible light as well as to enhance the photocatalytic activity.

2.2.1 Doped TiO_2 photocatalysts

2.2.1.1 Transition-metal-ion doped TiO_2 photocatalysts. To lower the band-gap energy of TiO_2, transition-metals, including Fe, Cr, V, Ni, Mn, Co, Cu, Cd, Ag, Zn, Zr, Nb, Ru and Ta, were doped into TiO_2 photocatalysts, occupying the substitutional or interstitial cites in the TiO_2 lattice, by employing ion implantation, sol-gel method or heat treatment process (Choi et al., 1994a; Choi et al., 1994b; Chatterjee and Dasgupta, 2005; Zhou et al., 2006b). Upon transition-metal-ion doping, new energy levels of guest metal ions can be formed around the valence band (VB) or conduction band (CB) of TiO_2. Besides, the oxygen vacancy and/or oxygen atom can also be generated due to the differences of the valence states between Ti^{4+} and guest metal ions (Zhang et al., 2009b). The energy level of oxygen vacancy is slightly lower than the CB of TiO_2, contributing to the band-gap narrowing. Thus transition-metal-ion doping can shift the adsorption band of TiO_2 photocatalysts from UV region to visible light region (Anpo and Takeuchi, 2003; Zhang et al., 2009b). Anpo and Takeuchi (2003) also indicated that the order of the effectiveness in the red shift was found to be V>Cr >Mn>Fe>Ni. Furthermore, the doped guest metal ions with an optimized concentration can greatly increase the lifetime of charge carriers by trapping photo-induced electrons (Choi et al., 1994a; Choi et al., 1994b), thus a enhanced

photocatalytic activity. For example, Zhou et al. (2006a; 2007) found that both V-ion-doped TiO_2 thin film and V-ion-doped P25 pallets exhibited excellent photocatalytic performance towards oxidation of formic acid under visible light irradiation mainly due to the increase of lifetime of charge carriers.

2.2.1.2 Non-metallic species doped TiO_2. It is the work published on Science by Asahi et al. (2001) that stirred researchers to improve and investigate non-metallic species doped TiO_2 photocatalysts. They initially set three requirements to achieve visible-light-active TiO_2 photocatalysts: (1) doping should produce states in the band gap of TiO_2 that absorb visible light; (2) the conduction band minimum, including subsequent impurity states, should be as high as that of TiO_2 or higher than the H_2/H_2O level to ensure its photoreduction activity; and (3) the states in the gap should overlap sufficiently with the band states of TiO_2 to transfer photoexcited carriers to reactive sites at the catalyst surface within their lifetime (Asahi et al., 2001). Based on the theoretical results of substitutional doping with a series of non-metallic species elements (C, N, F, P, or S) into O sites in anatase TiO_2, they finally chose N since its p states can contribute to the band-gap narrowing by mixing with O 2p states. Their sample, $TiO_{2-x}N_x$, revealed better optical properties (Figure 2.4A) and photocatalytic activities under visible light illumination (Figure 2.4B).

From then on, various non-metallic species elements, such as B (Chen et al., 2006), C (Sakthivel and Kisch, 2003), F (Yu et al., 2002a; Pan et al., 2008), P (Körösi et al., 2007), S (Umebayashi et al., 2002), and halogens (Usseglio et al, 2007; Yang et al., 2008) have been successfully doped into TiO_2 photocatalysts. Due to its significant contribution to electronic structures and the similar size with O, nitrogen has become the most effective and promising dopant in TiO_2 among all the non-metallic species dopants, and attracted the most extensive research in the world.

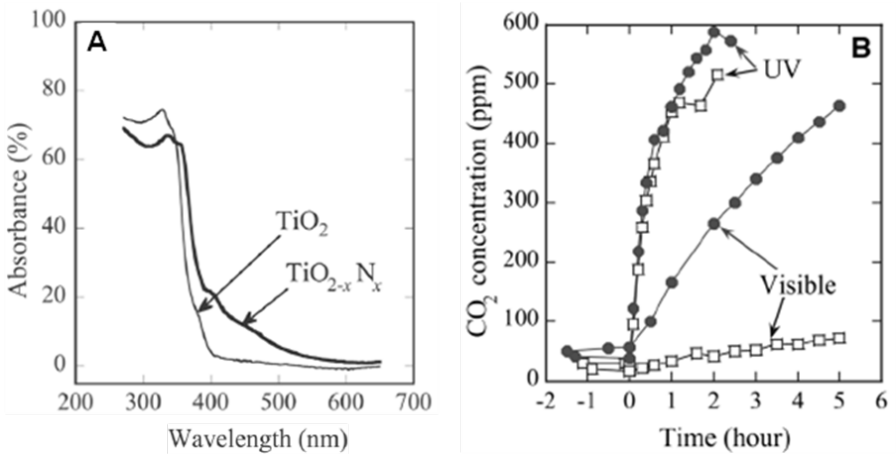

Figure 2.4 (A) Optical absorption spectra of $TiO_{2-x}N_x$ and TiO_2; (B) CO_2 evolution as a function of irradiation time (light on at zero) during the photodegradation of acetaldehyde gas under UV light and visible light over $TiO_{2-x}N_x$ (solid circles) and pristine TiO_2 (open squares), respectively (Asahi et al., 2001).

The most disputed topic on the N-doped TiO_2 photocatalysts is the origin of visible-light response and enhancement of photocatalytic activity. Some typical mechanisms in the literature were summarized by Serpone (2006) (see Figure 2.5). Aashi et al. (2001) proposed that the band gap narrowing by mixing N 2p and O 2p states was the nature of N-doped TiO_2 (Figure 2.5c). While some other researchers suggested that the discrete localized states above the valence band (Chen and Burda, 2008) or below the conduction band (Torres et al., 2004) held responsibility for visible-light-active photocatalytic performance (Figure 2.5b).

Serpone's group (2006; 2007) investigated the difference diffuse reflectance spectra of a series of TiO_2-based photocatalysts. In their works, all the difference diffuse reflectance spectra showed very similar feature regardless of N precursors and synthesis route. More interestingly, these spectra can be deconvoluted into three Gaussian bands centered around: 1) 1.7-2.1eV (729-590nm); 2) 2.4-2.6eV (517-477nm); 3) 2.9-3.0eV (428-413nm). Thus they proposed that color centers were the nature of doped TiO_2 and the three bands were caused by the transitions of color centers (see Figure 2.5d and e). Serpone's works offered a new method to investigate

the mechanism of visible-light-active N-TiO_2 photocatalysts, accepted by other researchers (Qiu et al., 2007). However, Mitoraj and Kisch (2008) stated that the origin of N-doped TiO_2, with urea as its N precursors, was melem and melon acting as visible-light sensitizers rather than nitrogen species or oxygen vacancies and colour centers.

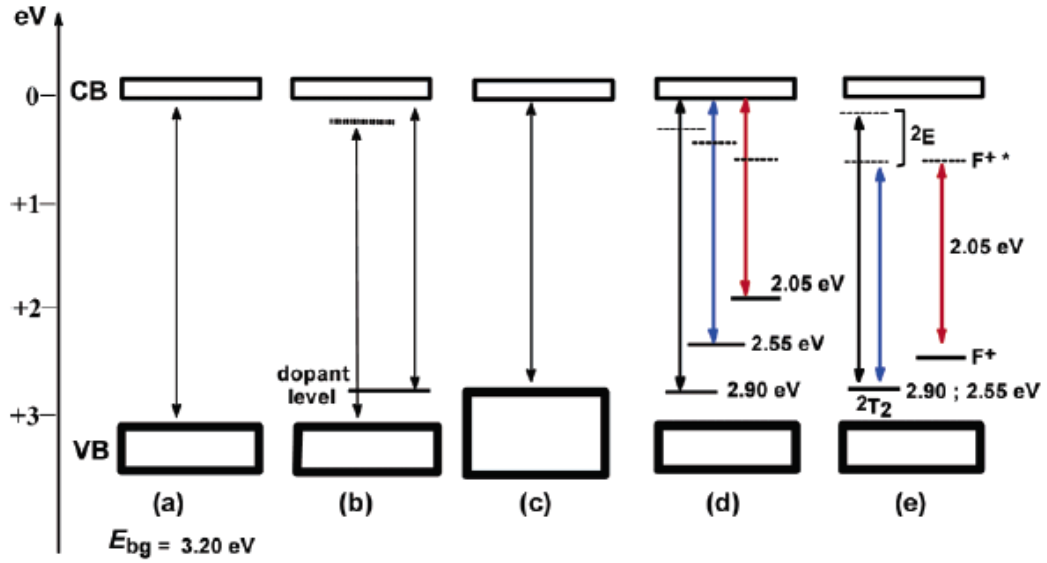

Figure 2.5 Various schemes illustrating the possible changes that might occur to the band gap electronic structure of anatase TiO_2 on doping with various non-metallic elements (Serpone, 2006).

In recent years, non-metallic species codoped TiO_2 photocatalysts, e.g. N, B-codoped TiO_2 (In et al., 2007; Gopal et al., 2008; Liu et al., 2008a), N, F-codoped TiO_2 (Li et al., 2005a; Li et al., 2005b), *etc*., have been synthesized to improve the photocatalytic activity. It is reported that N, B-codoped TiO_2 photocatalysts, prepared by a two-step hydrothermal method, showed enhancing the photocatalytic activity compared with N-doped TiO_2 and B-doped TiO_2, mainly due to the formation of the new O-Ti-B-N surface structure, which facilities surface separation and transfer of charge carriers (Liu et al., 2008a). This work was of high significance for addressing the synergistic effects of B/N codoping via both theoretical and experimental studies.

2.2.2 Noble metal-TiO_2 composite photocatalysts

Considerable efforts have been devoted to modify TiO_2 photocatalysts by introducing noble metal nanoparticles (NPs), such as Ag (Anderson et al., 2005; Awazu et al., 2008), Au (Li et al., 2007b; Li et al., 2008a; Bannat et al., 2009), Pt (Wang et al., 2005c; Li et al., 2009; Xie et al., 2009), Pd (Ismail et al., 2010) *etc.*, as well as noble metal oxide and metal halogen NPs (Li et al., 2008b). Most of the synthesized noble metal-TiO_2 composites showed enhanced photocatalytic performance due to the Schottky barrier, forming between the metal NPs and the support TiO_2. The so-called Schottky barrier, similar with energy barrier or the phase junction effect existing in Degussa P25 (Kawahara et al., 2002), results in trapping the photo-induced electrons in noble metal NPs, which significantly increases the lifetime of charge carriers (Linsebigler et al., 1995).

2.2.2.1 Ag-TiO_2 composite photocatalysts. Ag-TiO_2 photocatalysts have been attracted much attention in the past decades, mainly due to some unique advantages of Ag species: 1) metallic silver and silver ions have been known to show excellent broad-spectrum antibacterial properties for years (Li et al., 1998; Kumar et al., 2008); 2) Ag has no detrimental effects on mammalian cells at low amount and it has been employed to produce environmentally friendly paint (Kumar et al., 2008); 3) Ag is cheaper than other noble metals. Stimulated by these advantages, significant efforts have been made to design Ag-TiO_2 composite photocatalysts. Silver NPs can be deposited onto the surface of TiO_2 particles (Zhang et al., 2007; Thiel et al., 2007), nanotubes (Toledo-Antonio et al., 2009), nanofibers (Jin et al., 2007), nanorods (Cozzoli et al., 2004), TiO_2 thin films (Page et al., 2007), etc or deposited into the pores of porous TiO_2 photocatalysts (Wang et al., 2005a; Anderson et al., 2005; Liu et al., 2008b) through photo-assisted reduction (Cozzoli et al., 2004; Zhang et al., 2007;

Jin et al., 2007), chemical reduction (Zhang et al., 2007), and ion-exchange or impregnation following with annealing reduction (Toledo-Antonio et al., 2009; Anderson et al., 2005).

Besides, an interesting Ag-TiO_2 core-shell structure has been proposed and fabricated (Hirakawa and Kamat, 2004; Hirakawa and Kamat, 2005; Sakai et al., 2006). In the works of Hirakawa and Kamat (2004; 2005), Ag ions was firstly reduced and formed an Ag core and then Ti precursor was hydrolyzed to form a TiO_2 shell around the Ag nanoparticles. They found that charge separation occurred in the TiO_2 shell and photo-induced electrons can be stored in the Ag core upon UV light irradiation as illustrated in Figure 2.6, evidenced from the surface plasmon band of silver shift from 460nm to 420nm (Hirakawa and Kamat, 2004). The charge equilibrium plays an important role in the photocatalytic reaction.

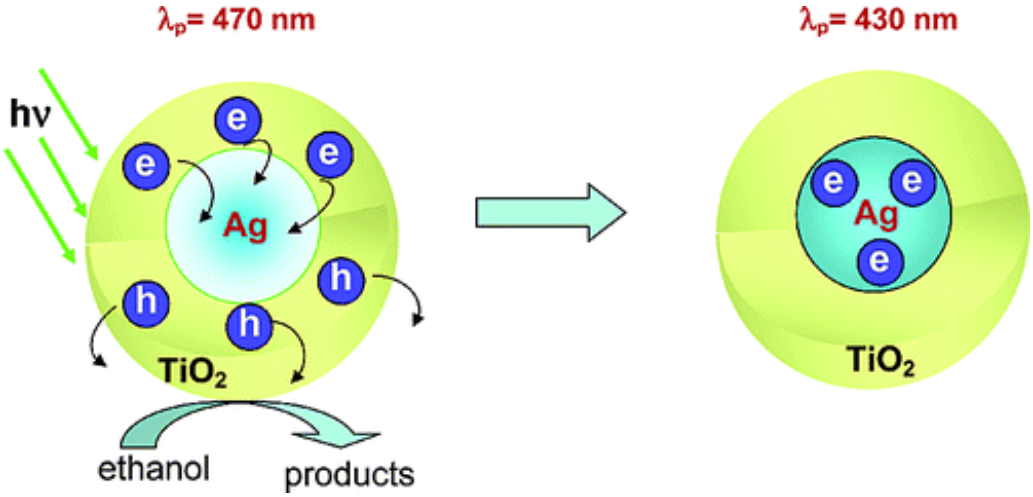

Figure 2.6 Photoinduced charge separation and storage in Ag/TiO_2 core-shell structure (Hirakawa and Kamat, 2004).

Recently, Awazu et al. (2008) proposed a novel concept of photocatalysts, named "Plasmonic Photocatalysts", by utilizing the surface plasmon resonance property of Ag NPs. In their work, TiO_2 thin film was deposited onto Ag-SiO_2 composite film with a core-shell structure and the prepared material exhibited better photocatalytic

performance than TiO_2 thin films deposited on pristine SiO_2 substrate. They indicated that the use of SiO_2 shell was mainly due to: 1) protecting Ag nanoparticles from oxidation; 2) shifting the surface plasmon band to UV region (380nm) from visible region (Awazu et al., 2008). Kubacka et al. (2009) introduced such plasmonic photocatalysts (Ag/TiO_2) into the ethylene-vinyl alcohol polymeric matrix, forming inorganic-organic composite photocatalyst. Due to the plasmon effect, the presence of minute amounts of Ag NPs greatly promoted the antibacterial properties to Gram-negative, Gram-positive bacteria/cocci, and yeasts. Furthermore, this material exhibited outstanding resistance to biofilm formation.

Moreover, visible-light active photocatalysts $Ag/AgCl/TiO_2$ (Anderson et al., 2005), $Ag/AgBr/TiO_2$ (Hu et al., 2006) and AgI/TiO_2 (Hu et al., 2006; Li et al., 2008d) composite photocatalysts were synthesized and found to show enhanced photocatalytic activity for destructing bacteria and degrading azo dyes. $Ag/AgBr/TiO_2$ composite photocatalyst covered by apatite was prepared and found to show enhanced photocatalytic antibacterial properties by Elahifard et al. (2007). They demonstrated that the photocatalysts adhere to the outer membrane of the cell due to hydrogen bonding between phosphate groups of apatite and polysaccharide strings of membrane, offering more chances for the reactive species to destruct the cell.

2.2.2.2 Au-TiO_2 composite photocatalysts. Despite its bulk inertness, Au NPs with small size can also be loaded/deposited to TiO_2 (Subramanian et al., 2003; Li et al., 2007b; Bannat et al., 2009; Bian et al., 2009; Zhao et al., 2009; Liu et al., 2010) or anionic modified TiO_2 (Wu et al., 2009) to enhance the absorption of visible light as well as photocatalytic activity due to the plasmons resonance effect of gold NPs and high Schottky barrier existing between host TiO_2 and guest Au NPs.

Li et al. (2007b) fabricated Au NPs-loaded mesoporous TiO_2 photocatalyst by using evaporation-induced self-assembly (EISA) method. The gold precursor was directly added into the mother sol containing Ti precursors and triblock copolymer. The resulted 0.5% Au-TiO_2 composite was demonstrated 3 times higher photocatalytic activity than pure mesoporous TiO_2. Bian et al. (2009) homogeneously encapsulated Au NPs (~5nm) in mesoporous core-shell TiO_2 microspheres by using a consecutive solvothermal and hydrothermal treatments (Figure 2.7).The preparation of this novel structure could be interpreted in terms of alcoholysis-induced self-organization of the zero-dimensional (0D) TiO_2 building clusters into 3D mesoporous microspheres under solvothermal condition together with their dissolution, re-deposition and Au^{3+} ions in-situ reduction by hydrothermal treatment. The formed Au-TiO_2 composite photocatalyst was found to exhibit enhanced photocatalytic activity and excellent of durability owing to the difficulty of leaking of Au NPs encapsulated in the chamber of TiO_2 microspheres.

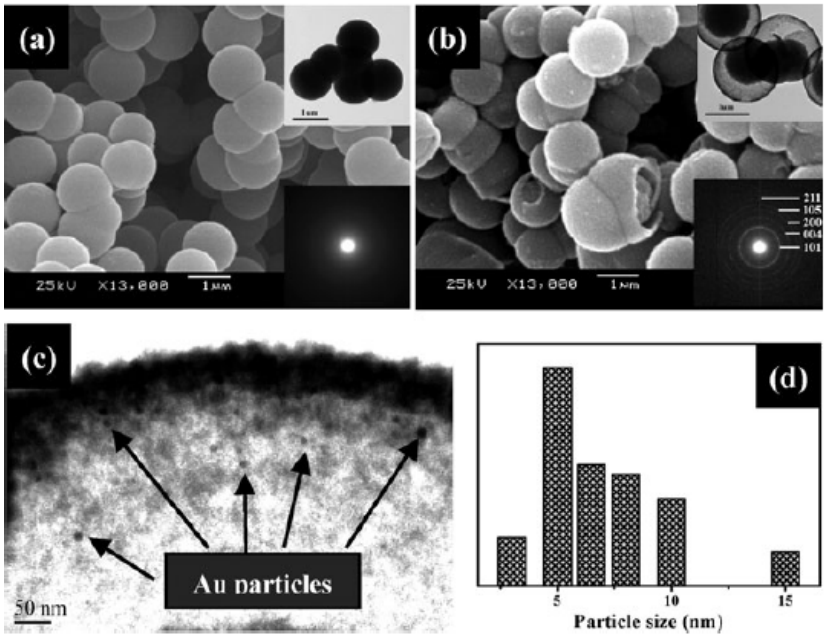

Figure 2.7 (a) SEM image of the Au/TiO_2 precursor before hydrothermal treatment. (b-d) SEM, TEM and Au size distribution pattern of the Au/TiO_2. The insets are the TEM and SAED images (Bian et al., 2009).

Furthermore, Au-loaded TiO_2 composites are excellent starting materials for preparation of all-solid-state Z-scheme CdS-Au-TiO_2 three-component (3C) nanojunction system (Tada et al., 2006; Zhu et al., 2009) due to the effective capability of photoreduction of S_8 to S^{2-} (Kiyonaga et al., 2006) by Au-TiO_2 in aqueous environment. Such Z-scheme 3C nanojunction photocatalysts were demonstrated much better photocatalytic performance than 1C and 2C system towards destroying azo dyes (Tada et al., 2006; Zhu et al., 2009), which was ascribed to the vectorial electron transfer of TiO→Au→CdS in such 3C system (Tada et al., 2006).

2.2.2.3 Pt-TiO_2 composite photocatalysts. Platinum NPs have been introduced into the TiO_2-based photocatalysts, forming Pt-TiO_2 composites, mainly due to two reasons, *i.e.* its fast photo-induced electrons trapping and selective adsorption of organic reactants on its surface (Zhang et al., 2009b). Li et al. (2009) deposited monodisperse Pt NPs onto the SiO_2/TiO_2 photocatalysts with a core-shell structure by a self-assembly method and the resulted sample was easier to be separated from reaction medium after photocatalysis in comparison with Degussa P25 and showed an unexpected enhanced photocatalytic performance during the recycle use due to the Pt oxidation state changing within photoreaction. Xie et al. (2009) developed a simple and green in-situ method to deposit noble metal NPs, such as Pt, Ru and so on, onto the surface of TiO_2 with uniform dispersion and very tiny size of metal NPs (~0.5-2.5nm) by employing titanium (III) oxide as the Ti precursor as well as the reductant as illustrated in Figure 2.8. The finally prepared Pt-TiO_2, Ru-TiO_2 and Pt,Ru-TiO_2 samples exhibited significantly enhanced photocatalytic activity than neat TiO_2 under UV irradiation.

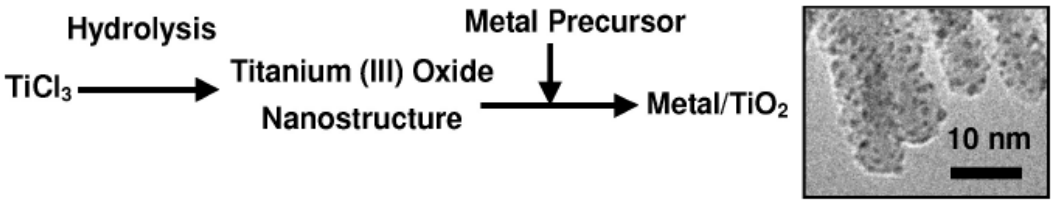

Figure 2.8 Schematic illustration of in-situ route to deposit noble metal nanoparticles onto TiO_2 and the TEM image of Pt-TiO_2 (Xie et al., 2009).

2.2.2.4 Pd- or PdO-TiO_2 composite photocatalysts. Recently, mesoporous Pd-TiO_2 photocatalyst was prepared by EISA method and the subsequent heat treatment converted Pd^{2+} to Pd NPs (Ismail et al., 2010). The synthesized Pd-TiO_2 calcined at 450^{o}C possessed large surface area and effective photocatalytic activity towards oxidation of methanol. Besides, palladium oxide NPs deposited on N-doped TiO_2 nanofibers (PdO/TiON) was found to show an interesting "memory" effect, *i.e.* it can kill 90% *E. coli* cells in dark environment after a pre-treatment of 10h exposure to simulate visible light irradiation (Li et al., 2008b). By employing conductive AFM and in-situ XPS techniques, they found that photo-induced electrons transferred from n-type semiconductor TiON to the PdO NPs under visible light irradiation, leading to the reduction of Pd^{3+} to Pd^{2+}. The leaving holes can transfer to the surface and benefit the photo-killing bacteria under visible light irradiation. After the light shut-off, the trapped electrons was released from PdO NPs and may transfer back to TiON, producing hydroxyl radicals and thus triggering the "memory" antibacterial effect (Li et al., 2010b).

2.3 Porous TiO_2-based photocatalysts

In the past two decades, porous TiO_2-based photocatalysts has attracted increasingly attention due to its many advantages, such as (1) a high density of active centres owing to their large surface area, (2) an enhanced light harvesting because of light reflection and scattering by the pores, and (3) possible recovery and reuse after each cycle of photocatalytic process.

2.3.1 Template methods

2.3.1.1 The hard template approach. In such confined-space assembly, Ti precursors are firstly introduced into the pores of the hard templates by means of wetting, sorption, deposition, complexation, grafting, ion exchange, *etc.* After materials processing and subsequent selective removal of the hard templates, porous TiO_2 photocatalysts can be obtained due to the "molding" effect of the hard templates. Apparently, the textural properties of the porous TiO_2, being a negative replica, are determined by the hard templates.

Meso/macroporous TiO_2 photocatalysts could be fabricated by employing porous silicas (Kim et al., 2008; Yue et al., 2009), alumina (Chae et al., 2005) and resins (Wang et al., 2007a) as hard templates. The challenge about preparation of mesoporous TiO_2 lies in the fast hydrolyze and polycondense rate of titanium alkoxides, leading to the formation of bulky precipitates, which makes them hard to be impregnated into the pore channel of hard templates. Recently, Kim et al. (2008) prehydrolyzed a titanium alkoxide and redissolved the obtained precipitate using a concentrated HCl solution. The aqueous solution of titanium oxychloride complex was found to be easily infiltrated into the mesopores of SBA-15, MSU-H and KIT-16 templates. After removal of the silicas, mesoporous TiO_2 with well-defined regular

mesopores and crystalline frameworks of mainly anatase phase were obtained. By applying the similar strategy with HNO_3 instead of HCl acid, Yue et al. (2009) successfully fabricated mesoporous bicrystalline TiO_2 (anatase and rutile).

Besides, by using self-assembled colloidal crystals as hard templates (Srinivasan and White, 2007; Galusha et al., 2008), 3D highly ordered macroporous TiO_2 photocatalysts (inverse TiO_2 opals) were obtained. Inorganic precursors were introduced into the interstices of the colloidal crystal by vacuum infiltration. Upon solidification and template removal, inverse TiO_2 opals were obtained. Srinivasan and White (2007) demonstrated that macroporous TiO_2 opals with pore diameter 0.5 μm showed an enhanced photocatalytic activity than P25 in photo-degradation of methyl blue dye (MB).

2.3.1.2 The soft template approach. Different from the hard template approach, the soft template approach employs soft matters like single organic molecules and supramolecues (e.g., amphiphilic surfactants and biomacromolecules) as templates. The pores can only be generated after the removal of templates from as-synthesized inorganic-organic composites via thermal treatment, extraction, microwave or UV light irradiation (Wan and Zhao, 2007). It is reported that microporous TiO_2 with a wormhole-like pore structure could be synthesized by using an amphiphilic chelating surfactant as soft template (Chandra and Bhaumik, 2008). The surface area of the microporous TiO_2 was extremely large (up to 634 m^2/g). However, the dimensions and accessibility of pores limited the applications of microporous TiO_2 to small molecules (Soler-Illia et al., 2002).

The larger pore size of mesoporous or macroporous TiO_2 materials significantly extends their photocatalytic applications. Many different soft-template strategies have been developed to prepare mesoporous TiO_2 photocatalyst by employing various

types of surfactants, including triblock or diblock polymers (Yang et al, 1998), cationic surfactant cetyltrimethylammonium bromide (CTAB) (Peng et al., 2005), neutral surfactant dodecylamine (Yoshitake et al., 2002), and recent Gemini surfactant (Lyu et al., 2004). More interestingly, fourteen commercial synthetic dyes were proved to be good organic templates for preparation ordered mesoporous TiO_2 photocatalyst (Wang et al., 2009c). Among the various designed approaches and soft templates, it is widely accepted that the evaporation-induced self-assembly (EISA) in junction with block polymers is the most promising route. A typical EISA process for the synthesis of highly ordered mesoporous TiO_2 starts from a homogeneous sol solution of a Ti precursor and a block copolymer dissolved in ethanol/water with an initial concentration of the block copolymer much lower than its critical micelle concentration (CMC). Subsequent deposition of the sol solution on a substrate (commonly a petri dish) induces the evaporation of the solvent and other volatile compounds, increasing the concentrations of both the Ti species and the block copolymer. Once the concentration of the block copolymer reaches its CMC, self-assembly begins, resulting in the cooperative assembly of Ti species and the block copolymer to form a mesostructured hybrid inorganic/organic composite (Yang et al, 1998; Yang et al., 1999). A humid aging step was proposed by Soler-Illia and Sanchez (2000) to improve the stability of hybrid mesostructures. Finally, mesoporous TiO_2 nanocrystalline photocatalysts are obtained after removal of the template by calcination.

For the photocatalytic activity of mesoporous TiO_2, high crystallinity and large surface area are highly attractive. Calcination at higher temperature would inevitably result in the collapses of the mesopores before the pore walls are fully crystallized. To resolve the crystallinity or stability problem, Tian et al. (2003) developed an ‘‘acid-

base pair'' concept for the synthesis of highly ordered and stable mesoporous metal oxides, including TiO_2, and mixed metal oxides, e.g. $Sn_xTi_{1-x}O_2$ and $Ce_xTi_{1-x}O_2$. An alternative approach to overcome the thermal stability problem was proposed by Li et al. (2004) via adding the amorphous P_2O_5 into the TiO_2 frameworks. The "glue" effect of P_2O_5 endowed the ordered mesostructured TiO_2-P_2O_5 composites with thermal stability up to 700^{o}C. Soon after, Dong et al. (2007) synthesized mesoporous TiO_2-SiO_2 composites with variable Ti/Si ratios and highly thermal stability (up to 900^{o}C) through the synchronous assembly of titanate and silicate oligomers in the presence of triblock copolymer P123 (see Figure 2.9). The amorphous silica also behaved like a glue for linking the anatase TiO_2 nanocrystals, thus dramatically improving the mesostructural thermal stability. TiO_2 was fully crystallized to anatase when calcined at 700^{o}C. At this temperature mesoporous TiO_2-SiO_2 composites exhibited the most excellent photocatalytic activities for the photo-degradation of Rhodamine B (RhB).

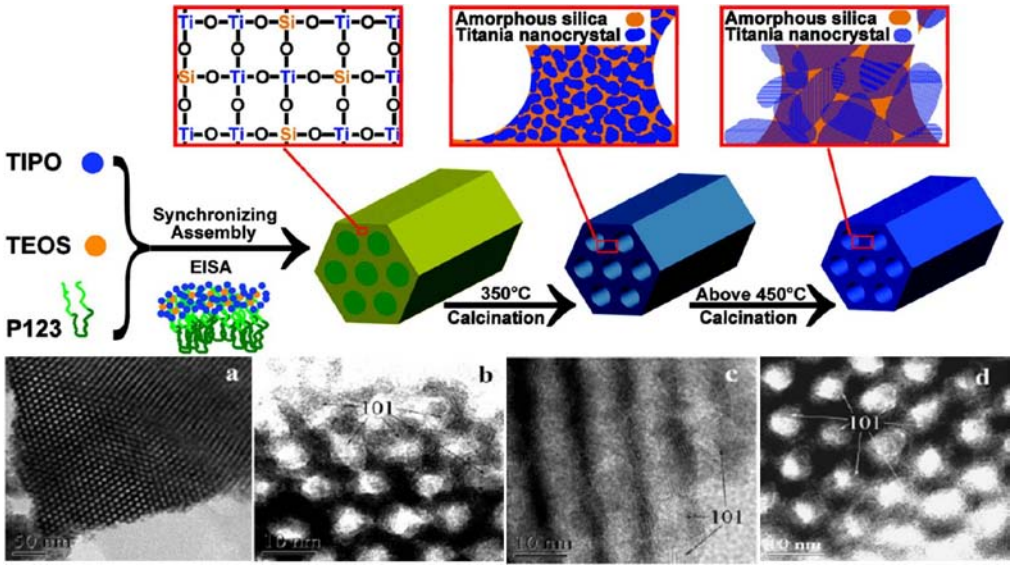

Figure 2.9 Upper: A scheme illustrating the synchronous assembly of titanate oligomers due to the hydrolysis of titanium isopropoxide (TIPO) and silicate species because of the hydrolysis of tetraethyl orthosilicate (TEOS) in the presence of P123 template to form a highly ordered mesoporous TiO_2-SiO_2 composite; TEM (a) and HRTEM (b-d) images of ordered 2D hexagonal mesoporous TiO_2-SiO_2 composite calcined at 700 °C for 4 h (a-c) and at 800 °C for 2 h (d) (Dong et al., 2007).

Very recently, a combined assembly of soft and hard (CASH) method for the preparation of highly crystalline mesoporous TiO_2, with thermal stability up to 1000^oC, was reported by Lee et al. (2008). The template they chose was a diblock copolymer, PI-*b*-PEO, poly(isoprene-*block*-ethylene oxide), which contains a hydrophilic PEO chain and a sp^2-hybridized hydrophobic PI chain. As illustrated in Figure 2.10, upon calcination under an inert environment, the PEO block was fully burnt off, serving as the soft template and generating mesopores. However, the more thermally stable PI blocks were pyrolyzed to rigid amorphous carbon, which mechanically supports the crystallization of the mesoporous frameworks, behaving like a hard template. With a similar strategy, by employing PS spheres as template, 3D macroporous TiO_2 was fabricated by Orilall et al. (2008).

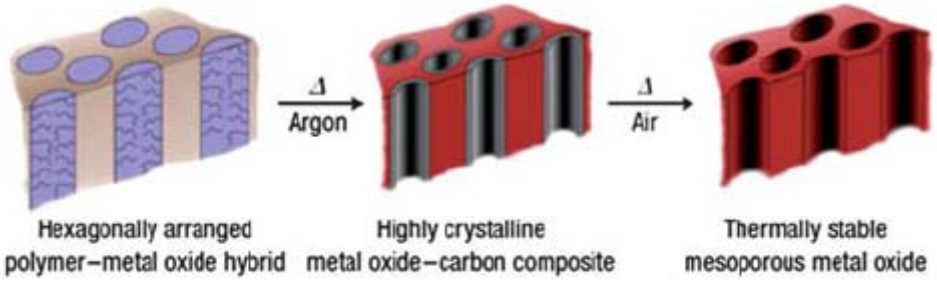

Figure 2.10 Schematic diagram of CASH method (Lee et al., 2008).

Hierarchically macro-mesoporous TiO_2 materials have been successfully fabricated by the self-assembling surfactant template approach in conjunction with larger scale agent, including emulsion droplets (Imhof and Pine, 1997), colloidal spheres (Grosso et al., 2003, Liu et al., 2009), polymer foams (Maekawa et al., 2003) and even recent cells (Sun et al., 2009). For example, Grosso et al. (2003) reported the continuous large-scale fabrication of hierarchically macro-mesoporous TiO_2 with hollow microsphere morphology by combining the spray drying technique, surfactant template approach and latex spheres. In the spray drying process, the feed solution,

containing Ti species and block copolymer F127 together with PS spheres, was dispersed by the atomizer and turned into uniform and size-controllable droplets. Droplets were thus forced to move into the assembly chamber, and dried by a hot carrier gas. EISA was launched based on the thus formed aerosols. During this process, the droplet size would decrease due to the solvent evaporation. However, the shape of the aerosol particles did not change because of the presence of surfactant molecules, which lower the interfacial tension of the droplets (Tsung et al., 2008). Subsequent removal of block copolymer and PS spheres through thermal treatment in the heating chamber could generate macroporous interior with mesoporous shell of nanocrystalline TiO_2. Besides, it is reported that macroporous brookite TiO_2 hollow spheres with enhanced photocatalytic performance could be fabricated by spray drying together with colloidal templating (Iskandar et al., 2007).

An alternative route to obtain hierarchically macro-mesoporous TiO_2 photocatalysts was reported by Yuan et al (2003) as well as Wang et al. (2005b). In their works, one single surfactant, Brij 56, was employing as soft template. The prepared hierarchically macro-mesoporous TiO_2 calcined at 350^oC showed photocatalytic reactivity about 60% higher than that of commercial Degussa P25 (Wang et al., 2005b). Incorporation of macropores in mesoporous frameworks not only ensures the highly efficient inner-pore accessibility, but also enhances the photo-absorption efficiency because macropores can serve as light-transfer pathways, which satisfied a wide variety of practical applications (Wang et al., 2005b).

2.3.2 Self-organization of nanobuilding blocks

Three-dimensional (3D) porous TiO_2 photocatalysts have been constructed by a versatile and facile bottom-up self-organization approach from zero-dimensional (0D),

1D, and 2D nanobuilding blocks. The attachment of the low-dimensional building blocks is generally carried out under hydrothermal conditions.

The TiO_2 microspheres built up by hydrous nanoparticles is an excellent example of self-organization of 0D nanoparticles into 3D microspheres. Size-controllable 3D TiO_2 spheres in the diameter range 0.1-2.0 mm have been synthesized by adjusting the synthetic conditions, especially the concentration of the added agglomeration promoters, such as inorganic salts (Eiden-Assmann et al., 2004), amine (Tanaka et al., 2009), ammonia (Sugimoto and Kojima, 2008) and surfactant (Eiden-Assmann et al., 2004), which are added into the medium in advance to alter the interactions between the primary TiO_2 nanoparticles. However, the surface areas of such microspheres were very low (20-70 m^2/g). To increase the surface area, solvothermal treatment has been developed for effective crystallization of TiO_2 without significant loss in porosity (Chen et al., 2009; Kim et al., 2009). For example, Chen et al. (2009) reported that an additional solvothermal treatment of the as-synthesized TiO_2 spheres in an ammonia-containing ethanol-water mixture before calcination could significantly increase the TiO_2 surface roughness with the formation of elongated TiO_2 nanocrystals, thus increasing the surface area.

1D TiO_2 nanorods have been assembled to 3D porous hollow microspheres with an urchinlike morphology under hydrothermal conditions by using potassium titanium oxalate as the Ti precursor (Li et al., 2006). The synthesized TiO_2 hollow spheres consisting of radically arranged rutile nanorods with their growth direction perpendicular to the spherical shell and possessed a BET surface area of 130 m^2/g. By hydrothermal treatment of $TiCl_4$-ethanol-water system, Wang et al. (2007b) synthesized flowerlike and urchinlike TiO_2 microspheres comprised of rutile nanorods at 50^oC. Soon after, water-chloroform emulsion or water-dichloromethane emulsion

was used to allow confined growth and oriented organization of 1D TiO_2 nanorods as illustrated in Figure 2.11 (Xu et al., 2007; Wang et al., 2009a). The morphology of the rutile nanorods TiO_2 hierarchical superstructures, such as free-standing thick film and microspheres can be perfectly manipulated by controlling the molar ratio of reactants. Thanks to the 3D porous superstructures, all the samples mentioned above exhibited higher photocatalytic activity than Degussa P25.

Recently, it is reported that 2D anatase nanosheets with dominant (001) facets was organized to 3D porous TiO_2 microspheres by a radically orientated assembly under solvothermal conditions (Zheng et al., 2009). These TiO_2 microspheres were found to exhibit excellent photocatalytic activity for the degradation of methyl orange.

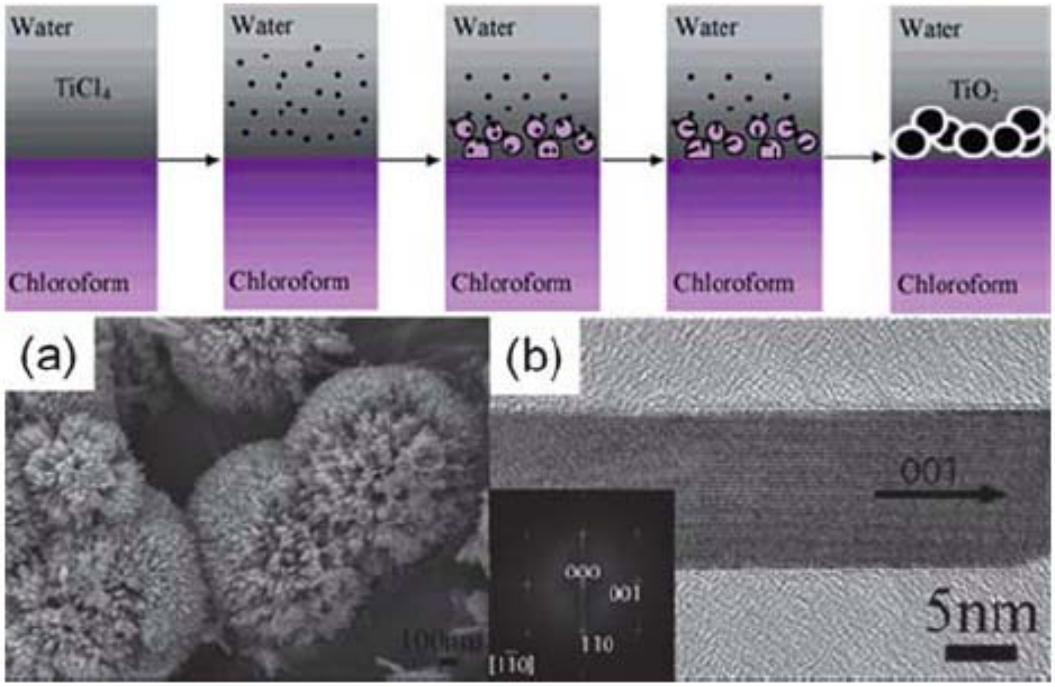

Figure 2.11 Schematic illustration of the formation of hierarchical rutile TiO_2 nanoarchitectures (top); SEM image (a) of TiO_2 microspheres consisting of rutile nanorods synthesized in water-chloroform emulsions; HRTEM image (b) of a single rutile nanorod as well as its 2D Fourier transform pattern (inset) (Xu et al., 2007).

2.3.3 Etching route to hollow structures under hydrothermal conditions

It has been reported that porous anatase TiO_2 hollow microspheres could be fabricated via hydrothermal treatment of a diluted HCl solution containing TiF_4 (Yang and Zeng, 2004a; Yang and Zeng, 2004b) or acidic $Ti(SO_4)_2$ solution in the presence of NH_4F (Liu et al., 2007; Yu et al., 2007). The self-generated HF, which is formed in situ as a hydrolysis product during hydrothermal process, is not only responsible for the formation of hollow structures since it can etch and dissolve the TiO_2 core, but also serves as the source of F-dopant or surface fluorination (Zhou et al., 2008; Pan et al., 2008).

Such F-containing anatase TiO_2 hollow microspheres possesses at least three advantages: (1) a stronger absorption in the UV-visible range than P25 does due to the multiple scattering and reflection of the incident light in the hollow interiors (Pan et al., 2008; Dong et al., 2009); (2) the enhancement of photocatalysis under UV light irradiation or the light respond in the visible light region due to F doping or surface fluorination (Zhou et al., 2008; Pan et al., 2008); (3) the easy recovery and possible reuse properties due to the large size of the hollow microsphere (Liu et al., 2007).

Very recently, Pan et al. (2008) investigated the TiF_4-H_2SO_4 synthesis system under hydrothermal treatment in order to utilizing the inner surface of hollow microsphere for wastewater treatment application. They demonstrated that high acidic concentrations enhanced HF etching and promoted a structural transition from solid to hollow in the spherical interior (Figure 2.12a and b). The prepared F-containing TiO_2 hollow microspheres achieved great success due to the enhanced photocatalytic performance in concurrent photocatalysis and membrane filtration (Figure 2.12c and d).

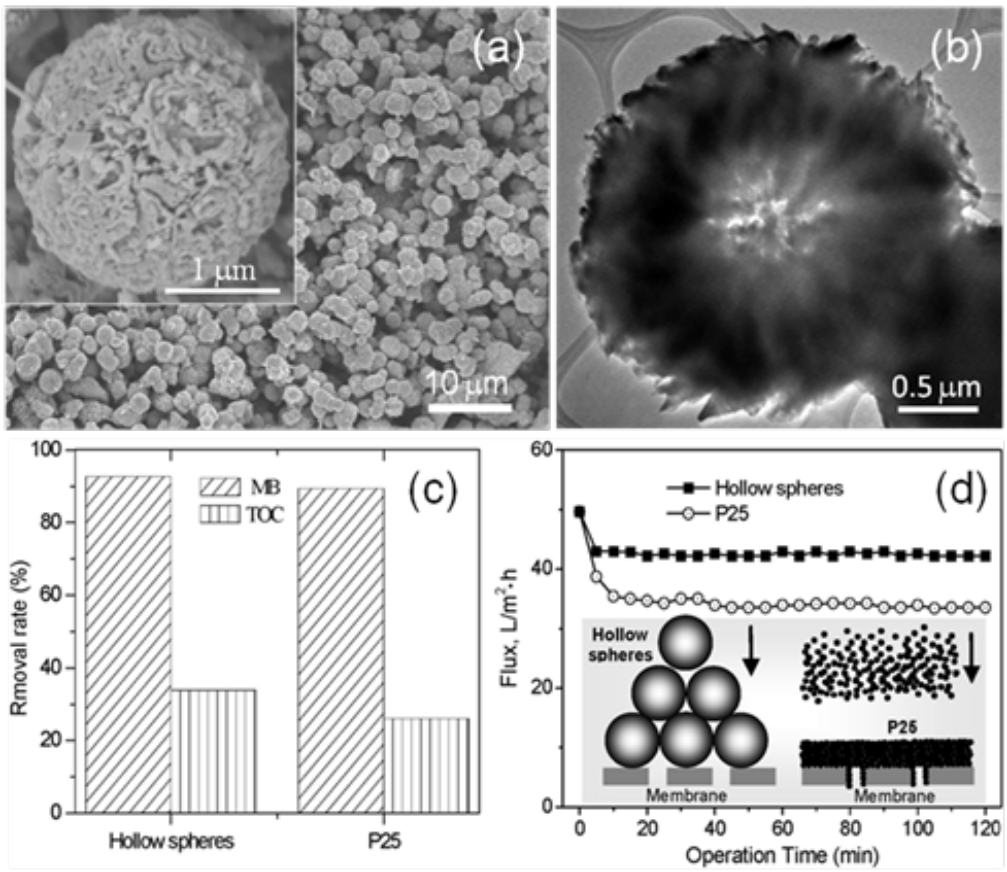

Figure 2.12 SEM (a) and TEM (b) images for hierarchically mesoporous F-TiO_2 hollow microspheres; insert of (a): magnified corresponding to (a); Methyl blue (MB) and TOC removal (c), and membrane flux (d) over mesoporous F-TiO_2 hollow microspheres and P25. Insert of (d): Schematic diagram of membrane fouling caused by photocatalysts (Pan et al., 2008).

2.3.4 Topotactic transition

Porous TiO_2 photocatalysts can also be fabricated through topotactic transition of appropriate solid-state intermediate, which provides crystallographically and chemically matched templates for the resulted porous TiO_2 under restricted conditions (Clarke et al., 1994). 1D porous TiO_2 nanotubes (NTs) synthesized by alkaline hydrothermal method is an excellent example of topotactic transition (Kasuga et al., 1998; Kasuga et al., 1999). Under strong basic environment (e.g., concentrated NaOH or KOH solution) in the hydrothermal synthesis, bulk TiO_2 powders are exfoliated and converted to titanate ($Na_2Ti_3O_7$ or $K_2Ti_3O_7$) nanosheets. Spontaneous curving and

scrolling of the exfoliated nanosheets yield multiwall titanate NTs with both ends opened. The driving force is believed to be the mechanical stress due to the imbalance in the width of layers in the multilayered nanosheets (Bavykin et al., 2004; Riss et al., 2009). Hydrogen titanates ($H_2Ti_3O_7$) NTs can be prepared by topotactic proton exchange in a diluted acid solution (e.g. 0.1M HCl solution). At elevated temperatures, $H_2Ti_3O_7$ NTs can dehydrate and topotactically transform to pure TiO_2 NTs without destroying their nanotubular structure as shown in Figure 2.13. It is reported that anatase (Kasuga et al., 1999; Bavykin et al., 2004; Riss et al., 2009; An et al., 2010), rutile (Lan et al., 2005), bi-crystalline Degussa P25 (Morgan et al., 2008; Grandcolas et al., 2009), organic Ti species (Peng et al., 2008) and amorphous TiO_2 all can be employing as the starting Ti precursors for preparation of TiO_2 NTs. The photocatalytic activity of TiO_2 NTs strongly depends on the calcination temperatures. Toledo Antonio et al. (2010) reported that TiO_2 NTs calcined at 400^oC showed the highest photocatalytic activity towards destructing blue-69 dye, even better than Degussa P25. A post-treatment of $H_2Ti_3O_7$ NTs with Ti-containing sol was developed in the work reported by An et al. (2008) and the resulted TiO_2 NTs calcined at 400^oC showed enhanced thermal stability and thus higher photocatalytic activity under UV irradiation.

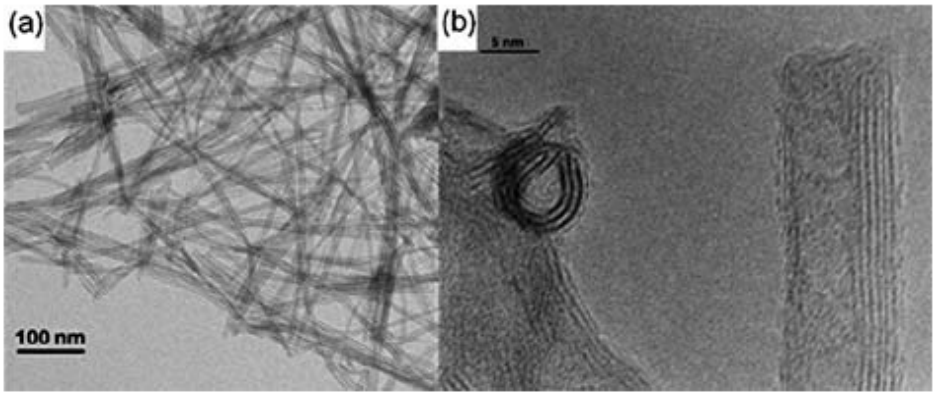

Figure 2.13 TEM (a) and radial and axial cross-sectional HRTEM images (b) of TiO_2 nanotubes synthesized via an alkaline hydrothermal treatment of anatase TiO_2 in 10 M NaOH solution at 120-140^{o}C (Bavykin et al., 2004).

2.3.5 Porous industrial photocatalysts

While numerous porous TiO_2-based materials with tailored physicochemical properties and demonstrated photocatalytic activities have been reported, most of these materials are fine powders. Such fine particle size suspended in water always requires a separation unit to recovery the solid from the medium, resulting in operation complexity and additional cost. Over the past decade, a great deal of research interest has been spent on designing industrial TiO_2-based photocatalysts by, for instances, supporting TiO_2 particles on large-surface-area porous solids, fabricating porous TiO_2 thin films on various substrates, or grafting TiO_2 nanoparticles on membranes.

2.3.5.1 TiO_2 supported on porous solids. Various porous solids, including microporous zeolites (Xu and Langford, 1995; Xu and Langford, 1997; Li et al., 2007a), clays (Li et al., 2007a), activated carbon (Tryba et al., 2003), mesoporous silicas (Reddy et al., 2004; Inumaru et al., 2005; Li and Zhao, 2006; Zhang et al., 2009a) and sepiolites (Nieto-Suarez et al., 2009) have been employed to support TiO_2-based photocatalysts. It is revealed that using zeolites as supports allowed the

formation of fine TiO_2 particles with a good dispersion and enhanced the adsorption of organic pollutants on TiO_2 (Xu and Langford, 1995; Xu and Langford, 1997). However, the main disadvantage of microporous zeolite supports lies in their small pore sizes, which limit the applications in photo-degradation of large organic molecules. Fortunately, the discovery of highly ordered mesoporous materials broadens the scope (Kresge et al., 1992). SBA-15, a very famous mesoporous silica, has been widely explored as a support of TiO_2 particles and the loading can be achieved by direct synthesis (Li and Zhao, 2006) or postsynthesis (Perathoner et al., 2006; Wang et al., 2007c). For example, Li and Zhao (2006) prepared a series of Ti-loaded SBA-15 using the direct synthesis method. Ti ions and anatase were found in the final products as framework and surface Ti species, respectively, both of which were found to be photocatalytic active. The photocatalytic behavior for degradation of organic wastes was observed to critically depend on the Ti content. An optimal molar ratio of Ti/Si was found to be 0.091 in their work.

Hierarchical macro-, meso-/micro-porous structures showed highly efficient accessibility of reactants to their inner surfaces, thus promoting photocatalytic performances (Yuan et al., 2003; Wang et al., 2005b). Nieto-Suarez et al. (2009) synthesized hierarchical macro-/meso-porous silica-sepiolite composites anchored by P25 (Figure 2.14a and b) via an ice-segregation induced self-assembly process. In their work, colloidal aqueous suspension with P25, sepiolite and silica (SS) were cooled down in liquid nitrogen and the formed ice served as rigid templates for generation of porous structures. The presence of hierarchical structures and the adsorbent of sepiolite provided highly efficient adsorption capability. Furthermore, the loaded Degussa P25 ensured highly efficient photocatalytic degradation of adsorbed organic pollutants (Figure 2.14c and d).

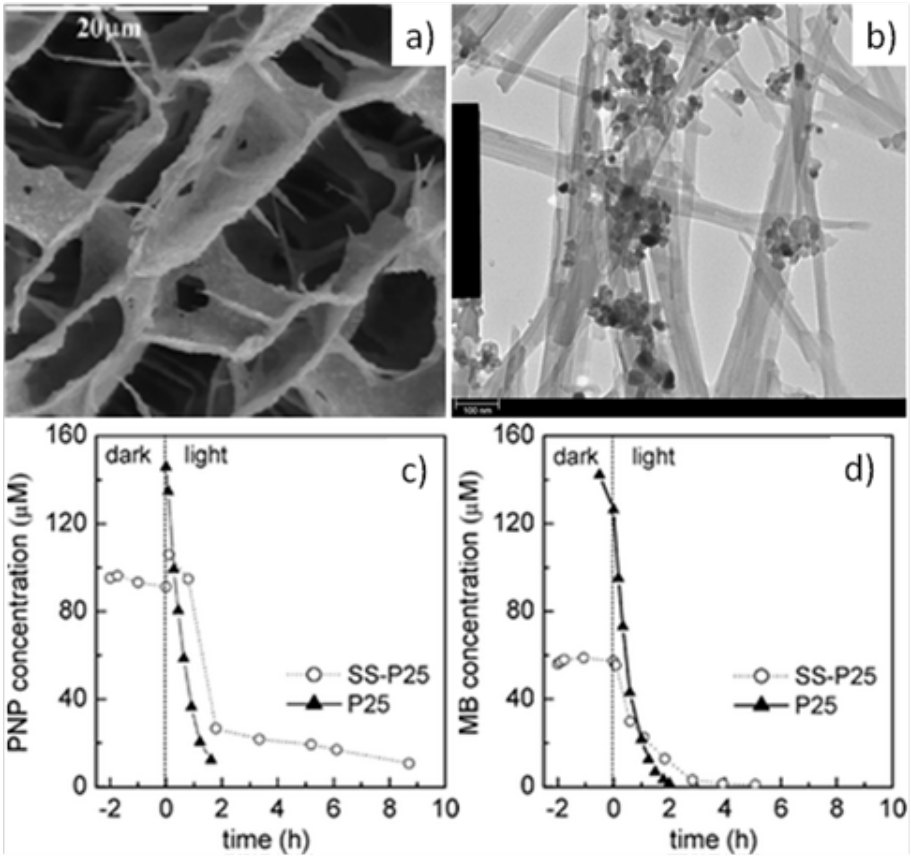

Figure 2.14 (a) SEM micrograph and (b) TEM micrograph of P25 adsorbed on sepiolites fibers, scale bar in (b) is 100 nm ; Plot representing (c) PNP concentration and (d) MB concentration versus irradiation time in solutions containing pristine P25 or SS-P25 composites (Nieto-Suarez et al., 2009).

2.3.5.2 Porous TiO_2 coated on substrates. The most popular method for coating TiO_2 thin films on substrates is the sol-gel process due to its flexibility and versatility (Sanchez et al., 2008). As mentioned above, block copolymer-mediated soft-templating strategy has been developed for the preparation of mesoporous TiO_2 powders (Yang et al., 1998; Yang et al., 1999). In 2001, three research groups prepared mesoporous TiO_2 nanocrystalline thin films with well-defined mesophases using the EISA method in the presence of block copolymers, respectively (Grosso et al., 2001; Yun et al., 2001; Hwang et al., 2001). Precise control over the hydrolysis and polycondensation of Ti species and their cooperative assembly with block copolymers are indispensable for obtaining a highly ordered mesostrucuture. So far,

various mesoporous TiO_2 thin films have been prepared in the presence of Pluronic triblock copolymers (Alberius et al., 2002; Sanchez et al., 2008).

In comparison with nonporous films derived from conventional sol-gel processes, mesoporous TiO_2 films present superior photocatalytic activity mainly due to their large accessible pore surfaces. The photocatalytic activity of mesoporous TiO_2 films is strongly dependent on the specific surface area, pore size, mesophase (Sakatani et al., 2006; Carreon et al., 2007), the crystallinity of pore walls (Sakatani et al., 2006; Tang et al., 2004) and thickness of mesoporous TiO_2 films. Generally, high crystallinity and large surface area benefit the photocatalytic performance. The crystallinity and surface area strongly depend on the calcination temperature. Therefore, there is an optimized calcination temperature for balancing these two parameters. Yu et al. (2004b) observed that mesoporous TiO_2 films showed the best photocatalytic activity when calcined at 500^oC. However, 600^oC and 400^oC were found to be the optimized calcination temperature by Carreon et al. (2007) and Sakatani et al. (2006), respectively. As to the thickness of mesoporous TiO_2 films, it can be controlled by using different materials and preparation methods, or tuning the viscosity of the initial sol solution and the coating time (Choi et al., 2006b; Soni et al., 2008).

Mesoporous TiO_2 films have been coated on various substrates, such as pyrex glass (Carreon et al., 2007; Choi et al., 2006b; Soni et al., 2008), quartz (Yu et al., 2004b), stainless steel (Ortel et al., 2010), and silicon (Sakatani et al., 2006; Soni et al., 2008). The roughness, composition, microstructure, as well as the thermal and chemical stability of the substrates have been demonstrated to have crucial influences on the crystallinity, mesostructural ordering, component purity and uniformity of resultant coating (Ortel et al., 2010; Zhang et al., 2006). For instance, Zhang et al. (2006) found

that a transition in the pore configuration took place from a cubical configuration to cage-like arrays, accompanied by an increase in crystallinity of anatase, when the substrate was changed from amorphous glass to polycrystalline Pt and then to single-crystal Si(111).

Mesoporous TiO_2-based films have been synthesized to further improve the photocatalytic activity by depositing noble metal nanoparticles (Yu et al., 2004a; Wang et al.,2005a; Bannat et al., 2009), or coupling with metal oxide semiconductors (Pan and Lee, 2006), or surface functionalization (Yu et al, 2003; Wang et al., 2005d). To enhance the photoresponsive range, visible-light-active mesoporous N-doped TiO_2 films have been synthesized by direct chemical synthesis (Soni et al., 2008) or by annealing in NH_3 gas (Martinez-Ferrero et al., 2007). Besides, highly ordered cubic mesoporous CdS/TiO_2 and $CdSe/TiO_2$ films were synthesized by thermal treatment of Cd^{2+}-doped TiO_2 films with selenium or sulfur vapour, and found to show an enhanced sensitivity to visible light (Bartl et al., 2004).

Other than Pluronic-type triblock copolymers, several PEO-based diblock copolymers have been designed and synthesized for the templating construction of mesoporous TiO_2 thin films (Groenewolt et al., 2005; Cheng et al., 2006).

2.3.5.3 TiO_2 grafted on membranes. Coupling photocatalysis with membrane technology has received increasing attention since the pioneer work of Anderson et al. (1988). Such integrations could completely eliminate the photocatalysts separation/recovery process. As for membranes, the presence of grafted photocatalysts endows them with the photocatalytic and antifouling functions, leading to a higher permeability, a lower operating pressure, and certainly a better water quality.

Polymeric membranes are widely used in the current water treatment industry. Due to the poor thermal and chemical stability of the polymer membranes, conventional sol-gel process needs organic solvent and calcination is not suitable for the deposition of photocatalysts. Grafting of TiO_2 nanoparticles has been thus designed to fabricate TiO_2/polyamide membranes by self-assembly of TiO_2 nanoparticles on the surface of the membrane (Kwak et al., 2001; Kim et al., 2003). The prepared hybrid membrane showed slight increase in water flux and salt rejection in comparison with the pure polymer membrane. The antibacterial fouling ability and the stability of the TiO_2 nanoparticles under the operation conditions were verified by measuring the viable numbers and determining the survival ratios of the *Escherichia coli* (*E. coli*). The photocatalytic bactericidal efficiency was remarkably enhanced for the hybrid membrane under UV illumination. Nevertheless, the organic membranes always encounter problems, such as instability under UV light and unsuitability under harsh conditions (Molinari et al., 2000).

Inorganic membranes, e.g. Al_2O_3 membrane, do not have the problems of polymer membranes (Bosc et al., 2005). Choi et al. (2006b; 2007) deposited mesoporous anatase TiO_2 thin layers on Al_2O_3 membranes by employing Tween 80 surfactant as a mesopore-directing agent along with acetic acid-based sol-gel dip-coating route. The resultant TiO_2/Al_2O_3 composite membranes exhibited efficient photocatalytic performances in both degrading biological toxins and inactivating microorganisms. However, the photocatalytic membranes displayed a nearly 40% decrease in permeability coefficient. To improve the photocatalytic activity and permeability of the composite membrane, a hierarchical mesoporous film with multilayer TiO_2 on Al_2O_3 membrane was designed (Choi et al., 2006a). The pore size stepwisely decreased from the bottom to the top layers. Such multilayer coating was

demonstrated to enhance the membrane flux without sacrificing the cut-off molecular weight.

2.4 Novel TiO_2-Graphene nanocomposite photocatalysts

Graphene (G) is a flat monolayer of carbon atoms tightly packed into a two-dimensional (2D) hexagonal lattice (Geim and Novoselov, 2007). Recently, graphene-containing composite materials have been attracting extensive attention, e.g. TiO_2/graphene nanocomposites for photocatalytic applications (Peng et al., 2008; Akhavan and Ghaderi, 2009; Zhang et al., 2010; Ng et al., 2010), due to its many unique properties. Generally, the advantages of introducing graphene-based materials into TiO_2 photocatalysts mainly lie in five aspects: (1) much larger surface area (theoretical value of graphene, 2630m^2/g); (2) higher mobility of charge carriers; (3) better affinity to organic wastes molecules through specific π-π interactions; (4) more easier sensitizing property under solar light irradiation; (5) outstanding mechanical and thermal properties (Geim and Novoselov, 2007). The synthesis approaches of TiO_2/graphene composites from Ti precursors and graphene oxide (GO), which can be prepared through Hummers and Offeman's method (1958), are roughly divided into four categories, including chemical reduction, thermal annealing, photocatalytic reduction and hydrothermal dehydration route.

Zhu et al. (2010) developed a facile one-pot chemical reduction route to prepare TiO_2/graphene composite nanosheets by employing $TiCl_3$ as Ti precursor as well as the reducing agent. The sample exhibited enhanced photocurrent response. Besides, TiO_2/graphene composites can also be prepared by thermal annealing (Lambert et al., 2009; Wang et al, 2009b). In order to achieve thermal reduction of graphene oxide,

the annealing temperature employed is usually very high, e. g. 1100^{o}C (Lambert et al., 2009).

The third and the most popular strategy is photocatalytic reduction of graphene oxide in the presence of TiO_2 suspension developed by Kamat's group (Williams et al., 2008). TiO_2 photocatalysts will generate electron and holes under UV light irradiation. The accumulated electrons will serve to reduce graphene oxide (GO) to reduced graphene sheets (RGO) in solution if the holes are scavenged by ethanol. Soon afterwards, TiO_2-graphene thin films prepared by this photocatalytic reduction method were found to be more promising than bare TiO_2 in the remediation of contaminated water through photo-degradation of organic wastes (Ng et al., 2010) and photo-killing bacteria under solar light irradiation (Akhavan and Ghaderi, 2009).

Hydrothermal dehydration method means that supercritical water (SC) serves as the reducing agent to achieve the reduction from exfoliated graphene oxide to graphene (Zhou et al., 2009). Soon afterwards, Zhang et al. (2010) successfully synthesized P25-graphene composite by direct hydrothermal treatment of P25 powders and graphene oxide in water-ethanol system. P25 was chemically bonded on the surface of graphene and concentrated along the wrinkles (Figure 2.15a and b). The P25-graphene composites (P25-GR) exhibit more excellent adsorptivity and higher photocatalytic activity towards destructing organic molecules under both UV irradiation and visible light irradiation than P25 and P25-carbon nanotubes (P25-CNTs) (Figure 2.15c and d). Besides, TiO_2 nanotubes-graphene and TiO_2 nanorods-graphene were also fabricated via alkaline hydrothermal treatment of Ti-containing GO in 10 M NaOH solution, and found to be excellent photocatalysts (Peng et al., 2008).

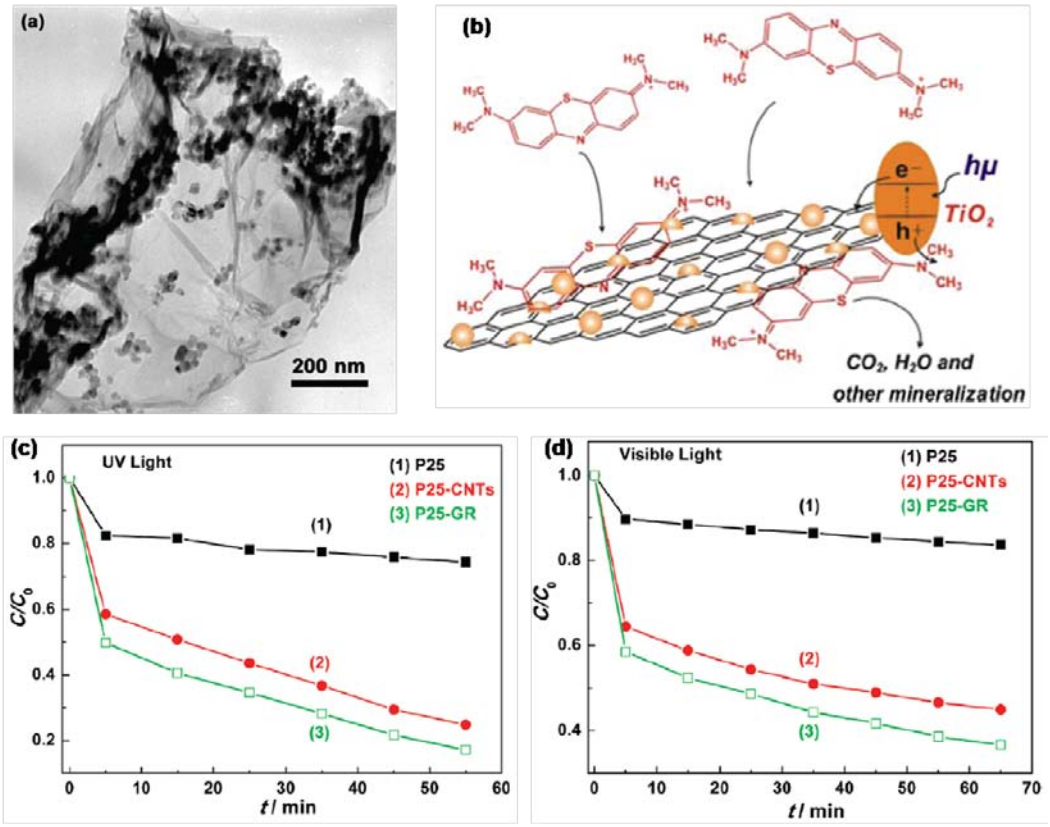

Figure 2.15 (a) Typical TEM image of P25-GR; (b) Schematic structure of P25-GR and tentative processes of the photodegradation of methylene blue (MB) over P25-GR; Photodegradation of methylene blue under (c) UV light and (d) visible light (λ>400 nm) over (1) P25, (2) P25-CNTs, and (3) P25-GR photocatalysts, respectively (Zhang et al., 2010).

CHAPTER 3

EXPERIMENTAL SECTION

3.1 Reagents and apparatus

The chemicals and apparatus employed in this master thesis project are summarized in Table 3.1 and Table 3.2, respectively. All the chemicals were used as received without further purification.

Table 3.1 Reagents used for synthesis of TiO_2-based photocatalysts

Chemicals	Grade	Supplier
P25	80 wt.% anatase, 20 wt.% rutile	Degussa
Titanium tetrachloride	99.95	Aldrich
Titanium tetraisopropoxide	98%	Aldrich
Dodecyl amine	98%	Aldrich
Urea	99.5%	Merck
Tetraethylammonium hydroxide	35%	Alfa Aesar
2-propanol	99.7%	Merck
Ethanol	99.50%	Aldrich
Orange II	85%	Sigma
Sodium hydroxide	AG (99.9%)	Merck
Hydrochloride acid	GR (37%)	Merck
Gold(III) chloride hydrate	99.999%	Aldrich

Table 3.2 Apparatus used in this master thesis project

Apparatus	Model or Specification	Manufacturer
Autoclave	Stainless steel lined with Teflon	Self-made
Oven	Binder FD240	Fisher Scientific
Vacuum pump	Thomas 2522C-02	Welch Vacuum
Balance	AND GF-2000 (0.5-2100 g)	Goldbell Weigh-System
Balance	AB204-S (10 mg-220 g)	MonoBloc Weighing Technology
Hot Plate & Magnetic stirrer	KMC-130SH	Vision Scientific
Muffle Furnace	CWF1100	Carbolite
Ultrosonics	Transsonic 460/H	ACHEMA
UV-lamp	HPR 125 W	Phillips
Xenon lamp	350W	Stonetech Electric
Peristaltic pump	Masterflex L/S	Cole-Parmer
UV-VIS spectrophotometer	UV-1601/3101	Shimadzu
pH meter	Ioncheck 10	Radiometer Analytical
Centrifuge	CT15RT	Techcomp
TOC analyzer	5000A	Shimadzu
Photoreactor	SGY-II	Stonetech Electric

3.2 Synthesis route of modified TiO_2-based photocatalysts

3.2.1 Hydrothermal synthesis of mesoporous tri-crystalline TiO_2 photocatalysts

The mesoporous tri-crystalline TiO_2 photocatalysts were prepared by a soft template method, based on the novel concept of "acid-base pairs" (Tian et al., 2004). Titanium tetrachloride ($TiCl_4$) and titanium tetraisopropoxide (TTIP) were selected as Ti precursors while urea was used as the additive, respectively. In a typical synthesis, 3g $TiCl_4$ was quickly dissolved in 20g deionized water. Then, 1.55g dodecyl amine and 1g urea were dissolved in this $TiCl_4$ solution under magnetic stirring for 30min, generating a homogeneous solution. Subsequently, the TTIP (4.75g) dissolved in 2-propanol (10g) was added dropwise into the solution just prepared. The sol was stirred for 1h at ambient temperature and then 3h at 40^oC. After that, the so-called gel was transferred into a 55ml stainless steel autoclave lined with Teflon and kept at 100^oC for 24h. After filtrated and rinsed with ethanol 3 times by using a vacuum pump, the sample was collected from the filtration membrane (0.45μm) and then dried at ambient temperature overnight. Lastly, the white powder was calcined at 350^oC for 8 hours in air with a ramping rate of 1^oC/min to remove the organic surfactant. Different weights of urea were used to vary the phase content of mesoporous tri-crystalline TiO_2 photocatalysts. The samples thus obtained are denoted as TiO_2-*s* where *s* represents weight of urea. Besides, the effect of $TiCl_4$, calcination temperatures and other additive, tetraethylammonium hydroxide (TTEA), were also explored in this section.

3.2.2 One-pot hydrothermal synthesis of visible-light-activated TiO_2-Au nanotubes

The synthesis of TiO_2-based nanotubular photocatalysts was conducted by using a modified alkaline hydrothermal method reported in the literature (Grandcolas et al., 2009). A typical synthesis procedure is described as follows: 0.48g Degussa P25 powders were added to 35mL 10M NaOH solution, followed by sonication for 10 min to completely disperse the solid powders. Then 0.3ml $HAuCl_4$ solution was added dropwise into the P25 suspension just prepared, in which the molar ratio of Au/Ti equals to 0.1%. After magnetically stirred for 1h at ambient temperature, the solution was then transferred to into a 55ml stainless steel autoclave lined with Teflon and kept at 150^{o}C for 16h. Subsequently, the fuchsia powder was rinsed by 0.1M HCl and D.I. water for four times, respectively. Then the sample collected was dried at 60^{o}C overnight. Lastly, the powder was calcined at 350^{o}C for 4 hours in air with a ramping rate of 5^{o}C/min to achieve the conversion from $H_2Ti_3O_7$-Au nanotubes to TiO_2-Au nanotubes. Different volumes of $HAuCl_4$ solution were used to vary the loading amount of Au nanoparticles. The samples thus obtained are denoted as TiO_2-Au-*x*%, where *x*% represents the molar ratio of Au/Ti. The naked TiO_2 nanotubes without loading Au nanoparticles were also prepared as a reference material by the similar method.

3.3 Characterization

3.3.1 Thermogravimetric analysis (TGA)

TGA was conducted on a thermogravimetric analyzer TGA 2050 (Thermal Analysis Instruments, USA) under air with a flow rate of 100 mL/min to investigate

the thermal behaviors of the samples. Around 10 mg sample was used and heated from room temperature to 600^{o}C with a heating rate of 10^{o}C min.

3.3.2 X-ray diffraction (XRD)

X-ray diffraction (XRD) takes advantages of the coherent scattering of x-rays by polycrystalline materials to obtain a wide range of structural information. The x-rays are scattered by each set of lattice planes at a characteristic angle, and the scattered intensity is a function of the amount of atoms, which occupy those planes. The scattering from all the different sets of planes results in a pattern, which is unique to a given compound. The structures of the prepared TiO_2-based photocatalysts in this thesis were measured by Shimadzu XRD-6000 diffractometer (CuKα radiation, λ=1.5418Å) operated at 40 kV and 30 mA. The scan range is 5.00-80.00 (deg) and the scan rate is 3.00 (deg/min).

3.3.3 Physical adsorption of N_2

Physical adsorption of N_2 technique is considered as a reference analytical approach to characterize the micro- and mesoporous parameters, including the specific surface area, pore size distribution and pore volume. In this project, it was carried out on an automatic volumetric sorption analyzer (Quantachrome, NOVA 1200). The sample was degassed at 200^{o}C for 3h in a vacuum chamber before measurement so as to remove any absorbed molecules from its surface. By determining the adsorbed volume of N_2 at controlled partial pressure of N_2 at around 77 K, the adsorption/desorption isotherm data was collected. The specific surface area was calculated by employing the multiple-point Brunauer-Emmett-Teller (BET) model in the relative pressure of 0.05-0.3 while the pore size distributions were obtained by using the Barrett-Joyner-Halenda (BJH) method on the desorption branch

of the isotherm. Besides, the total pore volume was determined from the volume of nitrogen adsorbed at the highest relative pressure of ~ 0.95.

3.3.4 Field-emission scanning electron microscope (FESEM)

The morphologies of TiO_2-based photocatalysts were imaged by using a field emission scanning electron microscopy (FESEM) (JEOL-6700F, Japan INC), which was operated at accelerating voltage 10 kV and filament current of 60 mA. Before measurement, the sample was stuck onto a double-face conducted tape mounted on a metal stud and coated with platinum with a sputter coater (JEOL JFC-1300 Auto fine coater).

3.3.5 Transmission electron microscope (TEM)

The microscopic features of the samples were observed with TEM. Before measurement, the sample was dispersed in ethanol and then dripped and dried on a copper grid. In this project, the TEM images were obtained on a JEOL 2010 and JEM 2010F transmission electron microscope, operated at an acceleration voltage of 200 kV.

3.3.6 X-ray photoelectron spectroscopy (XPS)

XPS spectra can be used to identify the chemical compositions of the samples. When a primary X-ray beam of precisely known energy impinges on sample atoms, inner shell electrons are ejected and the energy of the ejected electrons is measured. The concept of binding energy (E_b) of the electron to the atom refers to the difference in the energy of the impinging X-ray and the ejected electrons. Since E_b of the emitted electron depends on the energy of the electronic orbit and the element, it can be used to identify the element involved. Further, the chemical form or environment of the

atom affects the binding energy to a considerable extent to give rise to some chemical shift, which can be used to identify the valence of the atom and its exact chemical form. Thus it is an important technique for determining the origin and the surface amount of the dopants in the TiO_2 matrix. In this thesis project, XPS spectra were obtained by using AXIS HIS (Kratos Analytical Ltd., U.K.) with an monochromatized Al Kα X-ray source (1486.71 eV protons), operated at 15 kV and 10 mA. Wide scan spectra in the binding energy range of 1100-0 eV were recorded in 1 eV step size with pass energy of 80 eV. High resolution spectra of the specific elements were recorded in 0.05 eV steps with pass energy of 40 eV. The calibration of binding energy (BE) was referenced to the C_{1s} corresponding to graphitic carbon at 284.6 eV.

3.3.7 Diffusive reflectance UV-Vis spectrophotometer (DR-UV)

The diffusive reflectance data, which can be used to characterize the optical properties of the TiO_2-based photocatalysts, was collected from Shimadzu UV-3101PC UV-VIS-NIR Scanning Spectrophotometer with an ISR-3100 integrating sphere attachment (for solid samples) or Shimadzu UV-3600 UV-VIS-NIR Spectrophotometer. The wavelength range is 200nm-800nm. The samples were pressed as a pellet sealed with a glass cover to maintain an inert atmosphere and a barium sulphate pellet was used as an internal reference.

3.4 Evaluation of photocatalytic activity and antibacterial property

3.4.1 Semi-batch swirl flow reactor

Orange II, with a molecular formula of $C_{16}H_{11}N_2NaO_4S$, is widely used in the textile industry and it is a non-biodegradable synthetic dye. The photocatalytic

performance of the mesoporous tri-crystalline TiO_2 photocatalysts was evaluated by monitoring the degradation of this representative organic compound under UV irradiation according to the procedure reported in the literature (Li et al., 2007a). The experimental set-up (semi-batch swirl flow reactor) is shown in Figure 3.1. In this part, a 125 W HPR mercury vapor lamp (Philips, Belgium) peaking at 365 nm was chosen as the UV light source and compressed air as its coolant gas.

Briefly, 300mL orange II working solution (20ppm) was firstly put into the reservoir, which was maintained at ambient temperature by coolant water, under magnetic stirring for 30min. The peristaltic pump pushed the working solution into the reactor. Then 180mg synthesized photocatalyst was added into orange II solution without UV irradiation for 30min. After adsorption equilibrium, UV light was switched on. A sample volume of 5 mL was collected at specific time interval by a syringe and filtered with Millex Millipore filter (0.1 μm) to remove the photocatalyst before analysis. The concentrations of orange II were measured by employing a UV-Vis spectrophotometer (UV-1601, Shimadzu). The wavelength of the spectrophotometer was set at 484.5 nm.

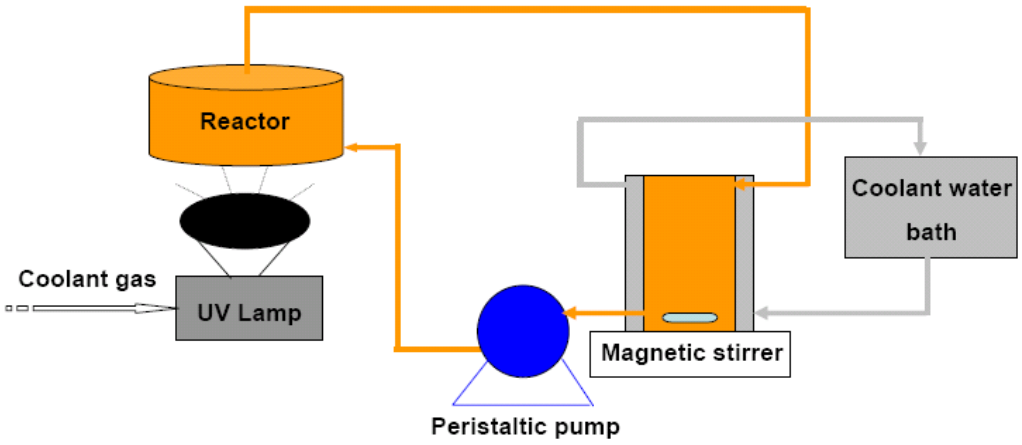

Figure 3.1 Schematic diagram of the photodegradation experimental set-up I: Semi-batch swirl flow reactor.

3.4.2 SGY-II Photoreactor: Open thermostatic batch reactor

Photocatalytic degradation of Orange II over Au-loaded TiO_2 NTs under visible light irradiation was carried out in an open thermostatic batch photoreactor (SGY II system). A 350 W Xenon lamp equipped with a 420 nm cut-off filter was chosen as the visible light source while both compressed air and cycling water as its coolant.

Before visible light irradiation, a suspension containing 200 mL of 5ppm Orange II solution and 0.2 g of solid photocatalyst was sonicated for 5 min and stirred for 30 min in the dark to allow sorption equilibrium. Then the Xenon light was switched on. At a given time interval of irradiation, 5 mL aliquots were withdrawn and filtered with Millex Millipore filter (0.1 μm). The concentrations of orange II were measured by employing a UV-Vis spectrophotometer (UV-1601, Shimadzu).

3.4.3 Recycle test

The recycle test of the TiO_2-Au-*x*% NTs under visible light irradiation was conducted by using the thermostatic batch photoreactor (SGY II system) as follows. 0.2g of photocatalyst TiO_2-Au-0.25% NTs was suspended in 200 mL of 5ppm Orange II solution. After 0.5h for sorption equilibrium under dark environment and subsequent 3.5h for visible light irradiation, switch off the Xenon light. 5 mL aliquots were withdrawn from supernatant after 0.5h waiting for the sedimentation of photocatalysts, filtered and analyzed on the UV-Vis spectrophotometer. Then 5 mL of concentrated Orange II solution with a proper concentration was supplied to the reactor in order to restore the initial concentration of Orange II (5ppm). Then start the subsequent run by following the same procedures just mentioned.

3.4.4 Evaluation of photocatalytic antibacterial property

The photocatalytic antibacterial activity of TiO_2-Au-0.25% NTs was carried out in an open thermostatic batch photoreactor by using *Escherichia coli* (ATCC 700926) as an indicator bacterium. Before each experiment, all utensils were autoclaved at 121 ^oC for 15 min to ensure sterility. *E. coli* was inoculated into a Luria Bertani medium (LB) and grown for 12 h at 37 ^oC on a rotary shaker at 150 rpm. The cells were then harvested by centrifugation at 4000 rpm for 10 min, washed twice with sterile phosphate buffer saline (PBS, 0.03mol/L, pH 7.2) to remove the nutrient, and the resulting pellets suspended again in a sterile PBS buffer to get an *E. coli* stock suspension. The initial concentrations of *E. coli* used in this study ranged from 10^8 to 10^9 CFU/mL, which were prepared by diluting the stock suspension.

A diluted cell suspension and the solid photocatalyst were mixed completely in a sterilized 100 mL glass conical flask with a cover under room temperature. A 350 W Xenon lamp equipped with a 420 nm cut-off filter was used as the visible light source. The *E. coli*/photocatalyst suspension was continually stirred (using a magnetic stirrer) throughout the experiment to ensure homogeneity. Aliquots of 100 μL of the suspension were sampled at pre-determined intervals and diluted 10-fold with PBS (ensuring cells were well suspended by vortex mixing each dilution before transfer), then spread on Petri dishes that had been previously coated with nutrient agar and incubated for 18 h at 37℃ prior to counting the colonies formed and calculating the number of active cells. Triplicate plates were used at each dilution and the counts on the three plates were averaged. Control experiment was conducted in the absence of solid photocatalyst.

CHAPTER 4

SYNTHESIS, CHARACTERIZATION AND HIGHLY PHOTOCATALYTIC PERFORMANCE OF MESOPOROUS TRI-CRYSTALLINE TiO_2

4.1 Introduction

Phase junction, generated from contacting of different polymorphs of TiO_2, always produces intriguing effects on charge carrier transfer processes in photocatalytic applications (Ding et al., 2000; Kawahara et al., 2002; Yang et al., 2009). On the other hand, mesoporous TiO_2 materials possessing high density of active centers owing to their high specific surface area, together with well ordered structures are highly attractive as photocatalysts (Yu et al., 2004b; Li et al., 2007b; Ismail et al., 2010). Therefore, in order to further improve the photocatalytic performance of TiO_2 materials, highly effective P25-like bi-crystalline TiO_2 photocatalysts in terms of powders or thin films with ordered mesoporous structures and fine control of the phase content are highly desired and thus attracted much attention in the past decade; for instance, Chen et al. (2007) prepared a series of mesoporous bi-crystalline TiO_2 photocatalysts with different phase content by tuning the molar ratio of the so-called "acid-base pair" Ti precursors $TiCl_4$ and $Ti(OBu)_4$. The sample with anatase/rutile (82:18, w/w), the phase content of which was nearly the same with that of Degussa P25 (80/20, w/w), was demonstrated to exhibit the highest photoactivity for phenol degradation.

More interestingly, tri-crystalline TiO_2 photocatalysts (anatase-rutile-brookite) with or without mesoporous structures have been successfully fabricated in some cases (Yu et al., 2002a; Luo et al., 2003; Yu et al., 2005). It is reported that heat treatment of mesoporous TiO_2 or F-doped TiO_2 materials above 600^oC could generate tri-crystalline TiO_2 photocatalysts (Yu et al., 2005). However, the mesoporous structures collapsed at such high temperatures and resulted in low specific surface area, thus leading to a worse photocatalytic performance than bicrystalline anatase-brookite calcined at lower temperatures. In the work reported by Luo et al. (2003), mesoporous tri-crystalline TiO_2 with anatase/rutile/brookite (48/32/20, w/w/w) could only be synthesized by using water and ethanol as solvents and 6 days aging time. But no photocatalytic activity was reported. Yu et al. (2005) prepared Ag deposited TiO_2 thin films by the liquid phase deposition (LPD) method. With increasing the Ag concentration in the initial solution, the TiO_2 phase in the resulted Ag-TiO_2 photocatalysts was changed from pure anatase to anatase-brookite mixtures and then to anatase-rutile-brookite mixtures. The tri-crystalline Ag-TiO_2 sample was found to show the best photocatalytic performance towards degradation of methyl orange. However, the specific surface area was not reported. Besides, the content of the more active anatase phase was restricted to a very low level (~20%).

To date, limited reports have been published regarding the fabrication, phase tuning and photocatalytic activity of mesoporous tri-crystalline TiO_2 materials. Thus two questions about mesoporous tri-crystalline TiO_2 still remain unclear, which include the following:

(1) How to achieve fine control of its phase composition without loss of its mesoporous structures and which is the key parameter affecting the phase content?

(2) What is the relationship between the phase composition and its photocatalytic activity? Dose the tri-crystalline TiO_2 with its optimal phase content show better photoactivity than pure anatase, rutile and bi-crystalline TiO_2?

To clarify the above-mentioned questions, it is of high significance to develop a synthesis route to achieve tuning the phase composition of mesoporous tri-crystalline TiO_2 easily. In this thesis project, soft-template method in conjunction with additives was applied to prepare tri-crystalline TiO_2 materials with mesoporous structures, large surface areas as well as different phase contents. Its physiochemical and photocatalytic properties under UV irradiation were also investigated in detail. The basic synthesis information of tri-crystalline TiO_2 is listed in Table 4.1.

Table 4.1 Preparation conditions of TiO_2 photocatalysts involved in this work

Samples ID.	Ti Precursors	Additive (g)	Calcination Temperature (^oC)
TiO_2-0	TTIP*/$TiCl_4$	-------	350/8h
TiO_2-1	TTIP*/$TiCl_4$	Urea/1	350/8h
TiO_2-2	TTIP*/$TiCl_4$	Urea/2	350/8h
TiO_2-3	TTIP*/$TiCl_4$	Urea/3	350/8h
TiO_2-4	TTIP*/$TiCl_4$	Urea/4	350/8h
TiO_2-5	TTIP*/$TiCl_4$	Urea/5	350/8h
TiO_2-6	TTIP*	Urea/2	350/8h
TiO_2-2 (450)	TTIP*/$TiCl_4$	Urea/2	450/8h
TiO_2-2 (550)	TTIP*/$TiCl_4$	Urea/2	550/8h
TiO_2-TT	TTIP*/$TiCl_4$	TTEA$^{\#}$/1	350/8h
TiO_2-Ur-TT	TTIP*/$TiCl_4$	TTEA$^{\#}$/1, Urea/1	350/8h

*TTIP: Titanium tetraisopropoxide; # TTEA: Tetraethylammonium hydroxide.

4.2 Characterization and photocatalytic activity of mesoporous tri-crystalline TiO_2

Mesoporous ternary or binary mixtures TiO_2 were prevalently obtained by tuning the amount of additive urea from 0-5g in the mother sol (TiO_2-s, s=0-5).

4.2.1 TGA investigation

Thermogravimetric analysis (TGA) is carried out over one typical mesoporous tri-crystalline TiO_2 to evaluate the thermal stability of these samples. Figure 4.1 shows the TGA curve of TiO_2-0 dried at ambient temperature without further calcination treatment. It can be seen that the major weight loss, which suggests the removal of absorbed water, the template and other organic species, occurs below 350^{o}C. Thus 350^{o}C is selected as the calcination temperature for the sake of obtaining mesoporous structures and high specific surface area, although the organic template is completely removed at 450^{o}C. The effect of calcination temperature and the nitrogen species left in the porous network will be discussed later.

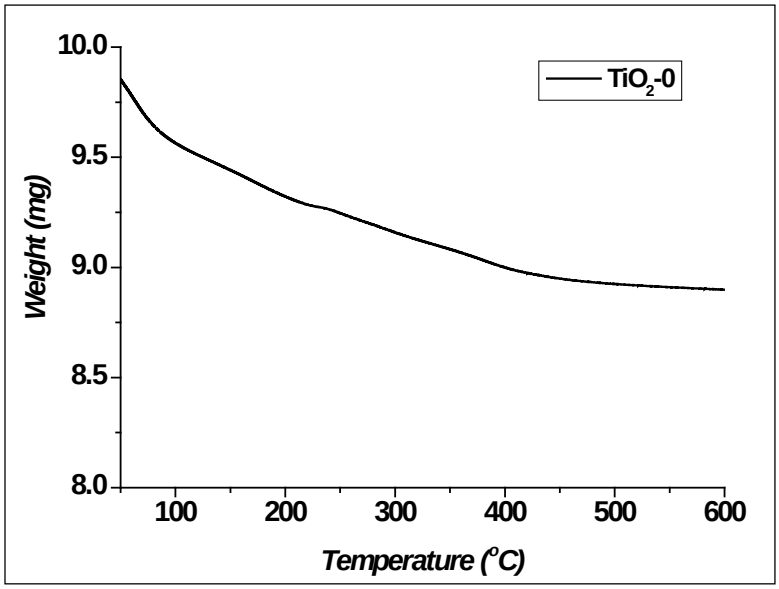

Figure 4.1 TGA spectrum of TiO_2-0.

4.2.2 N_2 adsorption/desorption analysis

N_2 adsorption/desorption isotherms and BJH-PSD curves for the samples TiO_2-s (s=0-5) are shown in Figure 4.2. According to the IUPAC classification, the entire samples exhibit a type IV isotherm with H2 hysteresis loop (~0.5-0.9), which is a characteristic of mesostructured materials (Sing et al. 1985). It is reported that H2 hysteresis loop used to describe the pores with narrow necks and wide bodies (Sing et al. 1985). Besides, the pore size distribution is very narrow for each sample (all the peaks centred on ~3.6-6.6nm).

Textural and structural parameters obtained from the adsorption/desorption data are summarized in Table 4.2. It is noted that the specific surface area remarkablely increases to a high value after the addition of urea in the synthesis process, indicating the important role of the selected additive in this work. The highest specific surface area is 176.05 m^2/g, corresponding to the sample with 4g urea additive. TiO_2-3 possesses a much higher pore volume than other samples, which is possibly due to its larger pore size and higher porosity.

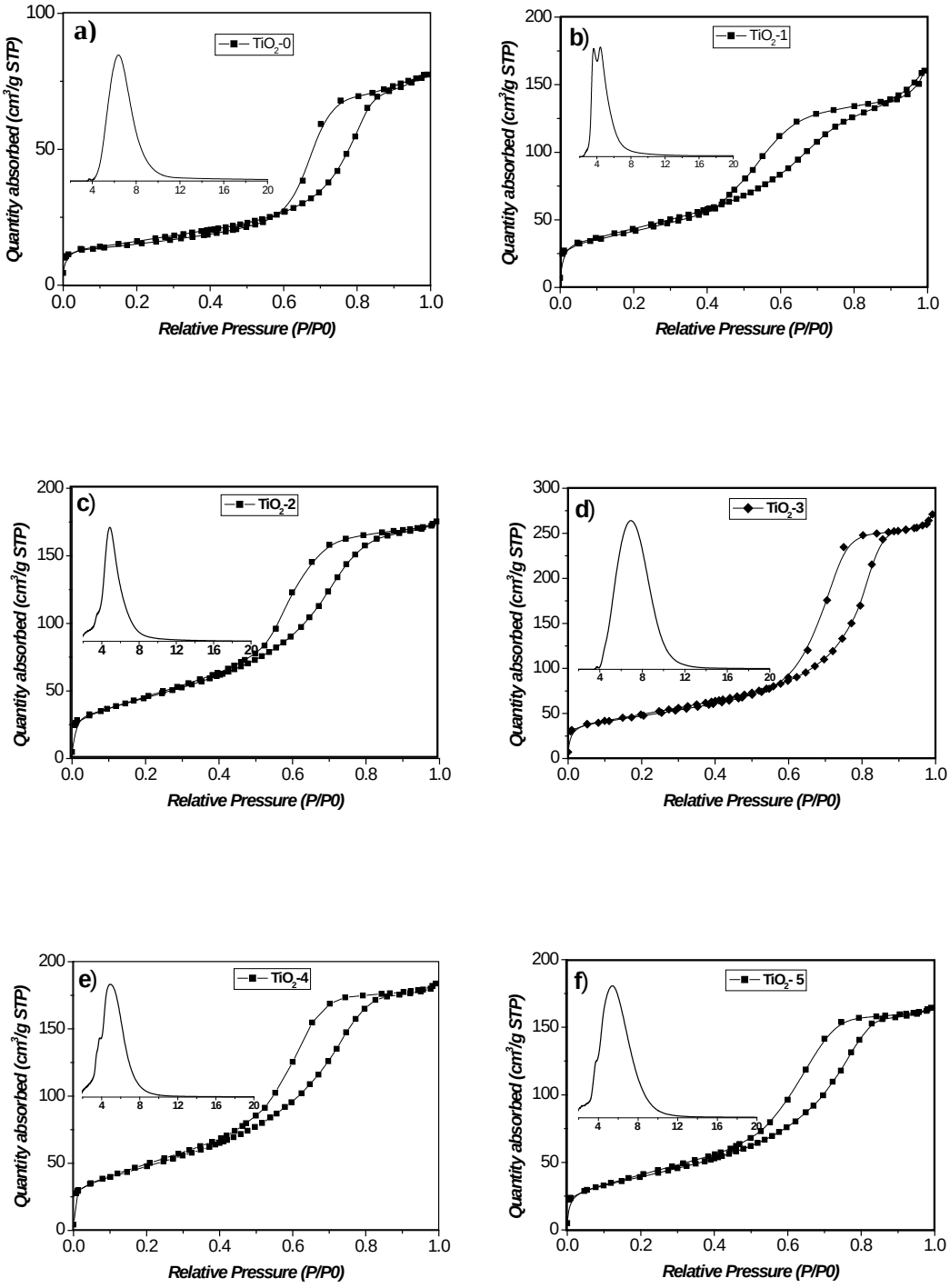

Figure 4.2 (a-f) Nitrogen adsorption-desorption isotherms and corresponding BJH pore size distribution curves (inset) of TiO_2-s (s=0-5).

Table 4.2 Textural and structural parameters of TiO_2-s (s=0-5)

Samples ID.	S_{BET} [a] (m^2/g)	D_{BJH} [b] (nm)	V_t [c] (cm^3/g)
TiO_2-0 (no urea)	56.29	6.6	0.1191
TiO_2-1	156.84	3.6, 4.4	0.2465
TiO_2-2	166.79	4.9	0.2697
TiO_2-3	174.39	6.6	0.4167
TiO_2-4	176.05	4.8	0.2825
TiO_2-5	142.72	5.5	0.2528

[a]BET surface area; [b]pore size distributions determined by the Barrett-Joyner-Halenda (BJH) method; [c]Total pore volume.

4.2.3 X-ray Diffraction results

The tri-crystalline or bi-crystalline structures of the samples TiO_2-s (s=0-5) at room temperature are confirmed by XRD measurements. The corresponding patterns (Figure 4.3) exhibit three main peaks located at $2\theta=25.5^o$, 27.5^o and 30.9^o, that can be indexed as characteristic anatase (101), rutile (110) and brookite (121), respectively. According to Zhang and Banfield (2000), the phase contents in tri-crystalline TiO_2 can be calculated from the following equations and the results are summarized in Table 4.3:

$$W_A = k_A A_A / (k_A A_A + A_R + k_B A_B) \quad (4.1)$$

$$W_R = A_R / (k_A A_A + A_R + k_B A_B) \quad (4.2)$$

$$W_B = k_B A_B / (k_A A_A + A_R + k_B A_B) \quad (4.3)$$

where, W_A, W_R, and W_B are the weight fractions of anatase, rutile, and brookite, respectively, while A_A, A_R, and A_B present the integrated intensities of anatase (101),

rutile (110), and brookite (121) peaks, respectively. k_A (0.886) and k_B (2.721) are two constants.

From Table 4.3, with the increase of urea addition amount, the anatase content becomes larger, while the brookite content decrease. As to the rutile phase, its content becomes smaller at initial and then maintains at around 7 (±1.8) %. It is noted that adding 5g urea can eliminate rutile phase completely, forming a bi-crystalline TiO_2 (anatase-brookite) with the anatase content as high as 84.53%.

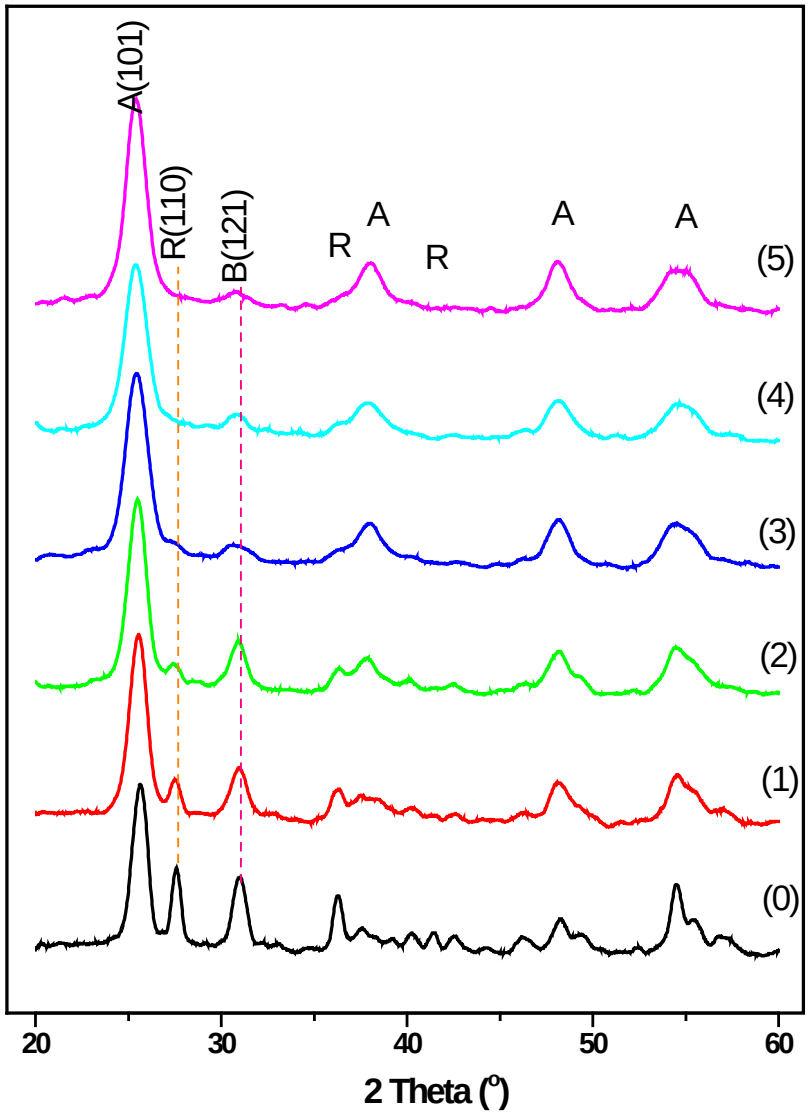

Figure 4.3 Wide-angle X-Ray diffraction patterns of TiO_2-s (s=0-5).

Table 4.3 Weight fractions of each phase in tri-crystalline or bi-crystalline samples TiO_2-s (s=0-5)

Samples ID.	Anatase (%)	Rutile (%)	Brookite (%)
TiO_2-0 (no urea)	40.80	13.75	45.45
TiO_2-1	51.62	7.65	40.73
TiO_2-2	55.47	6.98	37.55
TiO_2-3	72.13	8.76	19.11
TiO_2-4	75.07	6.59	18.33
TiO_2-5	84.53	0.00	15.47

4.2.4 FESEM and TEM investigation

Typical FESEM and TEM images of one typical mesoporous tri-crystalline sample TiO_2-2 are shown in Figure 4.4 (a-c). Form Fig 4.4a, the nanocrystallites in the sample TiO_2-2 are found to be with D_{TEM} of ～10-25 nm, which are very similar with the results calculated from Scherrer Equation (Anatase: 14.5nm, Rutile: 19.4nm and Brookite: 17.9nm).

The existence of mesopores can be confirmed by TEM and HRTEM images (Figure 4.4b and c), but the mesopores are wormhole-like and the distribution of pores is irregular, which is consistent with Yoshitake's work (Yoshitake et al., 2002). Yoshitake et al. (2002) claimed that it was the template dodecylamine that conducted TiO_2 into a wormhole-like structure. Unfortunately, the degree of structural order was very low since there was no obvious peak in the small-angle XRD pattern (not shown). The corresponding selected area electron diffraction (SAED) pattern of TiO_2-2 is shown in Figure 4.4d, which provides another evidence for tri-crystalline structures and is in good agreement with XRD pattern.

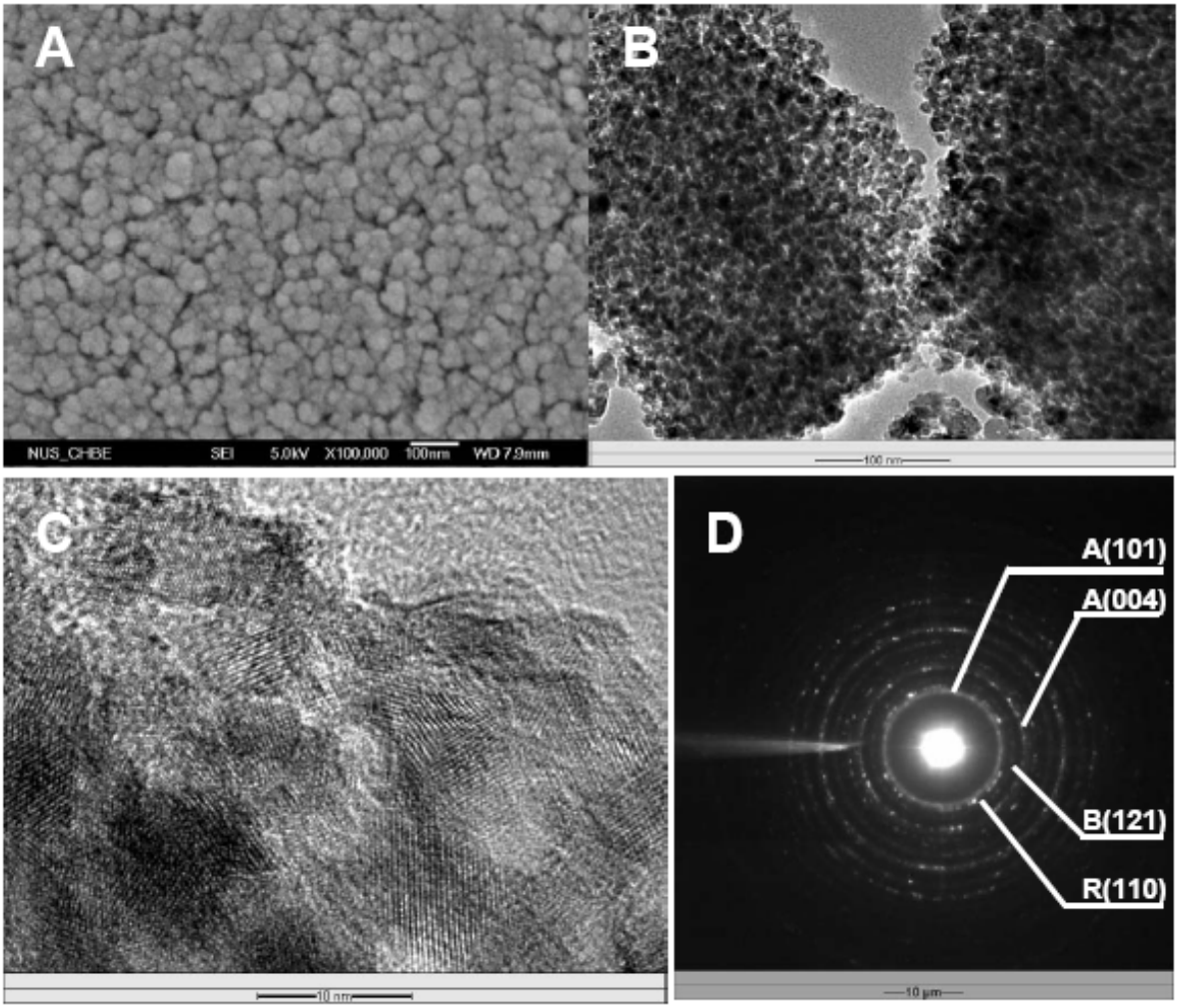

Figure 4.4 FESEM image (A), TEM image (B), HRTEM (C) and selected area electron diffraction pattern (D) of the sample TiO_2-2.

4.2.5 XPS results

Since both the surfactant (dodecylamine) and additive (urea) are N-contained chemicals and the calcination temperature (350^o) is not so high (evidence from Figure 4.1) in order to obtain better mesoporous structure and large surface areas, the synthesized tri-crystalline TiO_2-s may have N dopants. Figure 4.5 shows broad-scan XPS spectrum of TiO_2-0, which has no additive in the synthesis process. There is no obvious peak around 400eV in this spectrum due to the low amount of N. However,

the obvious N 1s feature centred on 399.3eV in the narrow-scan N1s XPS spectra confirms the existence of nitrogen species, generating from the template employed.

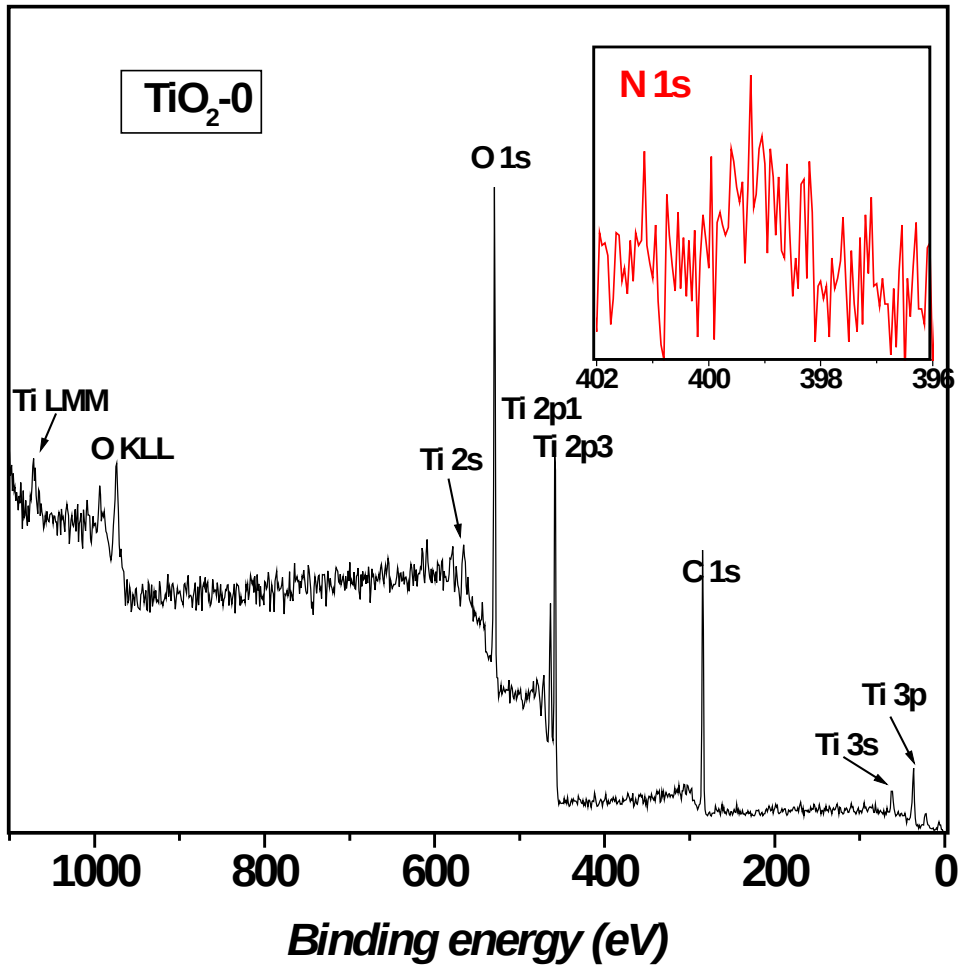

Figure 4.5 Broad-scan XPS spectra and narrow-scan N1s XPS spectra (inset) obtained for TiO_2-0.

The assignment of N 1s XPS peak in N-doped TiO_2 photocatalysts has been previously well discussed in the literature. The feature at ca. 398-399.0 eV was assigned to zero-valent N in NH_3 (Gopinath, 2006) while Yates's group (Diwald et al., 2004) reported that N 1s binding energy of 399.6 eV is due to nitrogen located in an interstitial site and probably bound to hydrogen, like N···H complex. Therefore the

peak centered on 399.3eV in this work is likely due to the interstitial NH_x complex. It is well known that N-doped TiO_2 is a visible-light-active photocatalyst and is reported that it can narrow the band gap (Asahi et al. 2001). Besides, its content may affect the photocatalytic performance. Thus the atomic concentration on the surface of each sample is analyzed and summarized in Table 4.4. It is very interesting that the addition of urea does not affect the surface N content significantly. With the increase of urea amount, the N content is found to be confined in a very narrow region, between 1.12-1.19%. Thus it is concluded that the NH_x complex left in the TiO_2 structure is mainly due to the amine surfactant.

Table 4.4 Atomic concentration data of the samples TiO_2-s (s=0-5)

Samples ID.	O (%)	Ti (%)	N (%)	N/Ti (%)
TiO2-0	71.80	27.07	1.13	4.17
TiO2-1	75.75	23.11	1.14	4.93
TiO2-2	71.64	27.19	1.17	4.30
TiO2-3	75.48	23.33	1.19	5.10
TiO2-4	74.09	24.79	1.12	4.52
TiO2-5	74.31	24.52	1.17	4.77

4.2.6 Photocatalytic properties under UV light irradiation

In this work, the photodegradation of Orange II is employed to evaluate the photocatalytic activities of the tri-crystalline or bi-crystalline samples TiO_2-s (s=0-5). Before UV irradiation, the mixture of Orange II solution and solid photocatalyst is magnetically stirred for 30 min in the dark environment to achieve complete sorption equilibrium. Figure 4.6 shows the photodegradation of Orange II over the sample

TiO_2-2. The intensity gradually decreases with the UV light irradiation time and a slightly peak shift to longer wavelength is observed probably due to the formation of reaction intermediates.

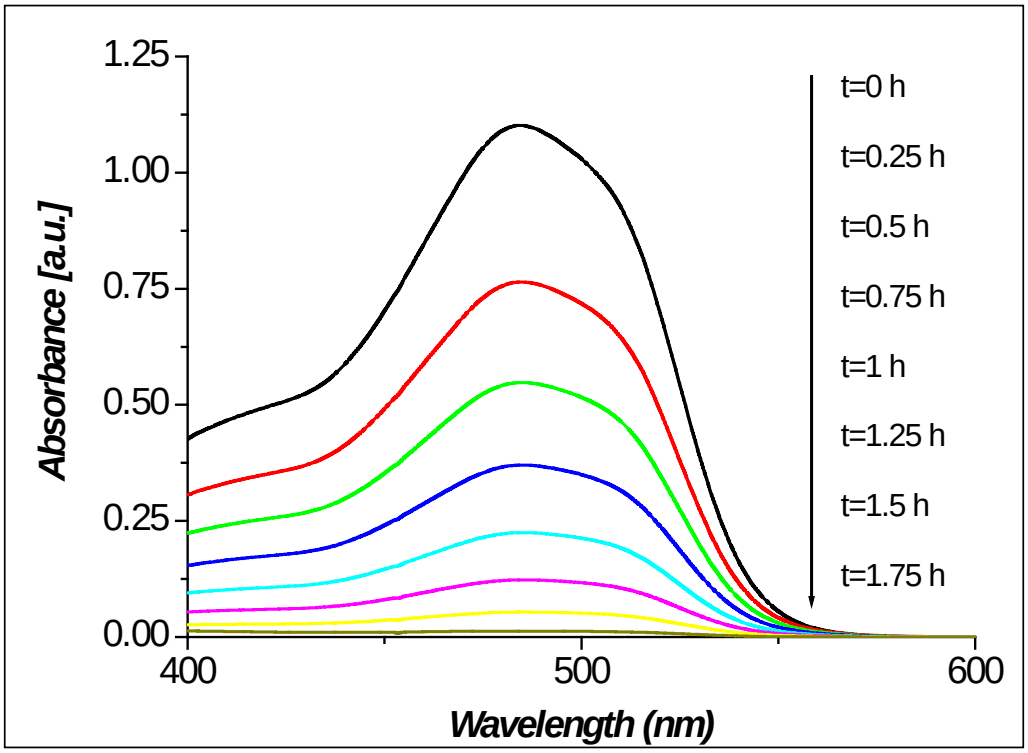

Figure 4.6 Photocatalytic degradation of Orange II over TiO_2-2 with time under UV irradiation (Phillips, HPR 125 W, wavelength centered on 365nm). Experiment condition: semi-batch swirl flow reactor; light intensity: 110w/m^2; catalyst amount: 0.6 g/L; initial concentration of orange II: 20 mg/L.

In Figure 4.7, the photocatalytic performances of the six samples (TiO_2-s, s=0-5) are compared. It is noted that only UV light has no obvious effect on the degradation of Orange II. The sample TiO_2-0 without the addition of urea shows the poorest photocatalytic performance among all the six samples, probably due to the obvious smaller BET surface area and low content of more active anatase phase. The other five samples with additive exhibit improved photocatalytic activities. The sample

TiO_2-2, corresponding to 2g urea additive, possesses the best photocatalytic activity and completely achieved the photo-decloration of Orange II within only 1.75h.

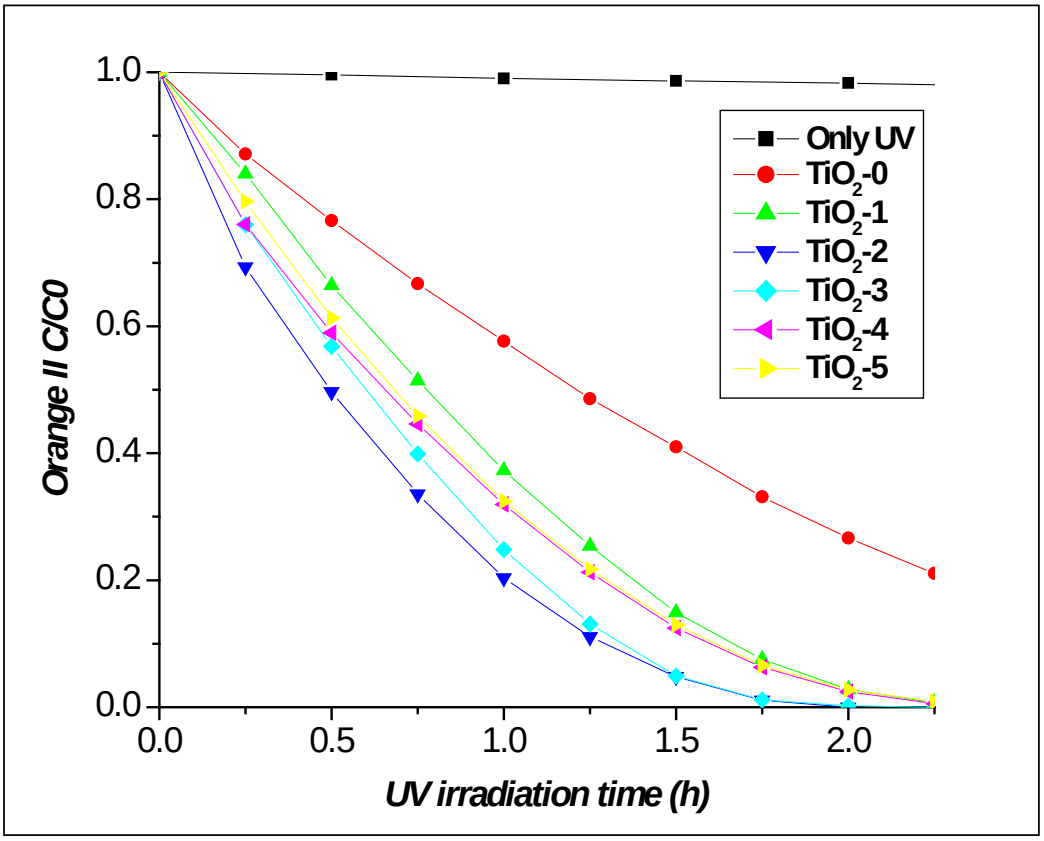

Figure 4.7 Comparison of the Orange II photodegradation activity over TiO_2-s (s=0-5). Experiment condition: semi-batch swirl flow reactor; light intensity: 110w/m^2; catalyst amount: 0.6 g/L; initial concentration of orange II: 20 mg/L.

4.3 Parameters affecting the phase content

4.3.1 The effect of urea and other additive (TTEA)

As discussed in section 4.2, adding urea not only plays an important role for obtaining well mesoporous structures, but also successfully achieves tuning the phase content of tri-crystalline TiO_2 to some extent (percentage of anatase phase from 40% to 85%). More efforts are made to further tune the phase contents, aiming to obtain

tri-crystalline TiO_2 with anatase weight below 40% or pure phases. Fortunately, tetraethylammonium hydroxide (TTEA) is found to be a proper additive to achieve pure rutile TiO_2 (see Figure 4.8c). Furthermore, a combined additive of 1g urea and 1g TTEA can form tri-crystalline TiO_2 with lower anatase content (evidence from Figure 4.8 and Table 4.5). The two samples are thus labelled as TiO_2-TT and TiO_2-Ur-TT, respectively.

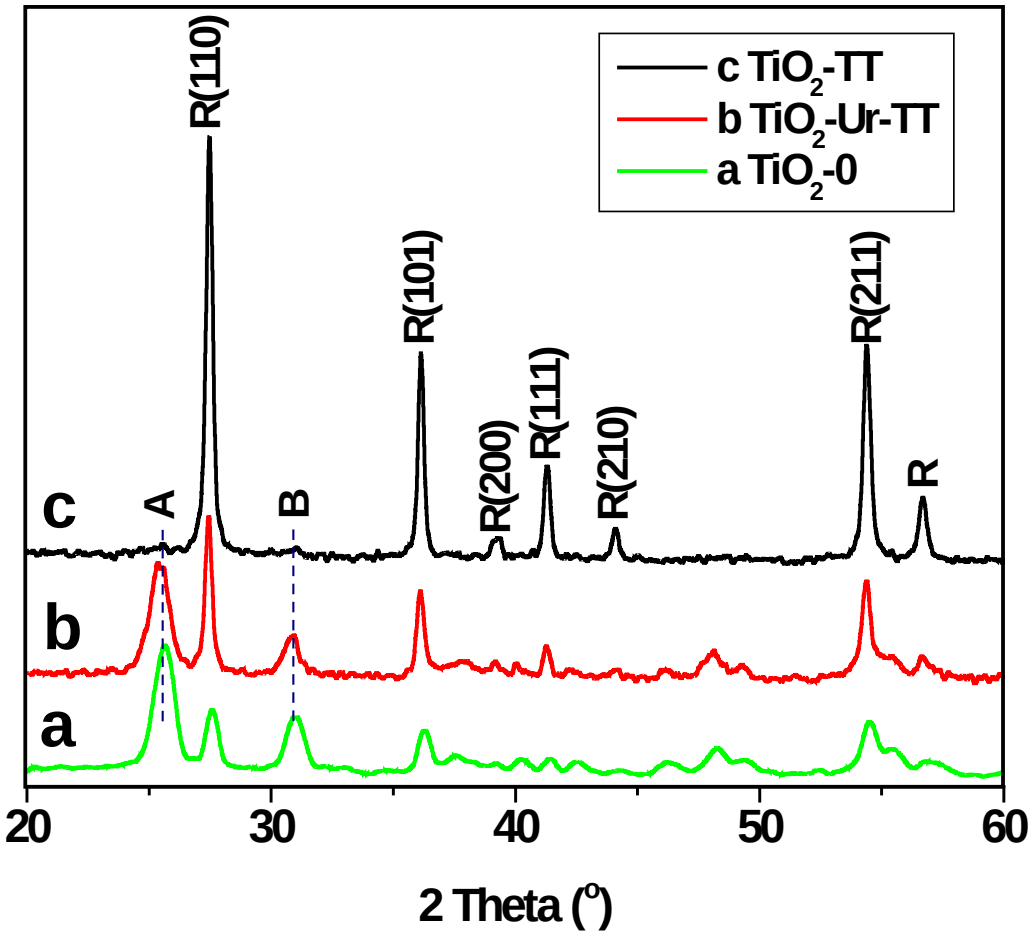

Figure 4.8 Wide-angle XRD patterns of (a) TiO_2-0, (b) TiO_2-Ur-TT, and (c) TiO_2-TT.

Table 4.5 Comparison of weight fraction in TiO_2-TT, TiO_2-Ur-TT and TiO_2-0

Photocatalysts ID.	Anatase (%)	Rutile (%)	Brookite (%)
TiO_2-TT	0	100	0
TiO_2-Ur-TT	32.37	32.29	35.34
TiO_2-0	40.80	13.75	45.45

The porous structures of TiO_2-TT and TiO_2-Ur-TT are also confirmed by nitrogen adsorption/desorption analysis (Figure 4.9). The sample with pure rutile phase shows very broad tri-modal pore size distribution, centred on 2.2nm, 9.6nm and 31.5nm (Figure 4.9a), even extending to the macropores region (>50nm) and resulting in a hierarchical porous TiO_2, which is possibly because that the TTEA also plays a template role in the synthesis process. Besides, the BET surface area for TiO_2-TT is very low, 36.31m^2/g (Table 4.6).

As to the sample TiO_2-Ur-TT with combined additives, the pore size distribution is confined to a narrow region centred on 7.9nm (Figure 4.9b) and the BET surface area is also significantly increased to 69.34m^2/g, which also supports the conclusion that urea plays an important role in controlling the porous structures and improving the BET surface area.

TTEA is also an N-contained chemical. Similarly with additive urea, the addition of TTEA does not result in any obvious change of the surface nitrogen content. However, the photocatalytic performance of TiO_2-TT and TiO_2-Ur-TT are found to be very poor compared with the samples TiO_2-s (s=0-5), which is probably due to the low surface area and low content of anatase.

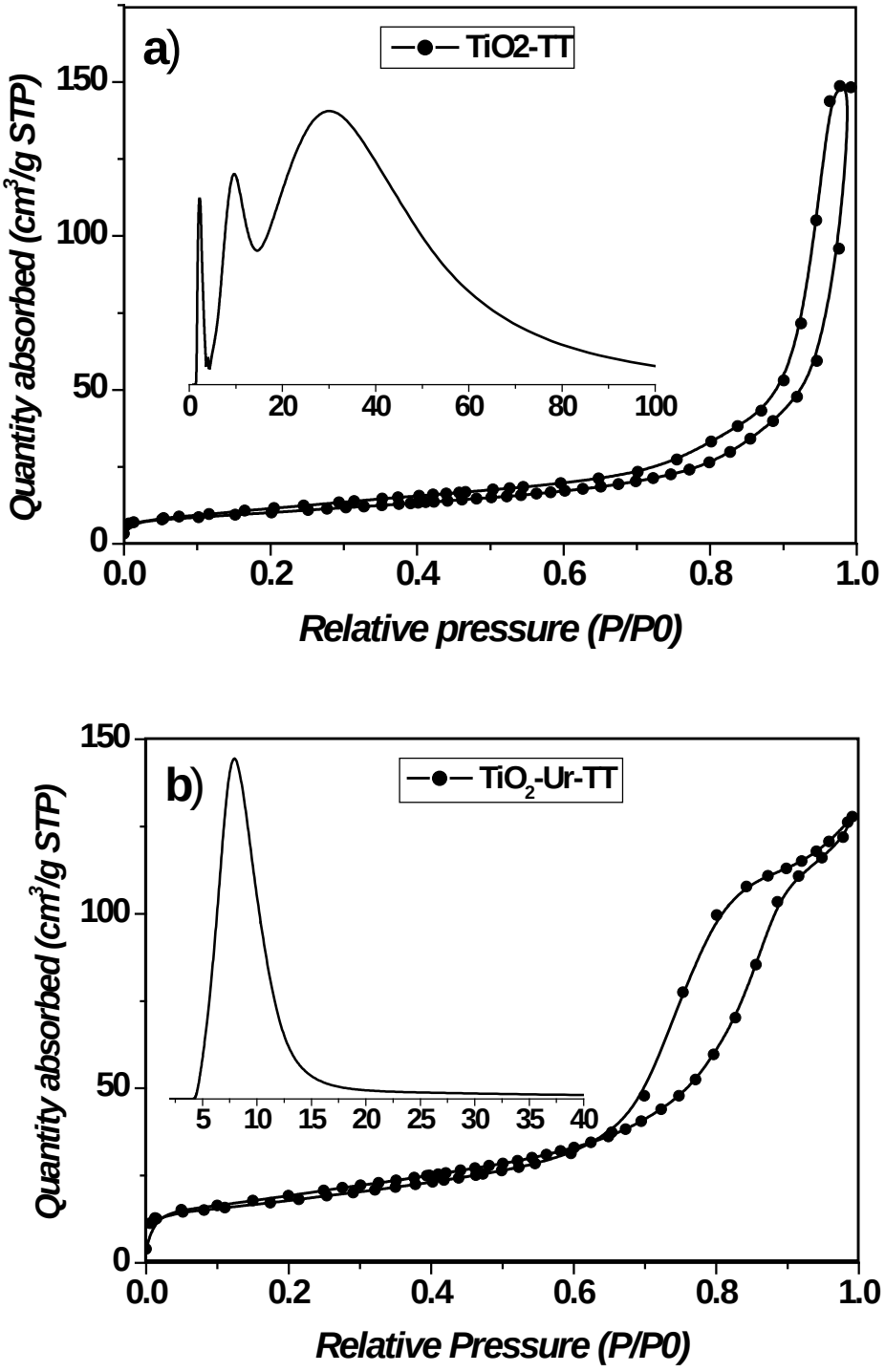

Figure 4.9 Nitrogen adsorption-desorption isotherms and corresponding BJH pore size distribution curves (inset) of (a) TiO_2-TT and (b) TiO_2-Ur-TT.

Table 4.6 Textural and structural parameters of TiO_2-TT and TiO_2-Ur-TT

Photocatalysts ID	S_{BET} [a] (m^2/g)	D_{BJH} [b] (nm)	V_t [c] (cm^3/g)
TiO_2-TT	36.31	2.2, 9.6, 31.5	0.2280
TiO_2-Ur-TT	69.34	7.9	0.1965

[a]BET surface area; [b]pore size distributions determined by the Barrett-Joyner-Halenda (BJH) method; [c]Total pore volume.

4.3.2 The effect of $TiCl_4$

The role of $TiCl_4$ is also examined in this work. In the acid-base pair method to synthesize mesoporous TiO_2, $TiCl_4$ is considered as the "PH adjustor" (Tian et al., 2004). The sample without $TiCl_4$ is fabricated and found to be pure anatase (Figure 4.10). Since the amount of $TiCl_4$ used in this work is 3g, a relative high value, it will result in a very low PH value, which may facilitate the formation of rutile and brookite phase (discussed later).

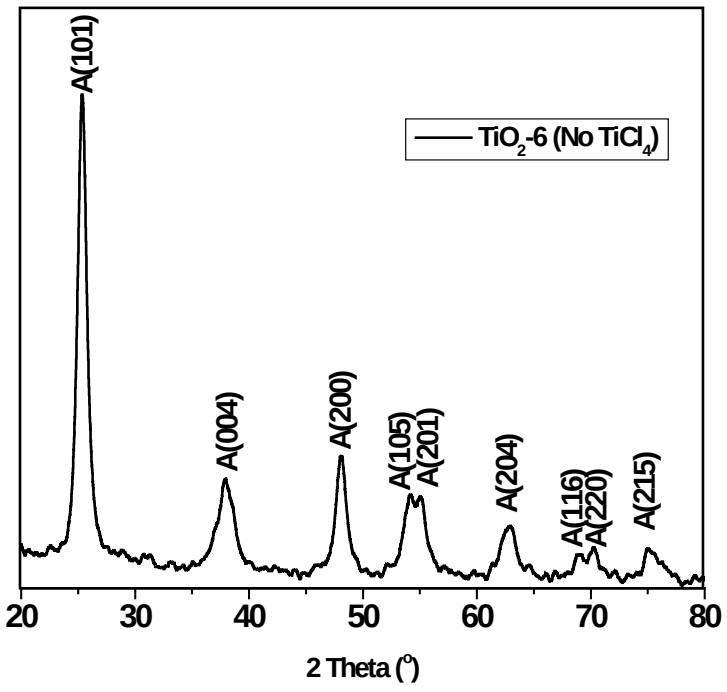

Figure 4.10 XRD pattern of TiO_2-6 (No $TiCl_4$).

The N_2 adsorption/desorption isotherm of TiO_2-6 in Figure 4.11 showed a type IV isotherm with H3 hysteresis loop, which was likely due to the slit-shaped pores resulting from aggregates of plate-like particles (Sing et al., 1985). But the mechanism of forming plate-like particles is not well understood. Its BET surface area and total pore volume are found to be 152.13 m^2/g and 0.5025 cm^3/g, respectively. Besides, it shows narrow pore size distribution with a peak centred on 7.8nm (Figure 4.11), which is much larger than that of mesoporous tri-crystalline TiO_2 samples fabricated with the existence of $TiCl_4$.

The pure anatase sample shows high photocatalytic activity and completes the photo-decloration of Orange II within 2.25h (the comparison with tri-crystalline samples will be discussed in the Section 4.4).

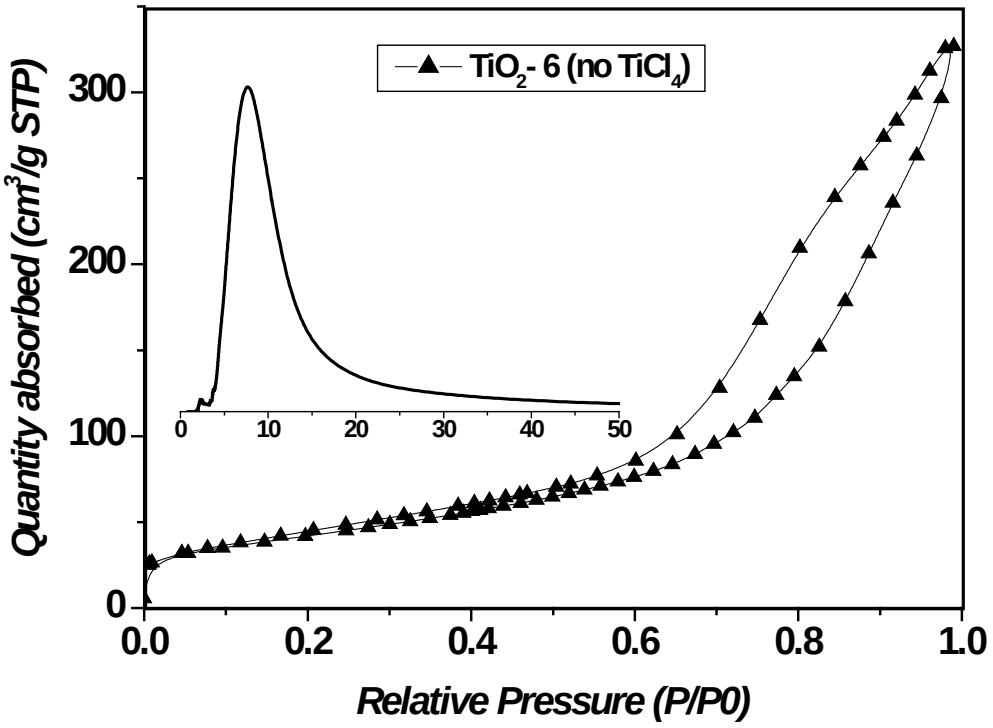

Figure 4.11 Nitrogen adsorption-desorption isotherm and corresponding BJH pore size distribution curves (inset) of of TiO_2-6 (No $TiCl_4$).

4.3.3 The effect of calcination temperature

Calcination temperature is considered as a key parameter affecting the mesoporous structures and phase transition. Thus three calcination temperatures, 350^{o}C, 450 ^{o}C and 550 ^{o}C, are investigated for the sample TiO_2-2 in this work.

From Figure 4.12, the two samples calcined at 450 ^{o}C and 550 ^{o}C maintains type IV isotherms, but the hysteresis loop shifts to larger relative pressure (P/P_0, 0.7-1.0), indicating that the pore size increases, which can be confirmed by the peak position from the inset of each figure. That the intrapaticle pore size distribution shifts to higher value is mainly because the mesopores partly collapse upon the increasing of calcination temperature, which also results in sharp decrease of the BET surface area to a very low value, 72.48m^2/g and 37.39 m^2/g (Table 4.7).

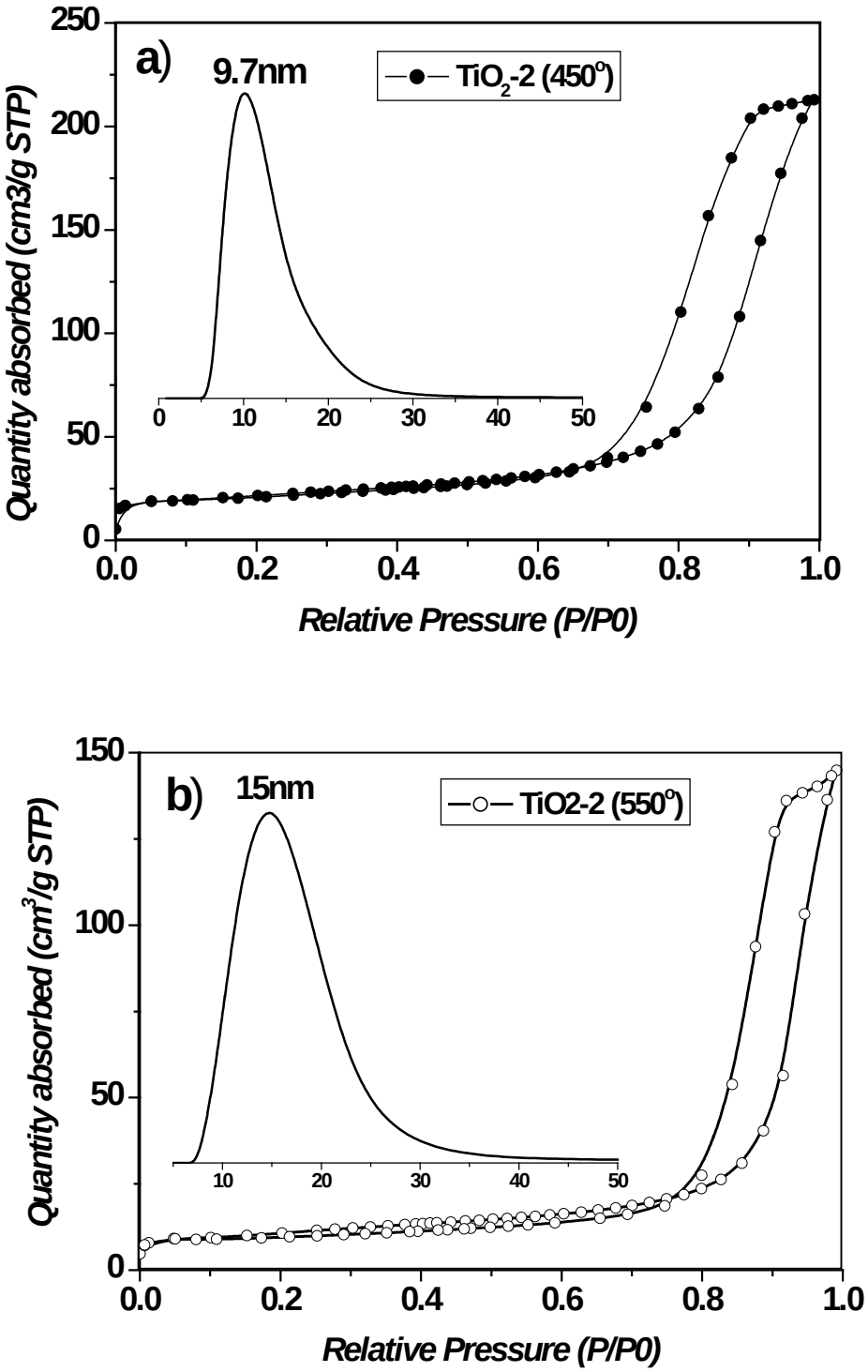

Figure 4.12 Nitrogen adsorption-desorption isotherms and corresponding BJH pore size distribution curves (inset) of (a) TiO_2-2 (450) and (b) TiO_2-2 (550).

Table 4.7 Textural and structural parameters of TiO_2-2 (450) and TiO_2-2 (550)

Photocatalysts ID	S_{BET} (m^2/g)	D_{BJH} (nm)	V_t (cm^3/g)
TiO_2-2 (350)	166.79	4.9	0.2697
TiO_2-2 (450)	72.48	9.7	0.3273
TiO_2-2 (550)	37.39	15.0	0.2226

[a]BET surface area; [b]pore size distributions determined by the Barrett-Joyner-Halenda (BJH) method; [c]Total pore volume.

Figure 4.13 shows the effect of calcination temperatures on the phase composition of tri-crystalline TiO_2. The sample calcined at 450 ^oC possesses very similar phase contents with that calcined at 350 ^oC, suggesting that the anatase phase is stable less than 450 ^oC. It is 550 ^oC that causes the significant transition from anatase phase to rutile phase while brookite phase still remains stable at this temperature (Table 4.8).

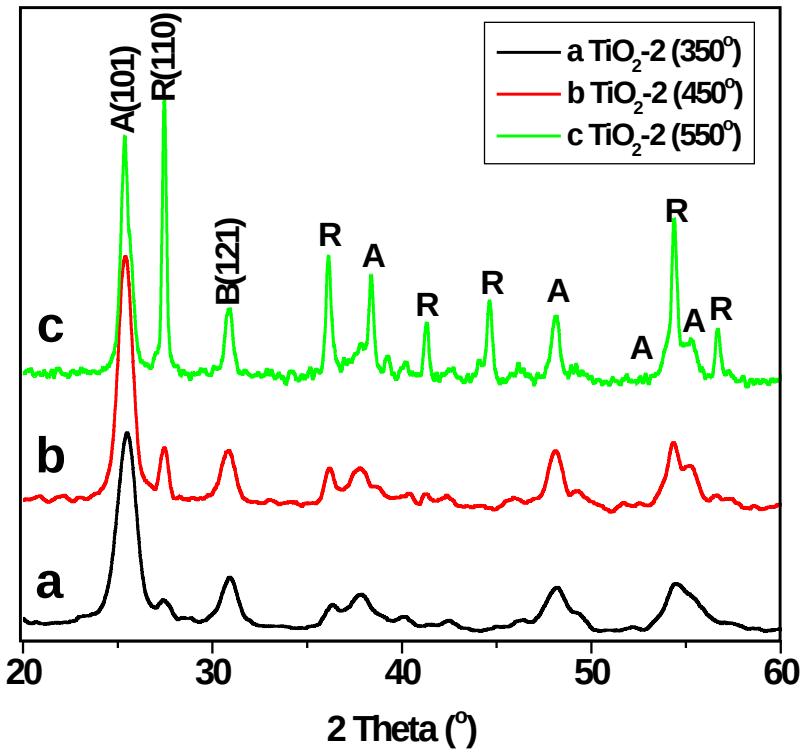

Figure 4.13 XRD patterns of TiO_2-2 (350), TiO_2-2 (450) and TiO_2-2 (550).

Table 4.8 Comparison of weight fraction in TiO_2-2 (350), TiO_2-2 (450) and TiO_2-2 (550)

Photocatalysts ID.	Anatase (%)	Rutile (%)	Brookite (%)
TiO_2-2 (350)	55.47	6.98	37.55
TiO_2-2 (450)	58.27	8.20	33.53
TiO_2-2 (550)	34.59	32.92	32.49

Even treated at very high temperature, the N species cannot be completely eliminated from the porous network, evidenced from XPS data (not shown). The surface N contents of these two samples were found to be 0.51% and 0.47%, respectively. Besides, the nature of N species left in the TiO_2 photocatalysts do not change, indicating that the NH_x located in an interstitial site strongly bound to titania and cannot be fully destructed less than 550^{o}C.

Figure 4.14 shows the photocatalytic performance of samples TiO_2-2 calcined at 350, 450 and 550^{o}C. As expected, the calcination temperature strongly affects the photocatalytic activity of the TiO_2 towards oxidizing and destructing Orange II. It can be clearly seen that the photocatalytic performance decrease sharply with the increase of calcination temperature. TiO_2-2 (450) exhibited poorer photocatalytic activity mainly due to the smaller BET surface area since the crystalline phase structure does not change much. While for the worst photoactivity of TiO_2-2 (550), it is caused by a combination effect of low BET surface area and the phase transition from anatase (more active phase) to rutile.

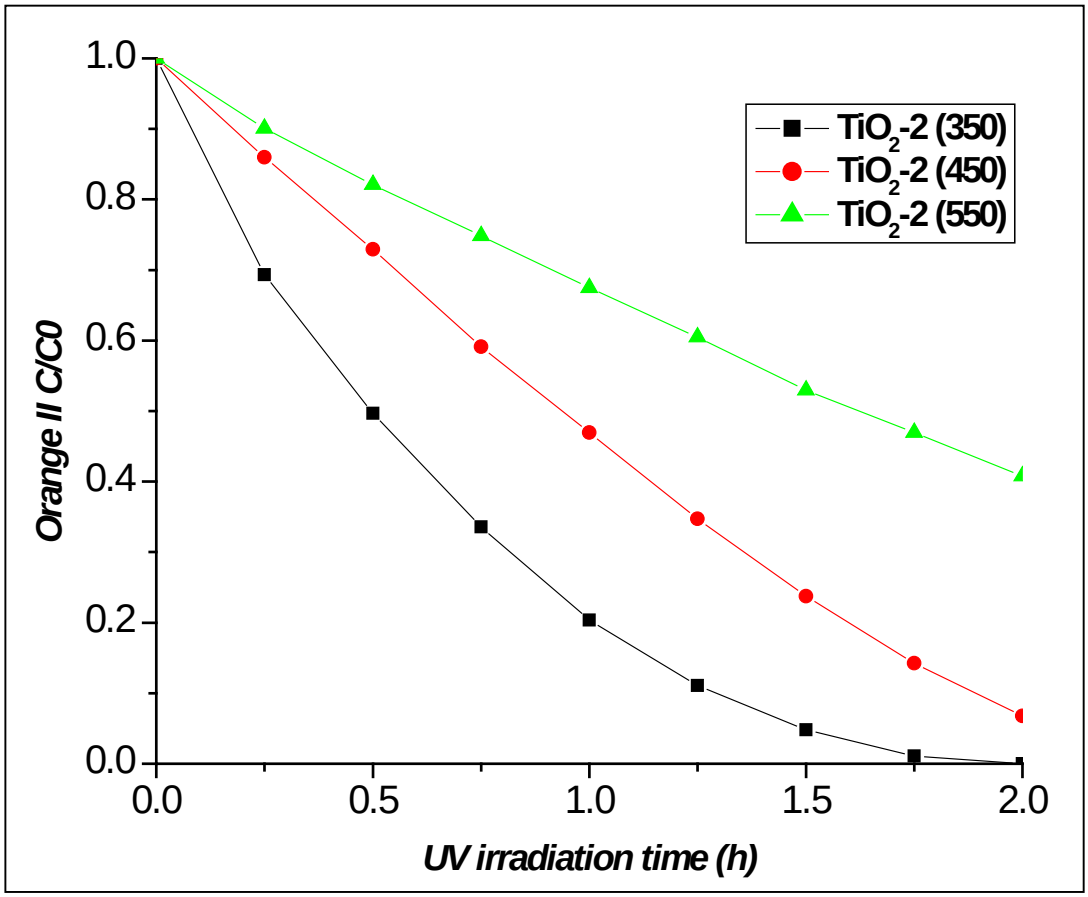

Figure 4.14 Comparison of the Orange II photodegradation activity over TiO_2-2 (350), TiO_2-2 (450) and TiO_2-2 (550). Experiment condition: semi-batch swirl flow reactor; light intensity: 110w/m^2; catalyst amount: 0.6 g/L; initial concentration of orange II: 20 mg/L.

4.4 Discussion of mesoporous tri-crystalline TiO_2 photocatalysts

4.4.1 Synthesis route and evolution of phase composition

The synthesis process in this work includes hydrolysis of *$TiCl_4$* in water, hydrolysis of *$Ti(oPr)_4$* (TTIP) in 2-propanol and water under strong acid condition, evaporation of solvent and gelation, hydrothermal treatment and final calcination.

Hydrolysis of 3g *$TiCl_4$* (Equation 4.4) in water generates large amount of *HCl*, which soon dissolves in water forming a strong acid environment. It is noted that

without *$TiCl_4$*, hydrolysis of *$Ti(oPr)_4$* leads to a basic gel (PH>10), facilitating the formation of pure anatase (TiO_2-6). Thus hydrolysis of *$Ti(oPr)_4$* can reduce the acidity and it also serves as an extra titanium source and oxygen donor. However, large amount of *HCl* and subsequent evaporation of solvent will result in a concentrated gel with high acidity ($[H^+]$ ~2mol/L).

$$TiCl_4 + 4H_2O(excess) \rightarrow Ti(OH)_4 + 4HCl \quad (4.4)$$

It is such strong acid condition that provides the possibility to form tri-crystalline or bi-crystalline TiO_2 since it is reported that the pure rutile and brookite phase can be obtained using 4M *HCl* at 200 ^oC and 3M *HCl* at 175 ^oC, respectively, by a two-step method (Coronado et al., 2008).

Addition of urea can reduce the acidity since it can react with water under the catalysis of *HCl* (Equation 4.5). Then the as-formed *NH_3* reacts with *HCl*, forming *NH_4Cl* (Eq. 4.6) and weakening the acidity. Urea serves as not only a PH adjustor, but also a stabilizer to enhance the porous network, especially increasing the BET surface area.

$$CO(NH_2)_2 + H_2O \xrightarrow{HCl} CO_2 + 2NH_3 \quad (4.5)$$

$$NH_3 + HCl \rightarrow NH_4Cl \quad (4.6)$$

As to TTEA, it can also react with *HCl* and reduce the acidity. However, the formation of pure rutile is probably due to the co-template of TTEA and dodecylamine rather than the weakening of the acidity.

4.4.2 The mechanism of photocatalytic degradation of Orange II

Orange II, with a molecular formula of $C_{16}H_{11}N_2NaO_4S$ (Figure 4.15), is widely used in the textile industry and it is a non-biodegradable synthetic dye. During the

photo-degradation of azo dyes over TiO_2 photocatalysts, it is widely accepted that the UV light irradiation results in the separation of photoinduced electrons and holes in the photocatalysts. These charge carriers can be transferred to the surface and combined with absorbed H_2O and O_2 molecules, generating highly reactive radicals, such as $OH^{\bullet}$, $O_2^{\bullet}$ and so on, as illustrated in Chapter 1. It is proposed that the highly reactive radicals firstly destroy the N=N bond (Figure 4.15) at the surface of TiO_2, generating benzene and naphthalene rings and subsequently forming a series of intermediates, like phenol, oxalate, malonate and so on (Bhattacharyya et al., 2004). Such intermediates tend to absorb on the surface of photocatalysts, leading to a decrease of photocatalytic activity.

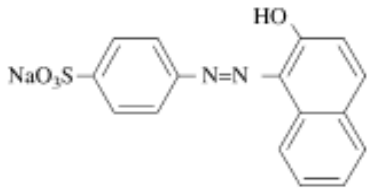

Figure 4.15 Chemical structure of Orange II (Bhattacharyya et al., 2004).

From Figure 4.6 and 4.7 in previous part, the tri-crystalline sample TiO_2-2 completed the photo-degradation, or more accurately photo-decoloration (not complete mineralization of Orange II), within 1.75h UV light irradiation. However, only decoloration is not really what we need since these organic intermediates still left in water may be harmful to human beings. But we cannot get useful information about the effect of TiO_2 on these organic intermediates from the UV-Visible spectrophotometer. Thus the value of total organic carbon (TOC) is evaluated in order to confirm the complete mineralization of Orange II and the results are compared with photo-decoloration data and shown in Figure 4.16.

As can be clearly seen from Figure 4.16, the TOC value decreases sharply at initial and then slows down due to the formation of reaction intermediates, which adsorb strongly on the surface of photocatalysts. TiO_2-2 only mineralizes about 64.1% of Orange II at 2h although the concentration of Orange II decreases to zero, evidenced from the value of its characteristic peak centred on 484.nm (Figure 4.6). After subsequent 40min UV light irradiation, the TOC value reduces to 13.56%, strongly indicating the complete mineralization of Orange II and its intermediates by tri-crystalline TiO_2 photocatalysts.

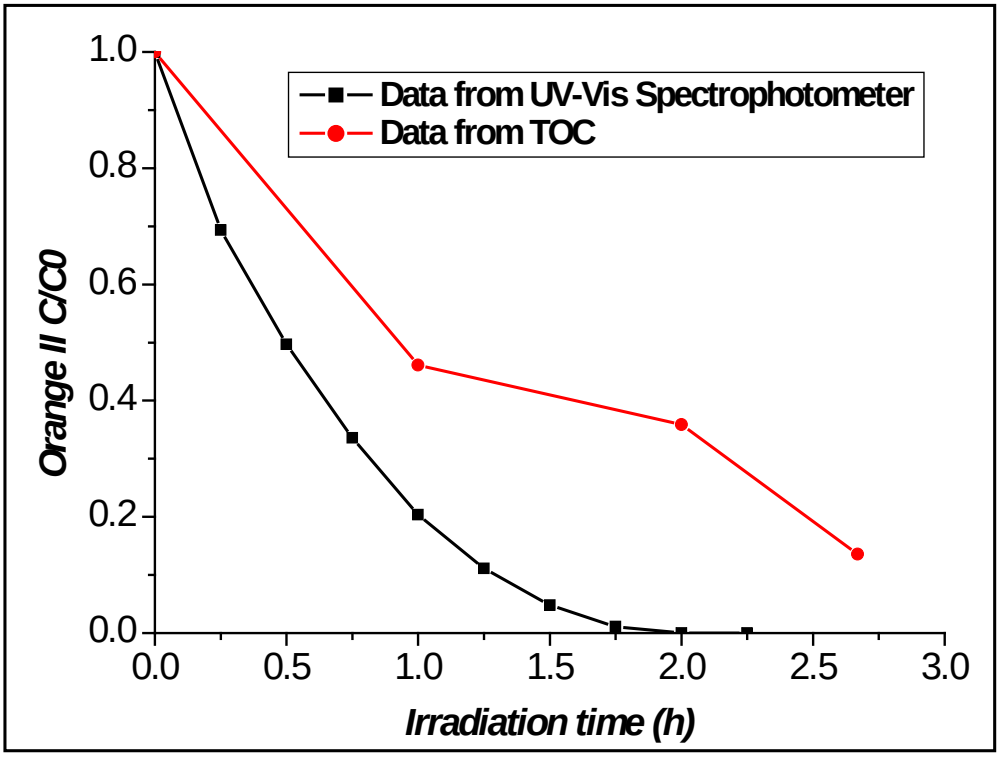

Figure 4.16 Comparison of photocatalytic degradation and TOC degradation of orange II over TiO_2-2. Experiment condition: semi-batch swirl flow reactor; light intensity: 110w/m^2; catalyst amount: 0.6 g/L; initial concentration of orange II: 20 mg/L.

4.4.3 The relationship between the phase content and photocatalytic activity

As mentioned in Chapter 1, the relationship between concentration ratio (C/C_0) of azo dyes and light irradiation time *t* follows the equation below

$$\ln(\frac{C}{C_0}) = kKt = K_{app}t \tag{4.7}$$

The kinetic parameter K_{app} is always selected to evaluate the photocatalytic performance of semiconductor photocatalysts. Thus the K_{app} of all the samples (excluding the samples calcined at 450^{o}C and 550^{o}C) are calculated by the Equation 4.7 (see the inset of Figure 4.17). From Figure 4.17, it can be clearly seen that pure anatase shows much better photoactivity than pure rutile due to its higher oxidation ability and obviously larger BET surface area. For mesoporous tri-crystalline TiO_2 photocatalysts, the sample TiO_2-2 with 55.47% anatase, 6.98% rutile and 37.55% brookite possesses the largest kinetic constant and it also shows better photocatalytic activity than pure anatase, pure rutile and bi-crystalline anatase-brookite samples.

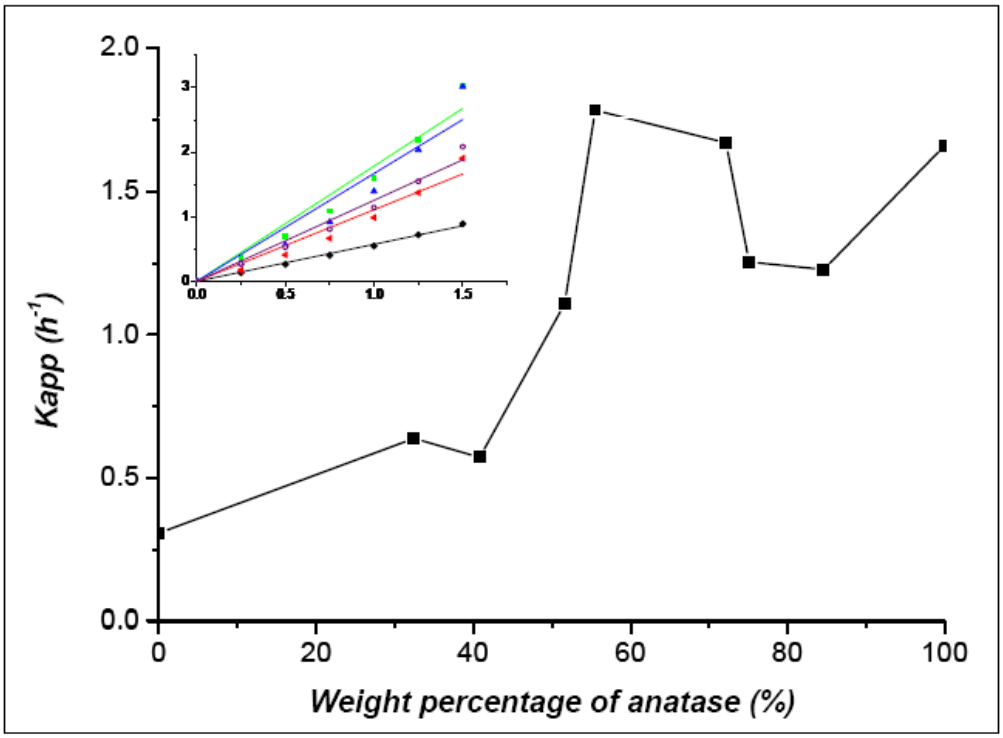

Figure 4.17 Variation in K_{app} as a function of anatase weight percentage and (inset) variation in the residual Orange II concentration as a function of UV-radiation exposure time for several samples.

Now the question is why the sample TiO_2-2 shows the best photocatalytic activity. Considering the N dopants existing in the porous networks, it may affect the photocatalytic performance by narrowing the band gap. Thus the UV-Vis absorption spectra of the samples TiO_2-s are measured and plotted in Figure 4.18. It is interestingly found that, with increasing the additive urea and thus the anatase phase percentage, the thresholds of absorption band of the resulted samples shows a slight blue shift (see the inset of Figure 4.18), which strongly suggests that it is the different phase contents rather than N dopants that cause these differences in the thresholds of absorbance bands since the band gap energies of rutile (3.0eV) and brookite (3.13eV) are a little smaller than that of anatase phase (3.2eV). Therefore, the sample TiO_2-0

with a large percentage of brookite phase possesses the narrowest band gap among all the samples.

Combining the facts that all the samples have nearly the same surface N content and that the light source employed in this work is UV light centred on 365nm, it is concluded that the N dopant is not the key parameter responsible for the variation in the photocatalytic performance for the samples. Besides, the BET surface area did not change much among the samples TiO_2-s (s=1-5) and pure anatase. Therefore it is the phase composition plays a key role in this work. The optimal phase composition in the sample TiO_2-2 facilitates the separation of photoinduced charge carriers and reduces the recombination rate of charge carriers due to the "phase junction effect".

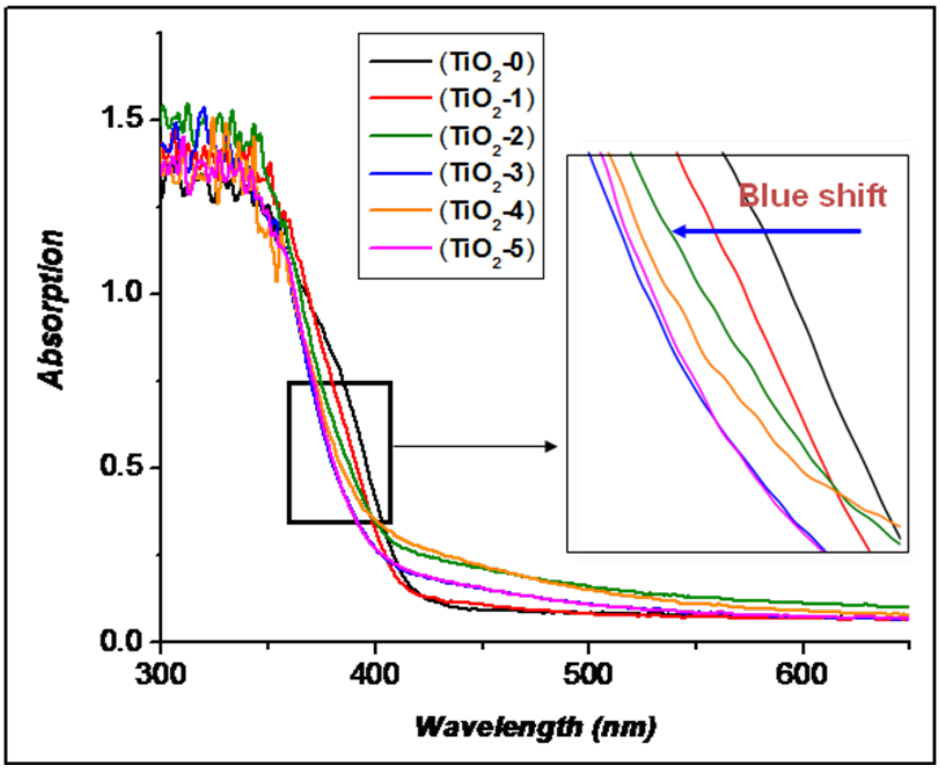

Figure 4.18 DR absorbance spectra obtained for the samples TiO_2-s (s=0-5) and (inset) enlarged view of highlighted rectangle.

4.5 Summary

In this chapter, a simple hydrothermal method is successfully developed to synthesis tri-crystalline TiO_2 photocatalysts. By changing the types and amounts of N-contained additives, the phase composition can be tuned. After analyzing all the data of these TiO_2 photocatalysts, several conclusions can be drawn as following:

(1) Strong acid environment is the key factor for the synthesis of tri-crystalline or bi-crystalline TiO_2 photocatalysts;

(2) Urea has an effect on improving the mesoporous framework, increasing the specific surface area and raising the anatase content via changing the PH value;

(3) Pure rutile TiO_2 can be successfully fabricated by employing TTEA as the additive while pure anatase TiO_2 can be formed without one of the Ti precursors, $TiCl_4$;

(4) The mesoporous tri-crystalline sample TiO_2-2 exhibits the best photocatalytic performance for degradation of Orange II under UV light and it is likely due to the large surface area and the optimal phase composition. The generated phase junction among the different polymorphs thus facilitates the separation of photoinduced electron and hole and suppresses the recombination rate.

CHAPTER 5

ONE-POT FABRICATION AND CHARACTERIZATION OF TiO_2 –Au NANOTUBES WITH VISIBLE-LIGHT-RESPONSE

5.1 Introduction

Recently, extensive interests have focused on the preparation and applications of one dimensional (1D) TiO_2 materials, especially TiO_2 nanotubes (NTs) due to their many advantages, such as large internal and external surface areas, pore accessibility, highly crystallinality, as well as abundance of surface OH groups (Bavykin et al., 2006; Bavykin and Walsh, 2009). Generally, 1D TiO_2 NTs can be prepared by three routes, including chemical templating synthesis (Liu et al., 2002), anodization of Ti foils in fluoride-containing solution (Gong et al., 2001), and hydrothermal method under strong basic environment (Kasuga et al., 1998; Kasuga et al., 1999), among which the alkaline hydrothermal method has attracted much attention since it is a simple, cost-effective and environmentally friendly technology. Moreover, the excellent ion-exchange capacity of the intermediates, $Na_2Ti_3O_7$ NTs and $H_2Ti_3O_7$ NTs, provides the possibility of loading metal ions/nanoparticles for catalytic applications through ion-exchange process (Sun and Li, 2003).

However, one of the shortcomings of pure TiO_2 materials, including naked TiO_2 NTs, lies in its large band gap energy, requiring UV energy to activate it and thus resulting in a low energy efficiency and high cost. Besides, the thermal stability of TiO_2 NTs prepared by alkaline hydrothermal method is really poor (lower than

300^oC). Therefore, many efforts have been made to extend the light responds of TiO_2 NTs from UV region to visible region and/or improve its thermal stability.

Jiang et al. (2008) solvothermally treated $H_2Ti_3O_7$ NTs in an ethanol-water solution with NH_4Cl at 120^oC. The resultant N-doped anatase TiO_2 nanotubes exhibited visible-light photocatalytic activity and the thermal stability was significantly improved up to 600^oC.

Loading noble metal nanoparticles (NPs) or coupling other semiconductor NPs onto TiO_2 NTs has been viewed as an alternative strategy to improve its photocatalytic activity and thermal stability. Toledo-Antonio et al. (2009) prepared Ag-loaded TiO_2 NTs via ion-echange between $H_2Ti_3O_7$ NTs and $AgNO_3$ solution, following with thermal reduction of Ag^+ ions to Ag nanoparticles. Zhao et al. (2009) prepared Au- or Pt-loaded TiO_2 NTs by treating the annealed $H_2Ti_3O_7$ NTs with Au or Pt precursors, followed with UV-assisted photoreduction. The resulted samples showed enhanced photocatalytic performance towards oxidation of azo dyes.

Grandcolas et al. (2009) prepared WO_3 nanoparticles decorated TiO_2 NTs by impregnating $H_2Ti_3O_7$ NTs with tungsten-containing ethanol/water solution. The synthesized WO_3-TiO_2 composite NTs were found to show better photocatalytic activity than pure TiO_2 NTs did towards destruction of gaseous chemical warfare agents under solar light irradiation. An et al. (2010) successfully fabricated iron-coated TiO_2 (Fe_2O_3-TiO_2) NTs by injecting $Fe(OH)_3$ sol strategically into the interlayer spacing of $H_2Ti_3O_7$ NTs. Subsequent thermal treatment converted the $Fe(OH)_3$ sol to uniformly dispersed Fe_2O_3 NPs, which served as a solid support for TiO_2 nanotubes and thus responsible for its enhanced thermal stability up to 400^oC. At this temperature, Fe_2O_3-TiO_2 NTs exhibited the best photocatalytic performance towards destructing methyl orange dye.

However, all the design strategies mentioned above based on a two-step synthesis route to achieve modification of pure TiO_2 nanotubes. In other words, interests were focused on modifying as-prepared or annealed $H_2Ti_3O_7$ NTs with metallic or non-metallic precursors after the hydrothermal synthesis. To date, limited methods have been reported for one-pot preparation of TiO_2 NTs with visible-light-response and/or improved thermal stability (Peng et al., 2008).

Actually, in hydrothermal conditions, supercritical water (SC) can serve as the reducing agent and offers a facile and green chemistry alternative to chemical reduction or photo-assisted reduction. Recently, Zhou et al. (2009) utilized the reducing capability of SC to convert graphene oxide to graphene and the results were really attractive. Furthermore, Peng et al. (2008) fabricated graphene-TiO_2 NT by simultaneously reducing graphene oxide with SC and forming TiO_2 NTs through one-pot hydrothermal synthesis without adding any reducing agents.

Therefore, in the present work, similar strategy was carried out in order to fabricate Au-loaded TiO_2 NTs by adding the Au precursor directly into the strong basic P25-containing mother solution before hydrothermal synthesis. The photocatalytic activity and antibacterial property of the prepared Au-loaded TiO_2 NTs were evaluated by photo-degradation of azo dyes and photo-killing of *E. Coli* under visible light irradiation. In addition to the catalytic activity, the possible cyclic usage of photocatalyst is another important issue for heterogeneous photocatalytic reactions. However, very few studies have focused on this issue. Thus, in the present work, the photocatalyst recycle and reuse were also evaluated.

5.2 Characterization and photocatalytic activity of TiO_2-Au nanotubes

5.2.1 Morphology of samples

Figure 5.1 illustrates TEM images of one typical Au-loaded TiO_2 nanotubular photocatalyst, TiO_2-Au-0.5%. As shown in Figure 5.1, the sample has an obvious tubular structure, which is not damaged during the calcination treatment. They are open-end nanotubes with 50-100nm in length and ~11 nm in outer diameter. Besides, small Au nanoparticles highlighted by the arrows are successfully deposited onto the outer and inner wall surface of TiO_2 NTs.

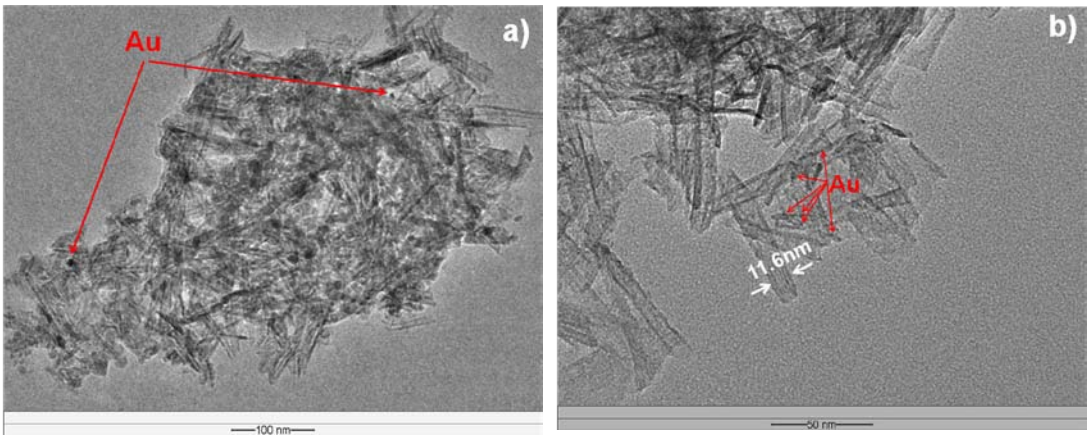

Figure 5.1 TEM images of TiO_2-Au-0.5% nanotubular photocatalyst.

5.2.2 N_2 adsorption/desorption analysis

N_2 adsorption/desorption isotherms and the corresponding BJH-PSD curves for $H_2Ti_3O_7$ NTs, $H_2Ti_3O_7$-Au-0.5% NTs and TiO_2-Au-*x*% NTs calcined at 350^{o}C are shown in Figure 5.2. According to the IUPAC classification, the entire samples show typical type IV curves, which strongly suggest the formation of mesopores in the nanotubular photocatalysts (Sing et al. 1985). The type of hysteresis loop of N_2

isotherms is intermediate between H1 (at $0.5< P/P_0< 0.8$), which is characteristic of uniform cylindrical pores inside aggregates of particles (Dong et al., 2007), and H3 (at $P/P_0> 0.8$). On one hand, a sharp capillary condensation step starting at relative pressure (P/P_0~0.7) is observed, suggesting a very narrow pore size distribution. On the other hand, the observed hysteresis loop extends to $P/P_0\approx1$, strongly indicating the presence of macropores, which are not being filled. The corresponding BJH-PSD curves offer clear and solid evidence for the analysis of pore structures above (see the insets of Figure 5.2a-h). Taking into account the TEM observations of the resulted nanotubular photocatalysts, the smaller pores (9-13nm) may correspond to the pores inside the nanotubes while the macropores (~120nm) may be formed due to the complicated overlaps of nanotubes (Figure 5.1a).

Textural and structural parameters obtained from the N_2 adsorption/desorption data are summarized in Table 5.1. The specific surface area (SSA) of the hydrogen titanate NTs is as high as 348.52 m^2/g while the SSA of the $H_2Ti_3O_7$-Au-0.5% NTs is reduced to 292.26 m^2/g probably due to loading Au nanoparticles. After calcination, the resulted pure TiO_2 NTs lost more than half of its surface area owing to the poor thermal stability and partial damage of nanotubular structures. As to Au-loaded TiO_2 photocatalysts, their SSA and total pore volume are obviously larger than the naked TiO_2 NTs. Since the exfoliation of bulk TiO_2 powders, curving and scrolling of titanate sheets, and the reduction of gold ions occur spontaneously in one pot, some tiny gold nanoparticles just formed may be scrolled into the interlayer spacing of titanate NTs, which thus serve as a solid support for nanotubular structures during calcination process, leading to an improved mesoporous structures and higher surface area.

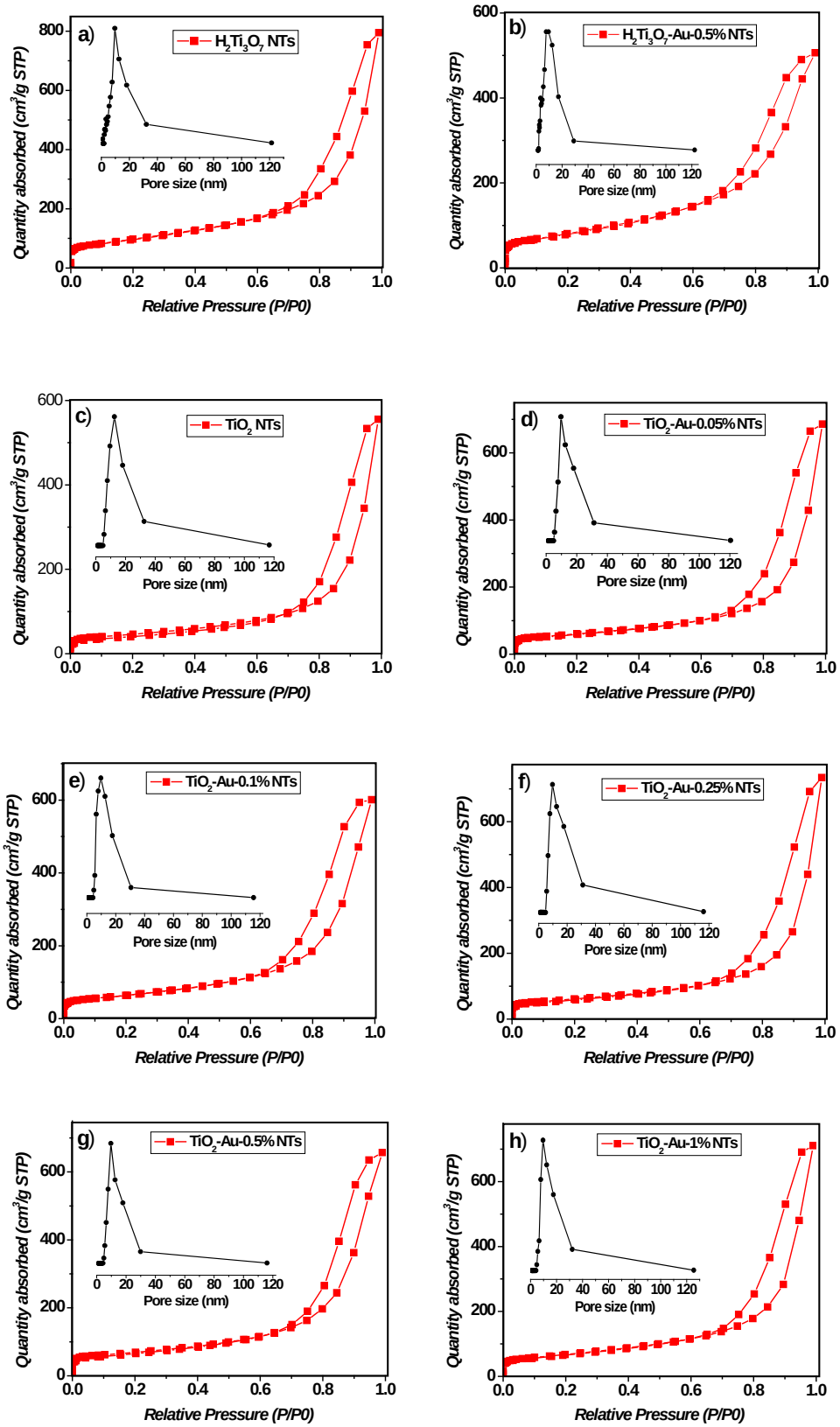

Figure 5.2 Nitrogen adsorption-desorption isotherms and corresponding BJH pore size distribution curves (inset) of (a) $H_2Ti_3O_7$ NTs, (b) $H_2Ti_3O_7$-Au-0.5% NTs and (c-h) TiO_2-Au-*x*% NTs (x=0, 0.05, 0.1, 0.25, 0.5 and 1).

Table 5.1 Textural and structural parameters of $H_2Ti_3O_7$ NTs, $H_2Ti_3O_7$-Au-0.5% NTs and TiO_2-Au-*x*% NTs

Samples ID.	S_{BET} [a] (m^2/g)	D_{BJH} [b] (nm)	V_t [c] (cm^3/g)
$H_2Ti_3O_7$ NTs	348.52	2-120, 9.6	1.2220
$H_2Ti_3O_7$-Au-0.5% NTs	292.26	2-120, 7.7, 9.6	0.8063
TiO_2 NTs	161.37	5-120, 12.5	0.8537
TiO_2-Au-0.05% NTs	210.95	5-120, 9.8	0.9660
TiO_2-Au-0.1% NTs	226.00	5-120, 9.7	0.9240
TiO_2-Au-0.25% NTs	235.11	5-120, 9.7	1.0290
TiO_2-Au-0.5% NTs	238.90	5-120, 9.9	0.9794
TiO_2-Au-1% NTs	240.17	5-120, 9.5	1.0922

[a]BET surface area; [b]pore size distributions determined by the Barrett-Joyner-Halenda (BJH) method; [c]Total pore volume.

5.2.3 X-ray Diffraction results

The XRD patterns of the resulted TiO_2-Au-*x*% NTs photocatalysts as well as the sample $H_2Ti_3O_7$-Au-0.5% NTs before calcination are shown in Figure 5.3. It can be clearly seen from Figure 5.3a that the two main peaks at 24.3 and 48.3^o highlighted by the arrows could be assigned to (110) and (200) diffraction planes of the lepidocrocite-type titanate $H_2Ti_3O_7$ NTs (Bavykin et al., 2006). In addition, characteristic diffraction peaks at 44.5^o is also observed in the sample before calcination, which is attributed to the (200) faces of metallic gold nanoparticles (Wu et al., 2009), strongly suggesting that the gold ions are reduced to metallic state during the hydrothermal synthesis. The peaks at 2θ values of 25.3, 37.8, 48.0, 53.9, 55.1 and 62.7 can be indexed to (101), (004), (200), (105), (211) and (204) crystal planes of anatase TiO_2 (JCPDS no. 21-1272), respectively (Figure 5.3b-g). With increasing the

molar ratio of Au/Ti in the initial solution, the (200) peak of gold NPs becomes more obvious (see Figure 5.3c-g).

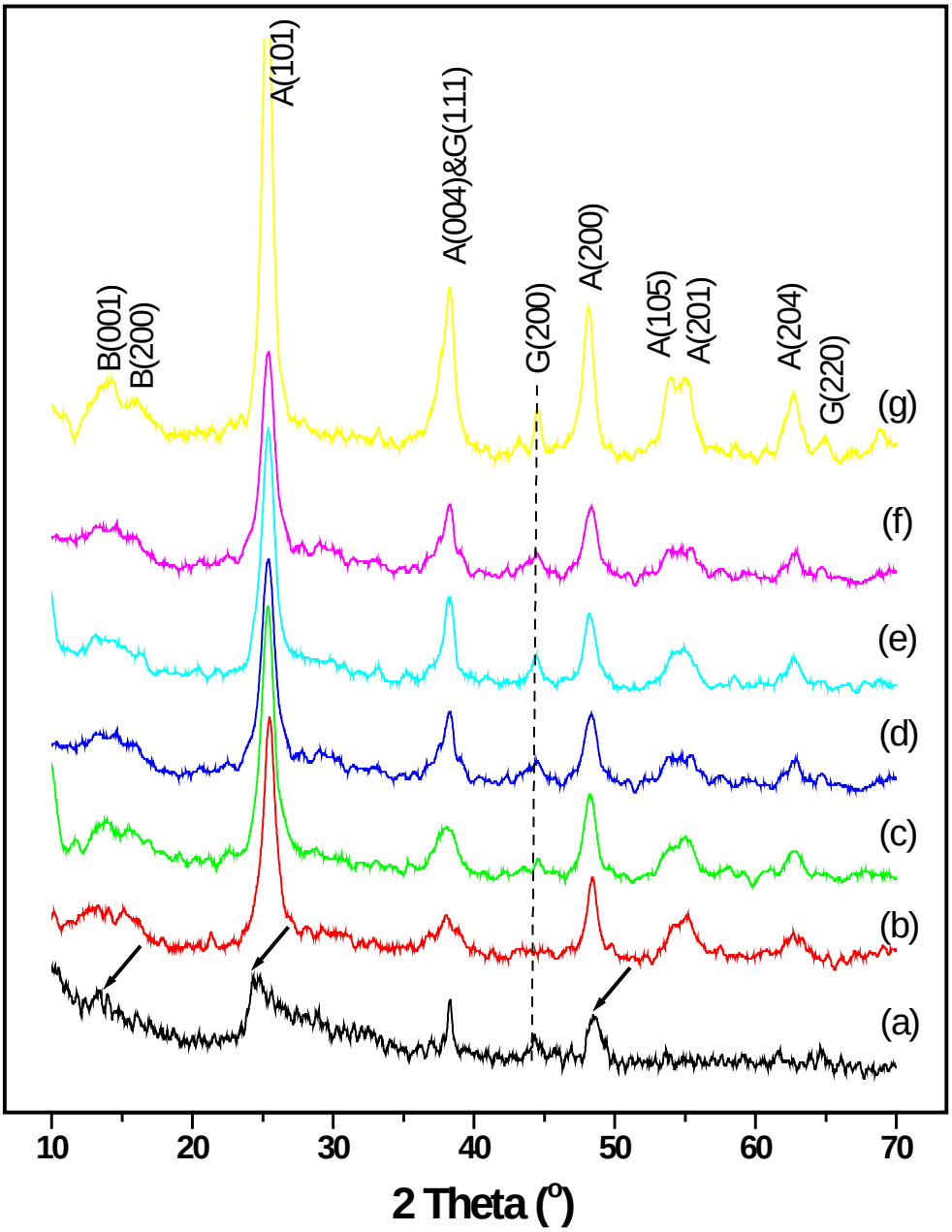

Figure 5.3 XRD patterns of (a) $H_2Ti_3O_7$- Au-0.5% NTs, (b) pure TiO_2 NTs, (c) TiO_2-Au-0.05% NTs, (d) TiO_2-Au-0.1% NTs, (e) TiO_2-Au-0.25% NTs, (f) TiO_2-Au-0.5% NTs, (g) TiO_2-Au-1% NTs.

More interestingly, minor peaks located at 12.7, 13.9 and 33.4^o, which can indexed to (001), (200) and (311) faces of TiO_2 (B) (JCPDF 35-0088), are also clearly observed, indicating that a low content of impurity TiO_2(B) exists in the resulted TiO_2-Au composite photocatalysts, which was probably due to the calcination treatment at above 250^{o}C (Armstrong et al., 2004; Armstrong et al., 2005). According to Yang et al. (2009), phase composition, TiO_2(B)/anatase, is roughly calculated from the intensity ratio ($I_{33.4°}/I_{37.8°}$) of the peak at 33.4° to the peak at 37.8°, which correspond to the (311) plane of TiO_2(B) and the (004) plane of anatase, respectively. From Table 5.2, the contents of TiO_2(B) are not significantly changed by loading various amounts of gold nanoparticles on TiO_2 NTs and are restricted into a very low level (2.4-4.5%). Fortunately, the formed TiO_2(B) impurity is demonstrated to benefit the photocatalytic activity of anatase due to the phase junction effect (Yang et al., 2009).

Table 5.2 Phase compositions TiO_2(B)/anatase of TiO_2-Au-*x*% NTs

Au/Ti, x%	0	0.05%	0.1%	0.25%	0.5%	1%
TiO_2(B)/Anatase	3.7/96.3	2.4/97.6	2.9/97.1	4.0/96.0	4.5/95.5	4.3/95.7

5.2.4 XPS results

Surface information on the Au-loaded TiO_2 nanotubes is investigated by XPS technique. The broad-scan XPS spectrum of TiO_2-Au-1% nanotubular photocatalyst is displayed in Figure 5.4a. A very tiny peak located at around 83 eV is observed, indicating the existence of gold species. It can be clearly seen from Figure 5.4b that binding energy values for Au $4f_{7/2}$ and Au $4f_{5/2}$ are found to be 83.1 and 86.8 eV, respectively, suggesting that all the Au species existed in their metallic state. No oxidized gold species was detected. According to the XPS handbooks, binding energy

values of Au $4f_{7/2}$ and Au $4f_{5/2}$ for metallic Au were centered at 84.0 and 87.7 eV, respectively. In the present work, the 0.9 eV shift of Au 4f peaks toward lower binding energies indicates strong interaction between the guest Au nanoparticles and the host TiO_2 NTs support (Wu et al., 2009).

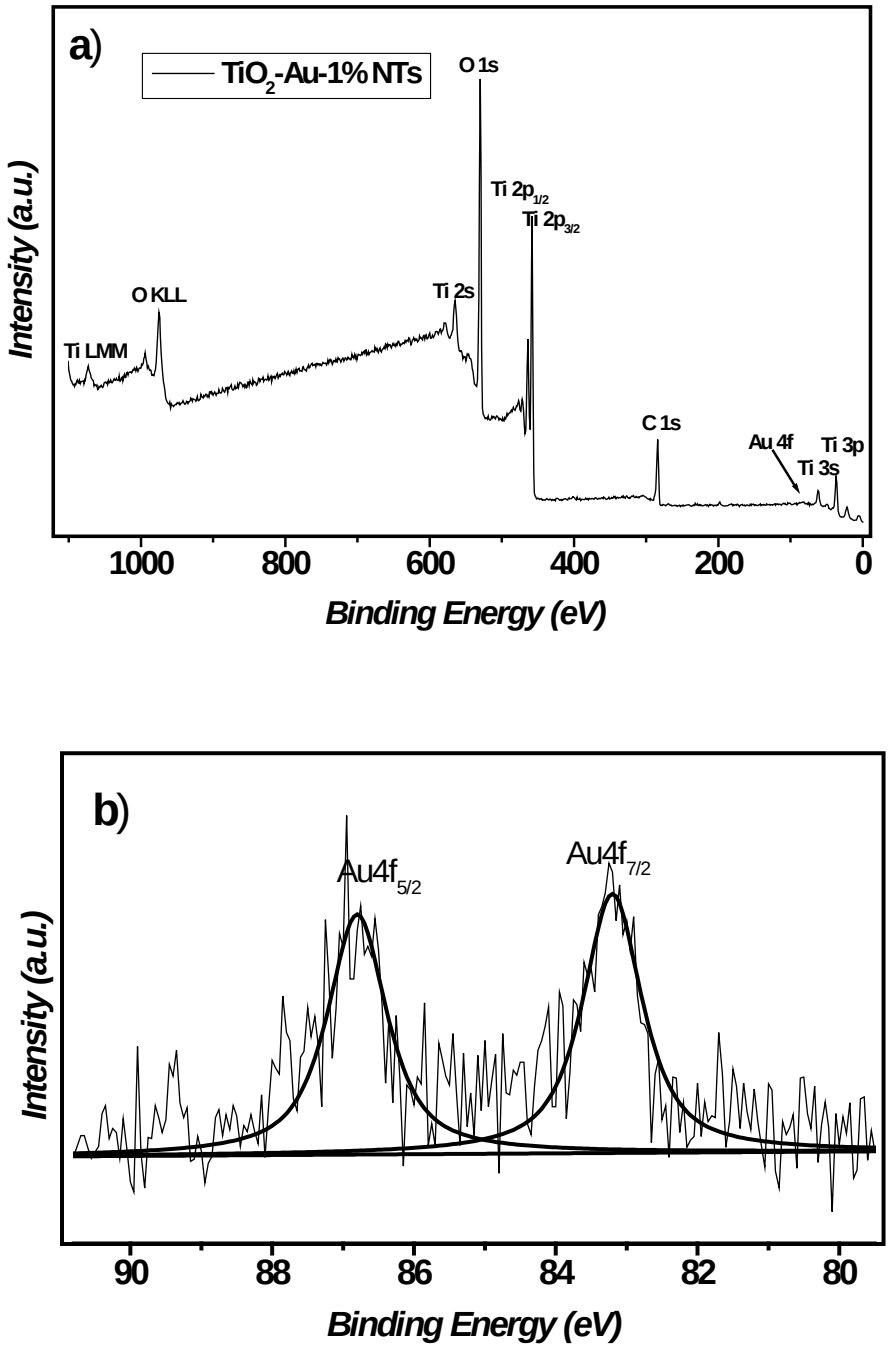

Figure 5.4 (a) Broad-scan XPS spectra and (b) high-resolution XPS spectra of Au 4f for the resulted TiO_2-Au-1% nanotubular photocatalyst.

5.2.5 Optical property

To study the optical response of TiO_2-Au-*x*% NTs, we measure the UV-Vis absorption spectra of TiO_2-Au-*x*% NTs (x=0, 0.05, 0.1, 0.25 and 0.5), $H_2Ti_3O_7$ NTs, and $H_2Ti_3O_7$-Au-0.05% NTs, and results are shown in Figure 5.5. In contrast to pure $H_2Ti_3O_7$ NTs, the absorption threshold of naked TiO_2 NTs after calcination shows an obvious red shift (Figure 5.5a) mainly due to the difference of band gap energy between the two materials (Bavykin et al., 2006; Bavykin and Walsh, 2009). It is worth noting that $H_2Ti_3O_7$-Au-0.05% NTs has an obvious broad absorption band ranging from 500 nm to 600 nm, which can be ascribed to the plasmon resonance of metallic Au nanoparticles according to the literatures (Zhao et al., 2009), thus indicating the effective reduction of Au^{3+} ions to Au nanoparticles during the hydrothermal synthesis. Besides, the intensity of the plamonic absorption band of TiO_2-Au-0.05% NTs is slightly improved compared with that of $H_2Ti_3O_7$-Au-0.05% NTs, probably due to Au nanoparticles depositing on two different supports.

From Figure 5.5b, the Au-loaded TiO_2 nanotubular photocatalysts exhibits significantly enhanced visible light absorption capability (400-700nm) and plamonic absorption band (centered on 540nm) with increasing the loading amount of Au nanoparticles. Besides, a slight red shift of the absorption thresholds of Au-loaded TiO_2 NTs is also observed, suggesting a slight effect of Au loading amount on the band gap narrowing of TiO_2 photocatalysts.

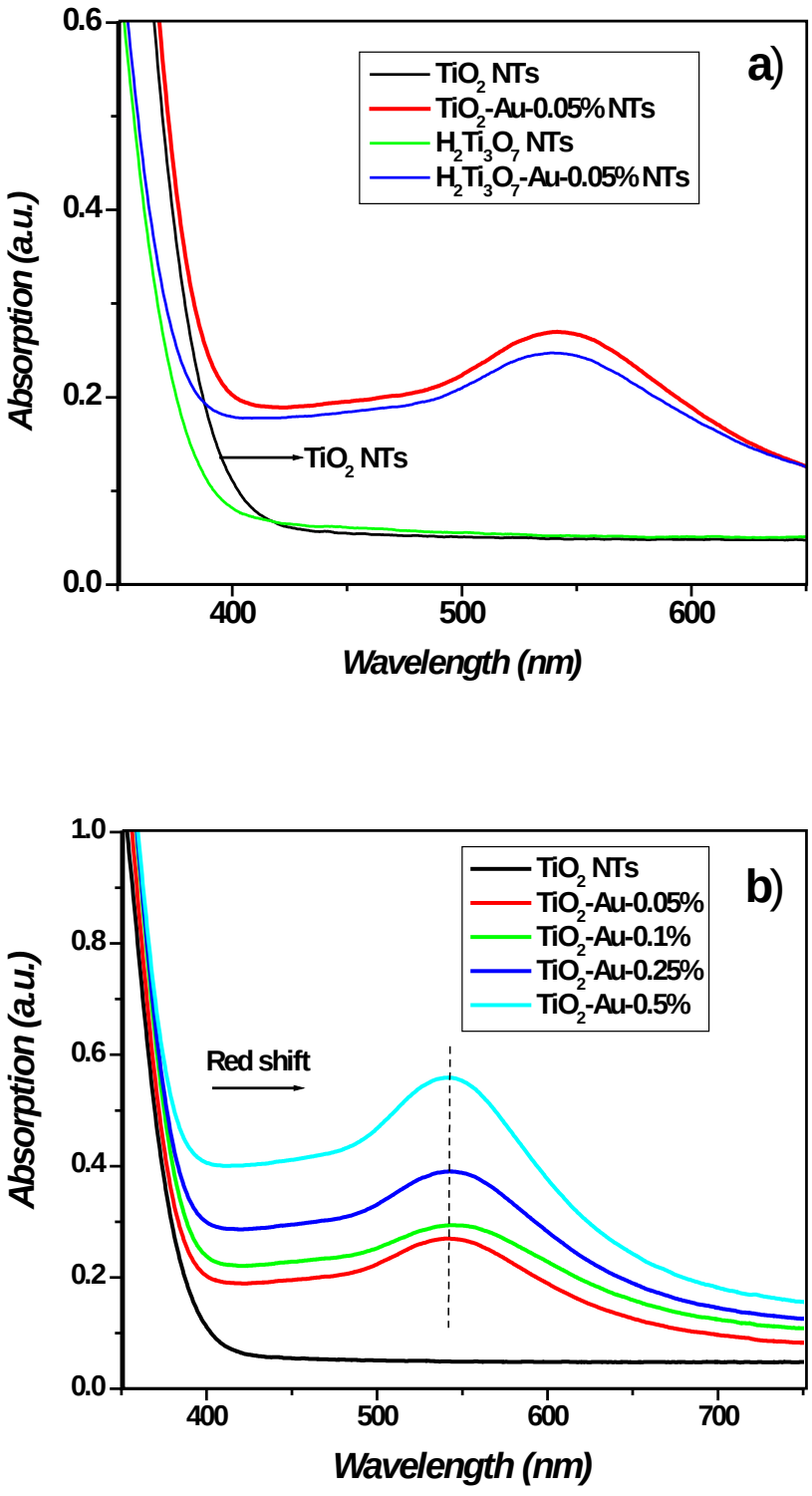

Figure 5.5 Comparison of DR absorbance spectra of (a) TiO_2 NTs, $H_2Ti_3O_7$ NTs TiO_2-Au-0.05% NTs, and $H_2Ti_3O_7$-Au-0.05% NTs, and (b) TiO_2-Au-*x*% NTs (x=0, 0.05, 0.1, 0.25 and 0.5).

5.2.6 Photocatalytic degradation of azo dyes under visible light irradiation

The photocatalytic activities of TiO_2-Au-*x*% NTs are evaluated by destructing Orange II dye under visible light (VL) illumination (Figure 5.6). It can be seen from Figure 5.6 that the degradation of Orange II hardly occurs only under VL irradiation. Note that the pure TiO_2 NTs without loading Au NPs can degrade 23% of Orange II after 3.5h VL irradiation, which is mainly due to self-sensitized degradation of dyes on TiO_2 surface (Chatterjee and Dasgupta, 2005). When the TiO_2 surface adsorbed Orange II dye molecules is exposed to the VL illumination, the adsorbed dye molecules are firstly got excited to its excited state, thus ejecting one electron from itself. The photo-induced electrons thus can be transferred to the conduction band of the TiO_2 semiconductor and then taken up by the O_2 molecule in the reacting solution, forming superoxide radicals, which will attack the dye molecules repeatedly to convert them to organic intermediates and then finally mineralize all the organic molecules to non-toxic harmless CO_2 and H_2O.

Au nanoparticles can also get excited under VL illumination due to the plasmon resonance effect (Figure 5.5). The ejecting electrons will be transferred to the conduction band of the TiO_2 semiconductor and then involved in the photocatalytic reaction system similar with the electrons generated by excited azo dyes, thus accelerating the degradation rate, which is evidenced from Figure 5.6. It can be clearly concluded that all the Au-loaded TiO_2 nanotubular photocatalysts exhibit enhanced visible light activity, especially the sample with 0.25% Au loading (molar ratio of Au/Ti).

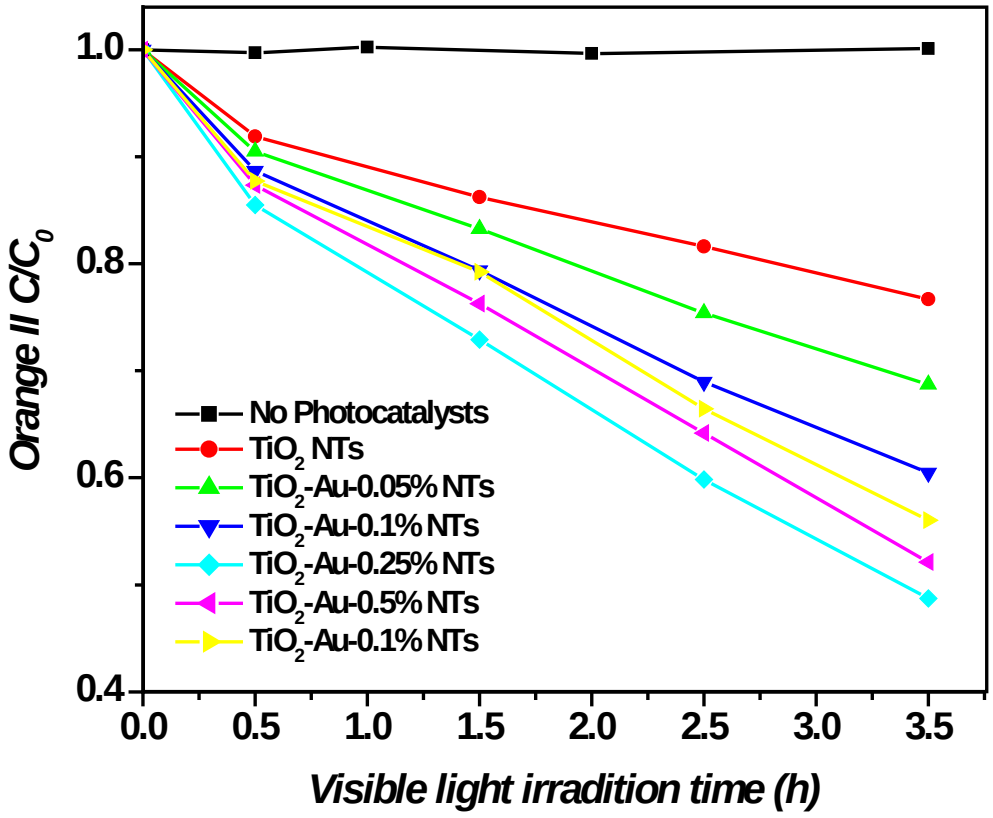

Figure 5.6 Comparison of the photocatalytic activity over TiO_2-Au-*x*% NTs towards oxidation of Orange II. Experiment condition: batch reactor; light source: 350W Xenon light equipped with a 420nm cut-off filter; catalyst amount: 1 g/L; initial concentration of Orange II: 5 ppm.

The kinetic data are fitted to the first-order kinetic equation, $\ln(C/C_0)=-k_{app}t$, where k_{app} is the apparent rate constant, C and C_0 are the concentrations of Orange II at time t=t and t=0, respectively (see the inset curves in Figure 5.7). Figure 5.7 shows the plot of apparent rate constants of the nanotubular photocatalysts versus their molar ratio of Au/Ti. With increasing the molar ratio of Au/Ti, the apparent rate constant (or VL activity) firstly increases and then decreases above the optimal Au loading amount. This is mainly because that higher Au loading may result in a high coverage of TiO_2 surface area, leaving a smaller surface exposed to targeted organic wastes, thus a decrease photocatalytic activity.

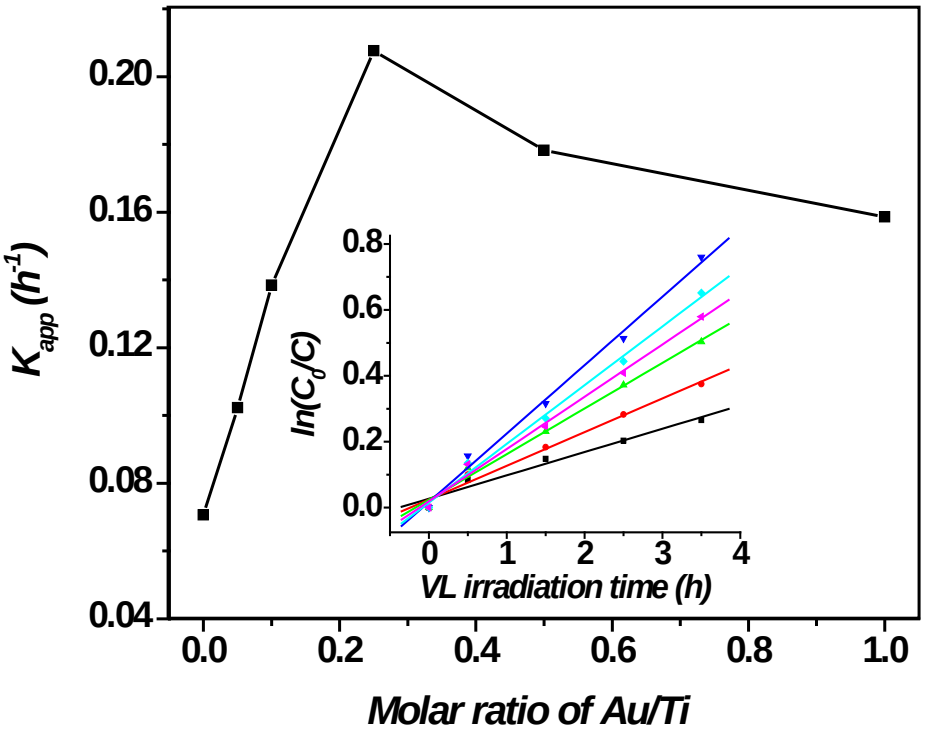

Figure 5.7 Effect of Au loading on the photocatalytic degradation of Orange II in aqueous solution.

5.2.7 Photocatalytic antibacterial activity under visible light irradiation

The photocatalytic antibacterial activity of Au-loaded TiO_2 NTs is measured by testing on *E. coli* (ATCC 700926). Without photocatalysts, no bactericidal effect is observed under VL illumination (see the Control curve in Figure 5.8).

Naked TiO_2 NT is found to show a slight photocatalytic antibacterial activity only at initial 0.5h illumination, which is unexpected due to its wide bandgap (3.2eV) and little capability of absorbing visible light. The probably reason is that the resulted nanotubular photocatalyst with abundance OH groups may adhere to the outer membrane of the *E.Coli* cells via weak hydrogen bonding so that some bacteria

cannot nourish from aqueous media, thus hindering the normal growth of bacteria and then achieving slight inactivation of *E. coli* (Elahifard et al., 2007).

An obvious bactericidal effect is observed on TiO_2-Au-0.25% nanotubular photocatalyst under VL illumination, which is consistent with its demonstrated VL absorption capability (Figure 5.5b, 400-700nm) and VL activity towards oxidation of Orange II dye (Figure 5.6). After 4h VL illumination, the concentration of survival *E. coli* drops sharply from 10^9 to 10^5 CFU/mL.

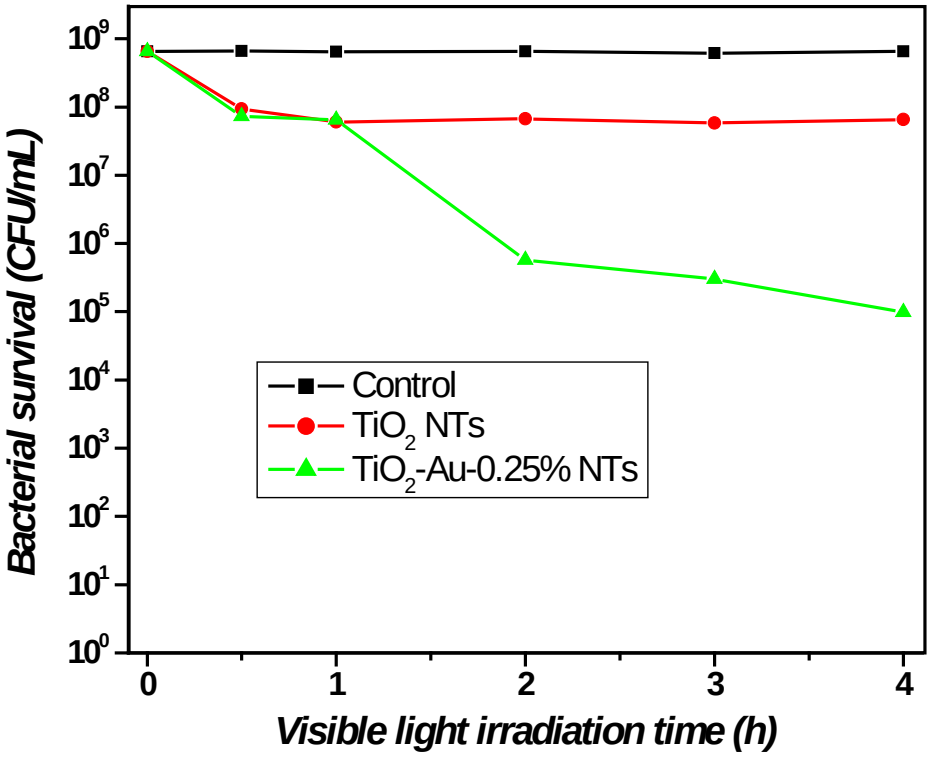

Figure 5.8 Photocatalytic inactivation of *E.coli* in solution containing (a) no catalyst, (b) TiO_2 NTs, and (c) TiO_2-Au-0.25% NTs under visible light irradiation. Experiment condition: batch reactor; light source: 350W Xenon light equipped with a 420nm cut-off filter; photocatalyst amount: 0.025g; initial concentration of *E.coli*: 10^8 to 10^9 CFU/mL.

5.2.8 Separation and cyclic usage test

In addition to the photocatalytic activity, the separation and the recycle usage of solid photocatalysts are also very important for the industrial applications. In this thesis project, the photocatalyst separation by sedimentation is evaluated. As can be seen from Figure 5.9 that TiO_2-Au-0.25% NTs and naked TiO_2 NTs precipitates almost completely within 5 h, resulting in a clear solution on the top and thus suggesting that our Au-loaded TiO_2 nanotubular photocatalysts can be easily separated from the reaction system by sedimentation. In contrast, it is difficult to separate commercial Degussa P25 powders from the reaction system by using sedimentation method. Besides, after decanting the supernatant carefully and subsequent drying at ambient temperature, TiO_2-Au-0.25% NTs and naked TiO_2 NTs could be recycled as high as 96.4% and 93.1%, respectively.

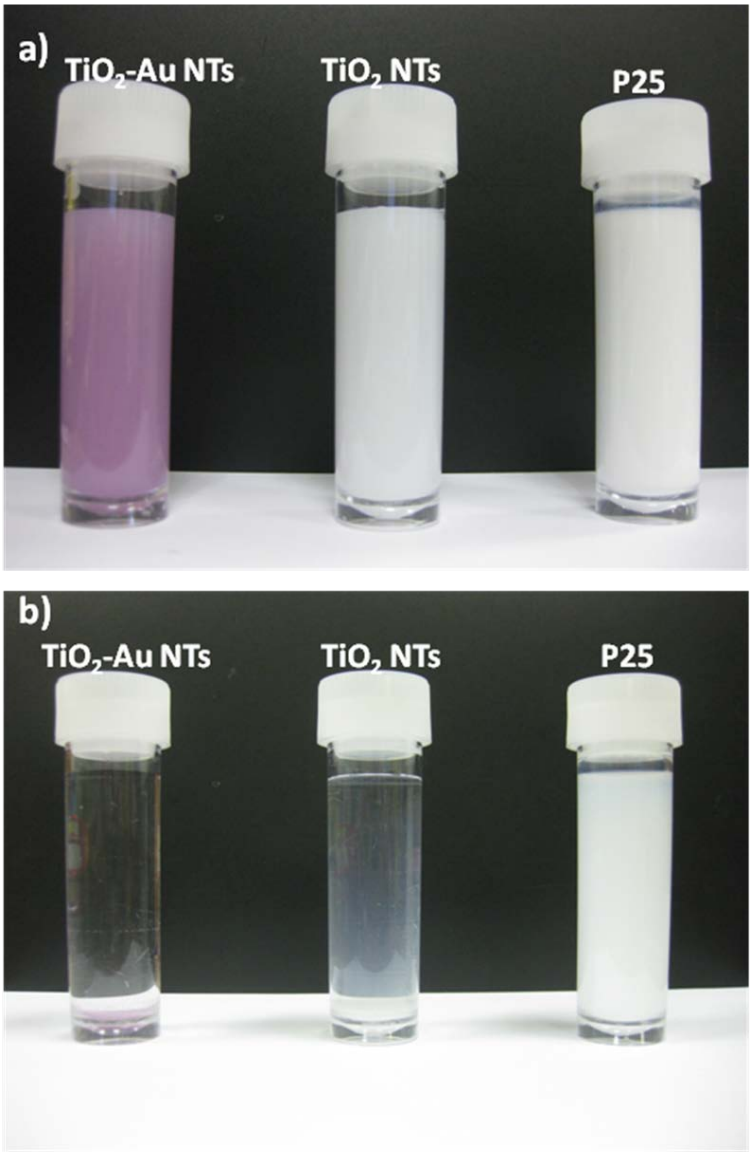

Figure 5.9 Sedimentation test of water solution containing photocatalysts TiO_2-Au-0.25% NTs, TiO_2 NTs and Degussa P25 at (a) t = 0 h and (b) t = 5h.

The cyclic usage experiments of the photocatalyst TiO_2-Au-0.25% NTs is carried out by photo-degradation of Orange II under VL illumination and the removal efficiency, representing the percentage of organic waste molecules destructed by TiO_2, after each run is plotted in Figure 5.10. The removal efficiency (or VL activity) of TiO_2-Au-0.25% nanotubular photocatalyst shows slight decrease from one run to another. After using four times, TiO_2-Au-0.25% lost about 19% of its photocatalytic activity. Note that two factors may account for this decrease of catalytic activity. First,

the intermediates generated in the last run will compete for the reactive oxygen species with the Orange II molecules in the current run. Second, the photocatalyst dosage is slightly decreased due to sampling for concentration analysis. However, in the fifth run, the removal efficiency decreases sharply and about 50% of its photocatalytic activity is lost. Thus it is concluded that our Au-loaded TiO_2 nanotubular photocatalysts is stable within 4 times recycle usage.

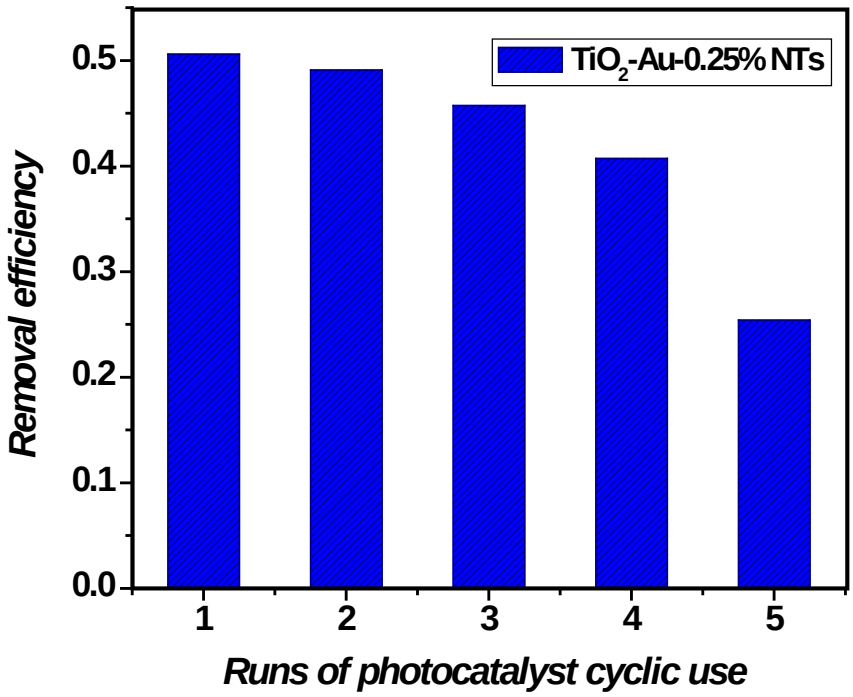

Figure 5.10 Cyclic usage experiments for photo-degradation of Orange II over TiO_2-Au-0.25% NTs under visible light illumination. Experiment condition: batch reactor; light source: 350W Xenon light equipped with a 420nm cut-off filter; catalyst amount: 1 g/L; initial concentration of Orange II: 5 ppm.

5.3 Summary

In this chapter, an environmental friendly one-pot hydrothermal method is successfully developed to synthesis visible-light-activated TiO_2-Au nanotubular photocatalysts without adding any reductant. After analyzing all the data of these TiO_2-Au nanotubes, several conclusions can be drawn as following:

1) Au ions can be reduced by supercritical water and then loaded onto titanate nanotubes under hydrothermal treatment;
2) The loading of Au nanoparticles on TiO_2 NTs obviously increases the specific surface area probably due to its effect on improving the nanotubular structures of TiO_2;
3) The synthesized TiO_2-Au NTs exhibits obvious enhanced visible light absorption capability and improved photocatalytic performance towards oxidation of Orange II dye as well as killing bacteria *E. Coli* under visible light irradiation. The optimal loading amount is found to be 0.25% (molar ratio of Au/Ti);
4) In addition, the prepared TiO_2-Au NTs can be easily separated from reaction medium within 5h, much better than Degussa P25, and not loss much photoactivity within four cycle reuse.

CHAPTER 6

CONCLUSIONS AND RECOMMENDATIONS

6.1 Conclusions

TiO_2-based photocatalysis is a promising and potential technique for waste water treatment. The subject of this master thesis project is thus to enhance the photocatalytic activity of TiO_2 photocatalysts by tuning the phase content or introducing guest metallic species. Some conclusions drawn from this thesis work are summarized below:

- A simple method of fabricating tri-crystalline mesoporous TiO_2 photocatalysts under strong acid environment was presented and the phase content could be tuned by changing the types and amounts of additives as well as the calcination temperatures. The additive urea had an effect on improving the mesoporous network and raising the anatase content via changing the PH value while the additive TTEA can be used to synthesis pure rutile. The tri-crystalline mesoporous TiO_2 with optimal phase content showed better photocatalytic activity towards photooxidation of Orange II than pure anatase, pure rutile and bicrystalline anatase-brookite samples probably due to phase junction effect, facilitating the separation of photoinduced electrons and holes and suppressing the recombination rate.
- Au nanoparticles deposited TiO_2 nanotubes were synthesized by a novel environmental friendly one-pot hydrothermal method under strong basic environment without adding any reductant. The synthesized TiO_2-Au NTs exhibited visible light absorption capability and improved photocatalytic

performance towards oxidation of Orange II dye as well as killing *E. Coli* under visible light irradiation (λ>420nm). The optimal loading amount was found to be 0.25% (molar ratio of Au/Ti). In addition, the prepared TiO_2-Au NTs could be easily separated from reaction medium within 5h by sedimentation, much better than commercial Degussa P25, and not loss much photoactivity within four cycle reuse.

6.2 Recommendations

The present work suggests that the modified TiO_2-based photocatalysts show quite promising results for the photo-degradation of organic wastes. However, much work is still needed to be conducted to make the process viable and efficient for commercial utilization. Therefore, some recommendations are proposed in the following section:

- Photocatalyst separation and reuse are two vital issues for the practical applications of TiO_2 photocatalysis. In present thesis work, the separation of TiO_2-Au composite photocatalysts by sedimentation and its cyclic reuse were studied and the results were really attractive. However, separation of mesoporous tri-crystalline TiO_2 powders involved in this thesis work is not easy and thus needed to be improved. Therefore, mesoporous tri-crystalline TiO_2 thin films are suggested and can be deposited onto the lamp, the light transmission medium, and/or the inside walls in the pilot scale reactor by employing dip coating or spin coating methods. As to its visible-light-activity, Ag nanoparticles thus can be considered due to its low price, strong antibacterial property as well as little harmful effect to human beings.

- Recently, graphene-based materials have been introduced into TiO_2 photocatalysts due to its many unique properties in order to enhance the photocatalytic performance under UV light or achieve visible light response. In future work, it is strongly suggested that the one-pot hydrothermal reduction method developed in this thesis work can be extended to fabricate graphene-TiO_2 nanotubes, or graphene-TiO_2-Au nanotubes. Besides, Fe or Ni nanoparticles loaded TiO_2 nanotubes should be attracted special attention due to its magnetic properties, which can be utilized in order to ease the separation and reuse of TiO_2 composite nanotubes for waste water treatment.

REFERENCES

Akhavan, O., E. Ghaderi. Photocatalytic reduction of graphene oxide nanosheets on TiO_2 thin film for photoinactivation of bacteria in solar light irradiation. J. Phys. Chem. C, 113, pp. 20214-20220. 2009.

Alberius, P. C. A., K. L. Frindell, R. C. Hayward, E. J. Kramer, G. D. Stucky, B. F. Chmelka. General predictive syntheses of cubic, hexagonal, and lamellar silica and titania mesostructured thin films. Chem. Mater., 14, pp. 3284-3294. 2002.

An, H., J. Li, J. Zhou, K. Li, B. Zhu, W. Huang. Iron-coated TiO_2 nanotubes and their photocatalytic performance. J. Mater. Chem., 20, pp. 603-610. 2010.

An, H. Q., B. L. Zhu, J. X. Li, J. Zhou, S. R. Wang, S. M. Zhang, S. H. Wu, W. P. Huang. Synthesis and characterization of thermally stable nanotubular TiO_2 and its photocatalytic activity. J. Phys. Chem. C, 112, pp. 18772-18775. 2008.

Anderson, M., H. Birkedal, N. R. Franklin, T. Ostomel, S. Boettcher, A. E. C. Palmqvist, G. D. Stucky. Ag/AgCl-loaded ordered mesoporous anatase for photocatalysis. Chem. Mater., 17, pp. 1409-1415. 2005.

Anderson, M. A., M. J. Gieselmann, Q. Y. Xu. Titania and alumina ceramic membranes. J. Membr. Sci., 39, pp. 243-258. 1988.

Anpo, M., M. Takeuchi. The design and development of highly reactive titanium oxide photocatalysts operating under visible light irradiation. J. Catal., 216, pp. 505-516. 2003.

Ardizzone, S., C. L. Bianchi, G. Cappelletti, S. Gialanella, C. Pirola, V. Ragaini. Tailored anatase/brookite nanocrystalline TiO_2. The optimal particle features for liquid- and gas-phase photocatalytic reactions. J. Phys. Chem. C, 111, pp. 13222-13231. 2007.

Armstrong, A. R., G. Armstrong, J. Canales, P. G. Bruce. TiO_2-B Nanowires. Angew. Chem., Int. Ed., 43, pp. 2286-2288. 2004.

Armstrong, G., A. R. Armstrong, J. Canales, P. G. Bruce. Nanotubes with the TiO_2-B structure. Chem. Commun., 41, pp. 2454-2456. 2005.

Asahi, R., T. Morikawa, T. Ohwaki, K. Aoki, Y. Taga. Visible-light photocatalysis in nitrogen-doped titanium oxides. Science, 293, pp. 269-271. 2001.

Awazu, K., M. Fujimaki, C. Rockstuhl, J. Tominaga, H. Murakami, Y. Ohki, N. Yoshida, T. Watanabe. A plasmonic photocatalyst consisting of silver nanoparticles embedded in titanium dioxide. J. Am. Chem. Soc., 130, pp. 1676-1680. 2008.

Bacsa, R. R., J. Kiwi. Effect of rutile phase on the photocatalytic properties of nanocrystalline titania during the degradation of p-coumaric acid. Appl. Catal. B: Environ., 16, pp. 19-29. 1998.

Bai, Y., W. Li, C. Liu, Z. Yang, X. Feng, X. Lu, K. Y. Chan. Stability of Pt nanoparticles and enhanced photocatalytic performance in mesoporous Pt-(anatase/TiO_2(B)) nanoarchitecture. J. Mater. Chem., 19, pp. 7055-7061. 2009.

Bannat, I., K. Wessels, T. Oekermann, J. Rathousky, D. Bahnemann, M. Wark. Improving the photocatalytic performance of mesoporous titania films by modification with gold nanostructures. Chem. Mater., 21, pp. 1645-1653. 2009.

Bartl, M. H., S. P. Puls, J. Tang, H. C. Lichtenegger, G. D. Stucky. Cubic mesoporous frameworks with a mixed semiconductor nanocrystalline wall structure and enhanced sensitivity to visible light. Angew. Chem., Int. Ed., 43, pp. 3037-3040. 2004.

Bavykin, D. V., F. C. Walsh. Elongated titanate nanostructures and their applications. Eur. J. Inorg. Chem., 8, pp. 977-997. 2009.

Bavykin, D. V., J. M. Friedrich, F. C. Walsh. Protonated titanates and TiO_2 nanostructured materials: synthesis, properties, and applications. Adv. Mater., 18, pp. 2807-2824. 2006.

Bavykin, D. V., V. N. Parmon, A. A. Lapkin, F. C. Walsh. The effect of hydrothermal conditions on the mesoporous structure of TiO_2 nanotubes. J. Mater. Chem., 14, pp. 3370-3377. 2004.

Bhattacharyya, A., S. Kawi, M. B. Ray. Photocatalytic degradation of orange II by TiO_2 catalysts supported on adsorbents. Cataly. Today, 98, pp. 431-439. 2004.

Bian, Z., J. Zhu, F. Cao, Y. Lu, H. Li. In situ encapsulation of Au nanoparticles in mesoporous core-shell TiO_2 microspheres with enhanced activity and durability. Chem. Commun., 45, pp. 3789-3791. 2009.

Bosc, F., A. Ayral, C. Guizard. Mesoporous anatase coatings for coupling membrane separation and photocatalyzed reactions. J. Membr. Sci., 265, pp. 13-19. 2005.

Butkus, M. A., M. Talbot, M. P. Labare. Feasibility of the silver-UV process for drinking water disinfection . Water Res., 39, pp. 4925-4932. 2005.

Carreon, M. A., S. Y. Choi, M. Mamak, N. Chopra, G. A. Ozin. Pore architecture affects photocatalytic activity of periodic mesoporous nanocrystalline anatase thin films. J. Mater. Chem., 17, pp. 82-89. 2007.

Chae, W. S., S. W. Lee, Y. R. Kim. Templating route to mesoporous nanocrystalline titania nanofibers. Chem. Mater., 17, pp. 3072-3074. 2005.

Chakraborty, A. K., Z. Qi, S. Y. Chai, C. Lee, S. Y. Park, D. J. Jang, W. I. Lee. Formation of highly crystallized TiO_2(B) and its photocatalytic behaviour. Appl. Catal. B: Environ., 93, 368-375. 2010.

Chandra, D., A. Bhaumik. Super-microporous TiO_2 synthesized by using new designed chelating structure directing agents. Microporous Mesoporous Mater., 112, pp. 533-541. 2008.

Chatterjee, D., S. Dasgupta. Visible light induced photocatalytic degradation of organic pollutants. J. Photochem. Photobiol. C: Photochem. Rev., 6, pp. 186-205. 2005.

Chen, D., D. Yang, Q. Wang, Z. Y. Jiang. Effects of boron doping on photocatalytic activity and microstructure of titanium dioxide nanoparticles. Ind. Eng. Chem. Res., 45, pp. 4110-4116. 2006.

Chen, D., F. Huang, Y. B. Cheng, R. A. Caruso. Mesoporous anatase TiO_2 beads with high surface areas and controllable pore sizes: A superior candidate for high-performance dye-sensitized solar cells. Adv. Mater., 21, pp. 2206-2210. 2009.

Chen, L., B. D. Yao, Y. Cao, K. N. Fan. Synthesis of well-ordered mesoporous titania with tuneable phase content and high photoactivity. J. Phys. Chem. C., 111, pp. 11849-11853. 2007.

Chen, X., C. Burda. The electronic origin of the visible-light absorption properties of C-, N- and S-doped TiO_2 nanomaterials. J. Am. Chem. Soc., 130, pp. 5018-5019. 2008.

Cheng, Y. J, J. S. Gutmann. Morphology phase diagram of ultrathin anatase TiO_2 films templated by a single PS-b-PEO block copolymer. J. Am. Chem. Soc., 128, pp. 4658-4674. 2006.

Choi, H., A. C. Sofranko, D. D. Dionysiou. Nanocrystalline TiO_2 photocatalytic membranes with a hierarchical mesoporous multilayer structure: synthesis, characterization, and multifunction. Adv. Funct. Mater., 16, pp. 1067-1074. 2006.

Choi, H., E. Stathatos, D. D. Dionysiou. Photocatalytic TiO_2 films and membranes for the development of efficient wastewater treatment and reuse systems. Desalination, 202, pp. 199-206. 2007.

Choi, H., E. Stathatos, D. D. Dionysiou. Sol-gel preparation of mesoporous photocatalytic TiO_2 films and TiO_2/Al_2O_3 composite membranes for environmental applications. Appl. Catal., B, 63, pp. 60-67. 2006.

Choi, W., A. Termin, M. R. Hoffmann. Effects of metal-ion dopants on the photocatalytic reactivity of quantum-sized TiO_2 particles. Angew. Chem., Int. Ed., 33, pp. 1091-1092. 1994.

Choi, W., A. Termin, M. R. Hoffmann. The role of metal ion dopants in quantum-sized TiO_2: Correlation between photoreactivity and charge carrier recombination dynamics. J. Phys. Chem., 98, pp. 13669-13679. 1994.

Clarke, J. B., J. W. Hastie, L. H. E. Kihlborg, R. Metselaar, M. M. Thackeray. Definitions of terms relating to phase transitions of the solid state. Pure Appl. Chem., 66, pp. 577-594. 1994.

Coronado, D. R., G. R. Gattorno, M. E. E. Pesqueira, C. de Coss, G. Oskam. Phase-pure TiO_2 nanoparticles: anatase, brookite and rutile. Nanotechnology, 19, 145605. 2008.

Cozzoli, P. D., R. Comparelli, E. Fanizza, M. L. Curri, A. Agostiano, D. Laub. Photocatalytic synthesis of silver nanoparticles stabilized by TiO_2 nanorods: A semiconductor/metal nanocomposite in homogeneous nonpolar solution. J. Am. Chem. Soc., 126, pp. 3868-3879. 2004.

Dambournet, D., L. Belharouak, K. Amine. Tailored preparation methods of TiO_2 anatase, rutile, brookite: Mechanism of formation and electrochemical properties. Chem. Mater., 22, pp. 1173-1179. 2010.

Di Paola, A., G. Cufalo, M. Addamo, M. Bellardita, R. Campostrini, Ischia, R. Ceccato, L. Palmisano. Photocatalytic activity of nanocrystalline TiO_2 (brookite, rutile and brookite-based) powders prepared by thermohydrolysis of $TiCl_4$ in aqueous chloride solutions. Colloid. Surf. A: Physicochem. Eng. Aspects, 317, pp. 366-376. 2008.

Ding, Z., G. Q. Lu, P. F. Greenfield. Role of the crystallite phase of TiO_2 in heterogeneous photocatalysis for phenol oxidation in water. J. Phys. Chem. B., 104, pp. 4815-4820. 2000.

Diwald, O., T. L. Thompson, T. Zubkov, E. G. Goralski, S. D. Walck, J. T. Yates Jr. Photochemical activity of nitrogen-doped rutile TiO_2 (110) in visible light. J. Phys. Chem. B., 108, pp. 6004-6008. 2004.

Dong, W., Y. Sun, C. W. Lee, W. Hua, X. Lu, Y. Shi, S. Zhang, J. Chen, D. Zhao. Controllable and repeatable synthesis of thermally stable anatase nanocrystal-silica composites with highly ordered hexagonal mesostructures. J. Am. Chem. Soc., 129, pp. 13894-13904. 2007.

Dong, X., J. Tao, Y. Li, H. Zhu. Enhanced photoelectrochemical properties of F-containing TiO_2 sphere thin film induced by its novel hierarchical structure. Appl. Surf. Sci., 255, pp. 7183-7187.2009.

Eiden-Assmann, S., J. Widoniak, G. Maret. Synthesis and characterization of porous and nonporous monodisperse colloidal TiO_2 particles. Chem. Mater., 16, pp. 6-11. 2004.

Elahifard, M. R., S. Rahimnejad, S Haghighi, M. R. Gholami. Apatite-coated $Ag/AgBr/TiO_2$ visible-light photocatalyst for destruction of bacteria. J. Am. Chem. Soc., 129, pp. 9552-9553. 2007.

Emeline, A. V., N. V. Sheremetyeva, V. N. Kuznetsov, V. K. Ryabchuk, N. Serpone. Photoinduced formation of defects and nitrogen stabilization of color centers in N-doped titanium dioxide. J. Phys. Chem. C., 111, pp. 11456-11462. 2007.

Fujishima A., K. Honda. Electrochemical photolysis of water at a semiconductor electrode. Nature, 238, pp. 37-38. 1972.

Galusha, J. W., C. K. Tsung, G. D. Stucky, M. H. Bartl. Optimizing sol-gel infiltration and processing methods for the fabrication of high-quality planar titania inverse opals. Chem. Mater., 20, pp. 4925-4930. 2008.

Gayaa, U. I., A. H. Abdullah. Heterogeneous photocatalytic degradation of organic contaminants over titanium dioxide: A review of fundamentals, progress and problems. J. Photochem. Photobiol. C: Photochem. Rev., 9, pp. 1-12. 2008.

Geim, A. K., K. S.Novoselov. The rise of graphene. Nat. Mater., 6, pp. 183-191. 2007.

Gong, D., C. A. Grimes, O. K. Varghese, W. Hu, R. S. Singh, Z. Chen, E. C. Dickey. Titanium oxide nanotube arrays prepared by anodic oxidation. J. Mater. Res., 16, pp. 3331-3334. 2001.

Gopal, N. O., H. H. Lo, S. C. Ke. Chemical state and environment of boron dopant in B,N-codoped anatase TiO_2 nanoparticles: An avenue for probing diamagnetic dopants in TiO_2 by electron paramagnetic resonance spectroscopy. J. Am. Chem. Soc., 130, pp. 2760-2761. 2008.

Gopinath, C. S. Comment on "Photoelectron spectroscopic investigation of nitrogen-doped titania nanoparticles". J. Phys. Chem. B., 110, pp. 7079-7080. 2006.

Grandcolas, M. A. Louvet, N. Keller, V. Keller. Layer-by-layer deposited titanate-based nanotubes for solar photocatalytic removal of chemical warfare agents from textiles. Angew. Chem. Int. Ed., 48, pp. 161-164. 2009.

Grätzelare, M. Photoelectrochemical cells. Nature, 414, pp. 338-344. 2001.

Groenewolt, M., T. Brezesinski, H. Schlaad, M. Antonietti, P. W. Groh, B. Ivan. Polyisobutylene-block-poly(ethylene oxide) for robust templating of highly ordered mesoporous materials. Adv. Mater., 17, pp. 1158-1162. 2005.

Grosso, D., G. Soler-Illia, E. L. Crepaldi, B. Charleux, C. Sanchez. Nanocrystalline transition-metal oxide spheres with controlled multi-scale porosity. Adv. Funct. Mater., 13, pp. 37-42. 2003.

Grosso, D., G. Soler-Illia, F. Babonneau, C. Sanchez, P. A. Albouy, A. Brunet-Bruneau, A. R. Balkenende. Highly organized mesoporous titania thin films showing mono-oriented 2D hexagonal channels. Adv. Mater., 13, pp. 1085-1090. 2001.

Herrmann, J. M. Heterogeneous photocatalysis: Fundamentals and applications to the removal of various types of aqueous pollutants. Cataly. Today, 53, pp. 115-129. 1999.

Hirakawa, T., P. V. Kamat. Charge separation and catalytic activity of $Ag@TiO_2$ core-shell composite clusters under UV-irradiation. J. Am. Chem. Soc., 127, pp. 3928-3934. 2005.

Hirakawa, T., P. V. Kamat. Photoinduced electron storage and surface plasmon modulation in $Ag@TiO_2$ clusters. Langmuir, 20, pp. 5645-5647. 2004.

Hoffmann, M. R., S. T. Martin, W. Choi, D. W. Bahnemannt. Environmental applications of semiconductor photocatalysis. Chem. Rev., 95, pp. 69-96. 1995.

Hu, C., J. Guo, J. Qu, X. Hu. Photocatalytic degradation of pathogenic bacteria with AgI/TiO_2 under visible light irradiation. Langmuir, 23, pp. 4982-4987. 2007.

Hu, C., Y. Lan, J. Qu, X. Hu, A. Wang. Ag/AgBr/TiO_2 visible light photocatalyst for destruction of azo dyes and bacteria. J. Phys. Chem. B., 110, pp. 4066-4072. 2006.

Hummers, W. S., R. E. Offeman. Preparation of graphitic oxide. J. Am. Chem. Soc., 80, pp. 1339-1340. 1958.

Hwang, Y. K., K. C. Lee, Y. U. Kwon, Nanoparticle routes to mesoporous titania thin films. Chem. Commun., 37, pp. 1738-1379. 2001.

Imhof, A., D. J. Pine. Ordered macroporous materials by emulsion templating. Nature, 389, pp. 948-951. 1997.

In, S., A. Orlov, R. Berg, F. García, S. P. Jimenez, M. S. Tikhov, D. S. Wright, R. M. Lambert. Effective visible light-activated B-doped and B,N-codoped TiO_2 photocatalysts. J. Am. Chem. Soc., 129, pp. 13790-13791. 2007.

Inumaru, K., T. Kasahara, M. Yasui, S. Yamanak. Direct nanocomposite of crystalline TiO_2 particles and mesoporous silica as a molecular selective and highly active photocatalyst. Chem. Commun., 41, pp. 2131-2133. 2005.

Iskandar, F., A. B. D. Nandiyanto, K. M. Yun, C. J. Hogan Jr., K. Okuyama, P. Biswas. Enhanced photocatalytic performance of brookite TiO_2 macroporous particles prepared by spray drying with colloidal templating. Adv. Mater., 19, pp. 1408-1412. 2007.

Ismail, A. A., D. W. Bahnemann, L. Robben, V. Yarovyi, M. Wark. Palladium doped porous titania photocatalysts: Impact of mesoporous order and crystallinity. Chem. Mater., 22, pp. 108-116. 2010.

Jiang, Z., F. Yang, N. Luo, B. T. T. Chu, D. Sun, H. Shi, T. Xiao, P. P. Edwards. Solvothermal synthesis of N-doped TiO_2 nanotubes for visible-light-responsive photocatalysis. Chem. Commun., 44, pp. 6372-6374. 2008.

Jin, M., X. Zhang, S. Shunsuke, Z. Liu, D. A. Tryk, A. V. Emeline, T. Murakami, A. Fujishima. Light-stimulated composition conversion in TiO_2-based nanofibers. J. Phys. Chem. C, 111, pp. 658-665. 2007.

Kasuga, T., M. Hiramatsu, A. Hoson, T. Sekino, K. Niihara. Formation of titanium oxide nanotube. Langmuir, 14, pp. 3160-3163. 1998.

Kasuga, T., M. Hiramatsu, A. Hoson, T. Sekino, K. Niihara. Titania nanotubes prepared by chemical processing. Adv. Mater., 11, pp. 1307-1311.1999.

Kawahara, T., Y. Konishi, H. Tada, N. Tohge, J. Nishii, S. Ito. A patterned TiO_2 (anatase)/TiO_2 (rutile) bilayer-type photocatalyst: Effect of the anatase/rutile junction on the photocatalytic activity. Angew. Chem. Int. Ed., 41, pp. 2811-2813. 2002.

Kim, S. H., S. Y. Kwak, B. H. Sohn, T. H. Park. Design of TiO_2 nanoparticle self-assembled aromatic polyamide thin-film-composite (TFC) membrane as an approach to solve biofouling problem. J. Membr. Sci., 211, pp. 157-165. 2003.

Kim, S. S., H. I. Lee, J. K. Shon, J. Y. Hur, M. S. Kang, S. S. Park, S. S. Kong, J. A. Yu, M. Seo, D. H. Li, S. S. Thakur, J. M. Kim. Preparation of highly ordered mesoporous TiO_2 materials with crystalline framework from different mesostructured silica templates via nanoreplication. Chem. Lett., 37, pp. 140-141. 2008.

Kim, Y. J., M. H. Lee, H. J. Kim, G. Lim, Y. S. Choi, N. G. Park, K. Kim, W. I. Lee. Formation of highly efficient dye-sensitized solar cells by hierarchical pore generation with nanoporous TiO_2 spheres. Adv. Mater., 21, pp. 3668-3673. 2009.

Kiyonaga, T., T. Mitsui, M. Torikoshi, M. Takekawa, T. Soejima, H. Tada. Ultrafast photosynthetic reduction of elemental sulfur by Au nanoparticle-loaded TiO_2. J. Phys. Chem. B, 110, pp. 10771-10778. 2006.

Körösi, L., S. Papp, I. Bertóti, I. Dékány. Surface and bulk composition, structure, and photocatalytic activity of phosphate-modified TiO_2. Chem. Mater., 19, pp. 4811-4819. 2007.

Kresge, C. T., M. E. Leonowicz, W. J. Roth, J. C. Vartuli, J. S. Beck. Ordered mesoporous molecular sieves synthesized by a liquid-crystal template mechanism. Nature, 359, pp. 710-712. 1992.

Kubacka, A., M. L. Cerrada, C. Serrano, M. Fernández-Garcia, M. Ferrer, M. Fernández-Garcia. Plasmonic nanoparticle/polymer nanocomposites with enhanced photocatalytic antimicrobial properties. J. Phys. Chem. C., 113, pp. 9182-9190. 2009.

Kumar, A., P. K. Vemula, P. M. Ajayan, G. John. Silver-nanoparticle-embedded antimicrobial paints based on vegetable oil. Nat. Mater., 7, pp. 236-247. 2008.

Kuznetsov, V. N., N. Serpone. Visible light absorption by various titanium dioxide specimens. J. Phys. Chem. B., 110, pp. 25203-25209. 2006.

Kwak, S. Y., S. H. Kim, S. S. Kim. Hybrid organic/inorganic reverse osmosis (RO) membrane for bactericidal anti-fouling. 1. preparation and characterization of TiO_2 nanoparticle self-assembled aromatic polyamide thin-film-composite (TFC) membrane. Environ. Sci. Technol., 35, pp. 2388-2394. 2001.

Lambert, T. N., C. A. Chavez, B. Hernandez-Sanchez, P. Lu, N. S. Bell, A. Ambrosini, T. Friedman, T. J. Boyle, D. R. Wheeler, D. L. Huber. Synthesis and characterization of titania-graphene nanocomposites. J. Phys. Chem. C, 113, pp. 19812-19823. 2009.

Lan, Y., X. P. Gao, H. Y. Zhu, Z. F. Zheng, T. Y. Yan, F. Wu, S. P. Ringer, D. Y. Song. Titanate nanotubes and nanorods prepared from rutile powder. Adv. Funct. Mater., 15, pp. 1310-1318. 2005.

Lee, J., M. C. Orilall, S. C. Warren, M. Kamperman, F. J. DiSalvo, U. Wiesner. Direct access to thermally stable and highly crystalline mesoporous transition-metal oxides with uniform pores. Nat. Mater., 7, pp. 222-228. 2008.

Li, B., X. Zhang, X. Li, L. Wang, R. Han, B. Liu, W. Zheng, X. Li, Y. Liu. Photo-assisted preparation and patterning of large-area reduced graphene oxide-TiO_2 conductive thin film. Chem. Commun., 46, pp. 3499-3501. 2010.

Li, C. Y., Y. Z. Wan, J. Wang, Y. L. Wang, X. Q. Jiang, L. M. Han. Antibacterial pitch-based activated carbon fiber supporting silver. Carbon, 36, pp. 61-65. 1998.

Li, D., H. Haneda, S. Hishita, N. Ohashi. Visible-light-driven N-F-codoped TiO_2 photocatalysts. 1. Synthesis by spray pyrolysis and surface characterization. Chem. Mater., 17, pp. 2588-2595. 2005.

Li, D., H. Haneda, S. Hishita, N. Ohashi. Visible-light-driven N-F-codoped TiO_2 photocatalysts. 2. Optical characterization, photocatalysis, and potential application to air purification. Chem. Mater., 17, pp. 2596-2602. 2005.

Li, D., H. Zhou, I. Honma. Design and synthesis of self-ordered mesoporous nanocomposite through controlled in-situ crystallization. Nat. Mater., 3, pp. 65-72. 2004.

Li, G., L. Wang, L. Lv, X. S. Zhao. Preparation and characterization of SiO_2/TiO_2-Pt core/shell nanostructures and evaluation of their photocatalytic activity. J. Nanosci Nanotechnol., 9, pp. 177-184. 2009.

Li, G., X. S. Zhao. Characterization and photocatalytic properties of titanium-containing mesoporous SBA-15. Ind. Eng. Chem. Res., 45, pp. 3569-3573. 2006.

Li, G., X. S. Zhao, M. B. Ray. Advanced oxidation of orange II using TiO_2 supported on porous adsorbents: The role of pH, H_2O_2 and O_3. Sep. Purif. Technol., 55, pp. 91-97. 2007.

Li, H. X., Z. F. Bian, J. Zhu, Y. N. Huo, H. Li, Y. F. Lu. Mesoporous Au/TiO_2 nanocomposites with enhanced photocatalytic activity. J. Am. Chem. Soc., 129, pp. 4538-4539. 2007.

Li, J. S., D. L. Shieh, D. Y. Li, C. H. Ho, S. J. Yang, J. L. Lin. Photodegradation of CH_3I on mesoporous TiO_2-B nanofibers with Au nanoparticles. Appl. Surf. Sci., 254, pp. 4655-4664. 2008.

Li, Q., Y. W. Li, P. Wu, R. Xie, J. K. Shang. Palladium oxide nanoparticles on nitrogen-doped titanium oxide: Accelerated photocatalytic disinfection and post-illumination catalytic ‘‘memory’’. Adv. Mater., 20, pp. 3717-3724. 2008.

Li, Q., Y. W. Li, Z. Liu, R. Xie, J. K. Shang. Memory antibacterial effect from photoelectron transfer between nanoparticles and visible light photocatalyst. J. Mater. Chem., 20, pp. 1068-1072. 2010.

Li, W., C. Liu, Y. X. Zhou, Y. Bai, X. Feng, Z. H. Yang, L. H. Lu, X. H. Lu, K. Y. Chan. Enhanced photocatalytic activity in anatase/TiO_2(B) core-shell nanofiber. J. Phys. Chem. C, 112, pp. 20539-20545. 2008.

Li, X., Y. Xiong, Z. Li, Y. Xie. Large-scale fabrication of TiO_2 hierarchical hollow spheres. Inorg. Chem., 45, pp. 3493-3495. 2006.

Li, Y., H. Zhang, Z. Guo, J. Han, X. Zhao, Q. Zhao, S. J. Kim. Highly efficient visible-light-induced photocatalytic activity of nanostructured AgI/TiO_2 photocatalyst. Langmuir, 24, pp. 8351-8357. 2008.

Linsebigler, A. L., G. Q. Lu, J. T. Yates, Jr. Photocatalysis on TiO_2 surface: Principles, mechanisms, and selected results. Chem. Rev., 95, pp.735-758. 1995.

Liu, G., Y. Zhao, C. Sun, F. Li, G. Q. Lu, H. M. Cheng. Synergistic effects of B/N doping on the visible-light photocatalytic activity of mesoporous TiO_2. Angew. Chem. Int. Ed., 47, pp. 4516-4520. 2008.

Liu, J., M. Li, J. Wang, Y. Song, L. Jiang, T. Murakami, A. Fujishima. Hierarchically macro-/mesoporous Ti-Si oxides photonic crystal with highly efficient photocatalytic capability. Environ. Sci. Technol., 43, pp. 9425-9431. 2009.

Liu, S. M., L. M. Gan, L. H. Liu, W. D. Zhang, H. C. Zeng. Synthesis of single-crystalline TiO_2 nanotubes. Chem. Mater., 14, pp. 1391-1397. 2002.

Liu, Y., L. Chen, J. Hu, J. Li, R. Richards. TiO_2 nanoflakes modified with gold nanoparticles as photocatalysts with high activity and durability under near UV irradiation. J. Phys. Chem. C, 114, pp. 1641-1645. 2010.

Liu, Y., X. Wang, F. Yang, X. Yang. Excellent antimicrobial properties of mesoporous anatase TiO_2 and Ag/TiO_2 composite films. Microporous Mesoporous Mater., 114, pp. 431-439. 2008.

Liu, Z., D. D. Sun, P. Guo, J. O. Leckie. One-step fabrication and high photocatalytic activity of porous TiO_2 hollow aggregates by using a low-temperature hydrothermal method without templates. Chem. Eur. J., 13, pp. 1851-1855. 2007.

Luo, H. M., C. Wang, Y. S. Yan. Synthesis of mesostructured titania with controlled crystalline framework. Chem. Mater., 15, pp. 3841-3846. 2003.

Lyu, Y. Y., S. H. Yi, J. K. Shon, S. Chang, L. S. Pu, S. Y. Lee, J. E. Yie, K. Char, G. D. Stucky, J. M. Kim. Highly stable mesoporous metal oxides using nano-propping hybrid gemini surfactants. J. Am. Chem. Soc., 126, pp. 2310-2311. 2004.

Maekawa, H., J. Esquena, S. Bishop, C. Solans, B. F. Chmelka. Meso/macroporous inorganic oxide monoliths from polymer foams. Adv. Mater., 15, pp. 591-596. 2003.

Martinez-Ferrero, E., Y. Sakatani, C. Boissiere, D. Grosso, A. Fuertes, J. Fraxedas, C. Sanchez. Nanostructured titanium oxynitride porous thin films as efficient visible-active photocatalysts. Adv. Funct. Mater., 17, pp. 3348-3354. 2007.

Matsunaga, T., R. Tomoda, T. Nakajima, H. Wake. Photoelectrochemical sterilization of microbial cells by semiconductor powders. FEMS Microbiol. Lett., 29, pp. 211-214. 1985.

Mills, A., S. K. Lee, A. Lepre. Photodecomposition of ozone sensitised by a film of titanium dioxide on glass. J. Photochem. Photobiol. A: Chem., 155, pp. 199-205. 2003.

Mitoraj, D., H. Kisch. The nature of nitrogen-modified titanium dioxide photocatalysts active in visible light. Angew. Chem. Int. Ed., 47, pp. 9975-9978. 2008.

Molinari, R., M. Mungari, E. Drioli, A. Di Paola, V. Loddo, L. Palmisano, M. Schiavello. Study on a photocatalytic membrane reactor for water purification. Catal. Today, 55, pp. 71-78. 2000.

Nagase, T., T. Ebina, T. Iwasaki, H. Hayashi, Y. Onodera, M. Chatterjee. Hydrothermal synthesis of brookite. Chem. Lett., 28, pp. 911-912. 1999.

Ng, Y. H., I. V. Lightcap, K. Goodwin, M. Matsumura, P. V. Kamat. To what extent do graphene scaffolds improve the photovoltaic and photocatalytic response of TiO_2 nanostructured films? J. Phys. Chem. Lett., 1, pp. 2222-2227. 2010.

Nieto-Suarez, M., G. Palmisano, M. L. Ferrer, M. C. Gutierrez, S. Yurdakal, V. Augugliaro, M. Pagliaro, F. del Monte. Self-assembled titania-silica-sepiolite based nanocomposites for water decontamination. J. Mater. Chem., 19, pp. 2070-2075. 2009.

Oguma, K., H. Katayama, S. Ohgaki. Photoreactivation of Escherichia coli after low- or medium-pressure UV disinfection determined by an endonuclease sensitive site assay. Appl. Environ. Microbiol., 68, pp. 6029-6035. 2002.

Orilall, M. C., N. M. Abrams, J. Lee, F. J. DiSalvo, U. Wiesner. Highly crystalline inverse opal transition metal oxides via a combined assembly of soft and hard chemistries. J. Am. Chem. Soc., 130, pp. 8882-8883. 2008.

Ortel, E., S. Sokolov, R. Kraehnert. Influence of steel substrate roughness on morphology and mesostructure of TiO_2 porous layers produced by template-assisted dip coating. Microporous Mesoporous Mater., 127, pp. 17-24.2010.

Ozawa, T., M. Iwasaki, H. Tada, T. Akita, K. Tanaka, S. Ito. Low-temperature synthesis of anatase-brookite composite nanocrystals: The junction effect on photocatalytic activity. J. Colloid Interface Sci. 281, pp. 510-513. 2005.

Page, K., M. Wilson, I. P. Parkin. Antimicrobial surfaces and their potential in reducing the role of the inanimate environment in the incidence of hospital-acquired infections. J. Mater. Chem., 19, pp. 3819-3831. 2009.

Page, K., R. G. Palgrave, I. P. Parkin, M. Wilson, S. L. P. Savinc, A. V. Chadwick. Titania and silver-titania composite films on glass—potent antimicrobial coatings. J. Mater. Chem., 17, pp. 95-104. 2007.

Palmisano, L., A. Sclafani. Thermodynamics and Kinetics for Heterogeneous Photocatalytic Processes. In Heterogeneous Photocatalysis, ed. by M. Schiavello, pp.109-132. New York: Wiley, 1997.

Pan, J. H., W. I. Lee. Preparation of highly ordered cubic mesoporous WO_3/TiO_2 films and their photocatalytic properties. Chem. Mater., 18, pp. 847-853. 2006.

Pan, J. H., X. Zhang, A. J. Du, D. D. Sun, J. O. Leckie. Self-etching reconstruction of hierarchically mesoporous F-TiO_2 hollow microspherical photocatalyst for concurrent membrane water purifications. J. Am. Chem. Soc., 130, pp. 11256-11257. 2008.

Peng, T., D. Zhao, K. Dai, W. Shi, K. Hirao. Synthesis of titanium dioxide nanoparticles with mesoporous anatase wall and high photocatalytic activity. J. Phys. Chem. B., 109, pp. 4947-4952. 2005.

Peng, W., Z. Wang, N. Yoshizawa, H. Hatoria, T. Hirotsub. Lamellar carbon nanosheets function as templates for two-dimensional deposition of tubular titanate. Chem. Commun., 44, pp. 4348-4350. 2008.

Perathoner, S., P. Lanzafame, R. Passalacqua, G. Centi, R. Schlogl, D. S. Su. Use of mesoporous SBA-15 for nanostructuring titania for photocatalytic applications. Microporous Mesoporous Mater., 90, pp. 347-361. 2006.

Qiu, X., Y. Zhao, C. Burda. Synthesis and characterization of nitrogen-doped group IVB visible-light-photoactive metal oxide nanoparticles. Adv. Mater., 19, pp.3995-3999. 2007.

Reddy, E. P., B. Sun, P. G. Smirniotis. Transition metal modified TiO_2-loaded MCM-41 catalysts for visible- and UV-light driven photodegradation of aqueous organic pollutants .J. Phys. Chem. B, 108, pp. 17198-17205. 2004.

Riss, A., M. J. Elser, J. Bernardi, O. Diwald. Stability and photoelectronic properties of layered titanate nanostructures. J. Am. Chem. Soc., 131, pp. 6198-6206. 2009.

Sakai, H., T. Kanda, H. Shibata, T. Ohkubo, M. Abe. Preparation of highly dispersed core/shell-type titania nanocapsules containing a single Ag nanoparticle. J. Am. Chem. Soc., 128, pp. 4944-4945. 2006.

Sakatani, Y., D. Grosso, L. Nicole, C. Boissiere, G. Soler-Illia, C. Sanchez. Optimised photocatalytic activity of grid-like mesoporous TiO_2 films: Effect of crystallinity, pore size distribution, and pore accessibility. J. Mater. Chem., 16, pp. 77-82. 2006.

Sakthivel, S., H. Kisch. Daylight photocatalysis by carbon-modified titanium dioxide. Angew. Chem. Int. Ed., 42, pp. 4908-4911. 2003.

Sanchez, C., C. Boissiere, D. Grosso, C. Laberty, L. Nicole. Design, synthesis, and properties of inorganic and hybrid thin films having periodically organized nanoporosity. Chem. Mater., 20, pp. 682-737. 2008.

Scotti, R., I. R. Bellobono, C. Canevali, C. Cannas, M. Catti, M. D'Arienzo, A. Musinu, S. Polizzi, M. Sommariva, A. Testino, F. Morazzoni. Sol-gel pure and mixed-phase titanium dioxide for photocatalytic purposes: Relations between phase composition, catalytic activity, and charge-trapped sites. Chem. Mater., 20, pp. 4051-4061. 2008.

Serpone, N. Is the band gap of pristine TiO_2 narrowed by anion- and cation-doping of titanium dioxide in second-generation photocatalysts? J. Phys. Chem. B., 110, pp. 24287-24293. 2006.

Shannon, M. A., P. W. Bohn, M. Elimelech, J. G. Georgiadis, B. J. Marin, A. M. Mayes. Science and technology for water purification in the coming decades. Nature, 452, pp. 301-310. 2008.

Sing, K. S. W., D. H. Everett, R. A. W. Haul, L. Moscou, R. A. Pierotti, J. Rouquerol, T. Siemieniewska. Reporting physisorption data for gas/solid systems with special reference to the determination of surface area and porosity. Pure Appl. Chem., 57, pp. 603-619. 1985.

Soler-Illia, G., C. Sanchez. Interactions between poly(ethylene oxide)-based surfactants and transition metal alkoxides: their role in the templated construction of mesostructured hybrid organic-inorganic composites. New J. Chem., 24, pp. 493-499. 2000.

Soler-Illia, G., C. Sanchez, B. Lebeau. J. Patarin. Chemical strategies to design textured materials: from microporous and mesoporous oxides to nanonetworks and hierarchical structures. Chem. Rev., 102, pp. 4093-4138. 2002.

Soni, S. S., M. J. Henderson, J. F. Bardeau, A. Gibaud. Visible-light photocatalysis in titania-based mesoporous thin films. Adv. Mater., 20, pp. 1493-1498. 2008.

Srinivasan, M., T. White. Degradation of methylene blue by three-dimensionally ordered macroporous titania. Environ. Sci. Technol., 41, pp. 4405-4409. 2007.

Subramanian, V., E. E. Wolf, P. V. Kamat. Influence of metal/metal ion concentration on the photocatalytic activity of TiO_2-Au composite nanoparticles. Langmuir, 19, pp. 469-474. 2003.

Sugimoto, T., T. Kojima. Formation mechanism of amorphous TiO_2 spheres in organic solvents. 1. roles of ammonia. J. Phys. Chem. C, 112, pp. 18760-18771. 2008.

Sun, X., C. Zheng, M. Qiao, J. Yan, X. Wang, N. Guan. Bioinspired synthesis of hierarchical macro-mesoporous titania with tuneable macroporous morphology using cell-assemblies as macrotemplates. Chem. Commun., 45, pp. 4750-4752. 2009.

Sun, X., Y. Li. Synthesis and characterization of ion-exchangeable titanate nanotubes. Chem. Eur. J., 9, pp. 2229-2238.2003.

Tada, H., T. Mitsui, T. Kiyonaga, T. Akita, K. Tanaka. All-solid-state Z-scheme in CdS-Au-TiO_2 three-component nanojunction system. Nat. Mater., 5, pp. 782-786. 2006.

Tanaka, S., D. Nogami, N. Tsuda, Y. Miyake. Synthesis of highly-monodisperse spherical titania particles with diameters in the submicron range. J. Colloid Interface Sci., 334, pp. 188-194. 2009.

Tang, J., Y. Y. Wu, E. W. McFarland, G. D. Stucky. Synthesis and photocatalytic properties of highly crystalline and ordered mesoporous TiO_2 thin films. Chem. Commun., 40, pp. 1670-1671. 2004.

Thiel, J., L. Pakstis, S. Buzby, M. Raffi, C. Ni, D. J. Pochan, S. I. Shah. Antibacterial properties of silver-doped titania. Small, 3, pp. 799-803. 2007.

Tian, B., X. Liu, B. Tu, C. Yu, J. Fan, L. W, S. Xie, G. D. Stucky, D. Y. Zhao. Self-adjusted synthesis of ordered stable mesoporous minerals by acid-base pairs. Nat. Mater., 2, pp. 159-163. 2003.

Tian, G. H., H. G. Fu, L. Q. Jing, B. F. Xin, K. Pan. Preparation and characterization of stable biphase TiO_2 photocatalyst with high crystallinity, large surface area, and enhanced photoactivity. J. Phys. Chem. C., 112, pp. 3083-3089. 2008.

Toledo-Antonio, J. A., M. A. Cortes-Jácome, C. Angeles-Chavez, E. López-Salinas, P. Quintana. Highly quasi-monodisperse Ag nanoparticles on titania nanotubes by impregnative aqueous ion exchange. Langmuir, 25, pp. 10195-10201. 2009.

Toledo Antonio, J. A., M. A. Cortes-Jácome, S. L. Orozco-Cerros, E. Montiel-Palacios, R. Suarez-Parra, C. Angeles-Chavez, J. Navarete, E. López-Salinas. Assessing optimal photoactivity on titania nanotubes using different annealing temperatures. Appl. Catal., B, 100, pp. 47-54. 2010.

Torres, G. R., T. Lindgren, J. Lu, C. G. Granqvist, S. E. indquist. Photoelectrochemical study of nitrogen-doped titanium dioxide for water oxidation. J. Phys. Chem. B., 108, pp. 5995-6003. 2004.

Tryba, B., A. W. Morawski, M. Inagaki. Application of TiO_2-mounted activated carbon to the removal of phenol from water. Appl. Catal. B: Environ., 41, pp. 427-433. 2003.

Tsung, C. K., J. Fan, N. F. Zheng, Q. H. Shi, A. J. Forman, J. F. Wang, G. D. Stucky. A general route to diverse mesoporous metal oxide submicrospheres with highly crystalline frameworks. Angew. Chem., Int. Ed., 47, pp. 8682-8686. 2008.

Umebayashi, T., T. Yamki, H. Itoh, K. Asai. Band gap narrowing of titanium dioxide by sulfur doping. Appl. Phys. Lett., 81, pp. 454-456. 2002.

Usseglio, S., A. Damin, D. Scarano, S. Bordiga, A. Zecchina, C. Lamberti. $(I_2)_n$ encapsulation inside TiO_2: A way to tune photoactivity in the visible region. J. Am. Chem. Soc., 129, pp. 2822-2828. 2007.

Wan, Y., D. Y. Zhao. On the controllable soft-templating approach to mesoporous silicates. Chem. Rev., 107, pp. 2821-2860. 2007.

Wang, C., C. Shao, Y. Liu, X. Li. Water-dichloromethane interface controlled synthesis of hierarchical rutile TiO_2 superstructures and their photocatalytic properties. Inorg. Chem., 48, pp. 1105-1113. 2009.

Wang, D., D. Choi, J. Li, Z. Yang, Z. Nie, R. Kou, D. Hu, C. Wang, L. V. Saraf, J. Zhang, I. A. Aksay, J. Liu. Self-assembled TiO_2-graphene hybrid nanostructures for enhanced Li-ion insertion. ACS Nano, 3, pp. 907-914. 2009.

Wang, J. Q., J. F. Wang, Q. L. Sun, W. Wang, Z. Y. Yan, W. J. Gong, L. Min. UV and solar light degradation of dyes over mesoporous crystalline titanium dioxides prepared by using commercial synthetic dyes as templates. J. Mater. Chem., 19, pp. 6597-6604. 2009.

Wang, M. L., C. H. Wang, W. Wang. Porous macrobeads composed of metal oxide nanocrystallites and with percolated porosity. J. Mater. Chem., 17, pp. 2133-2138. 2007.

Wang, X. C., J. C. Yu, C. M. Ho, A. C. Mak. A robust three-dimensional mesoporous Ag/TiO_2 nanohybrid film. Chem. Commun., 17, pp. 2262-2264. 2005.

Wang, X. C., J. C. Yu, C. M. Ho, Y. D. Hou, X. Z. Fu. Photocatalytic activity of a hierarchically macro/mesoporous titania. Langmuir, 21, pp. 2552-2559. 2005.

Wang, X. C., J. C. Yu, H. Y. Yip, L. Wu, P. K. Wong, S. Y. Lai. A mesoporous Pt/TiO_2 nanoarchitecture with catalytic and photocatalytic functions. Chem. Eur. J., 11, pp. 2997-3004. 2005.

Wang, X. C., J. C. Yu, Y. D. Hou, X. Z. Fu. Three-dimensionally ordered mesoporous molecular-sieve films as solid superacid photocatalysts. Adv. Mater., 17, pp. 99-102. 2005.

Wang, Y., L. Zhang, K. Deng, X. Chen, Z. Zou. Low temperature synthesis and photocatalytic activity of rutile TiO_2 nanorod superstructures. J. Phys. Chem. C, 111, pp. 2709-2714. 2007.

Wang, Z. Y., F. X. Zhang, Y. L. Yang, B. Xue, J. Cui, N. J. Guan. Facile postsynthesis of visible-light-sensitive titanium dioxide/mesoporous SBA-15. Chem. Mater., 19, pp. 3286-3293. 2007.

Wei, J., J. Yao, X. Zhang, W. Zhu, H. Wang, M. J. Rhodes. Hydrothermal growth of titania nanostructures with tuneable phase and shape. Mater. Lett., 61, pp. 4610-4613. 2007.

Williams, G., B. Seger, P. V. Kamat. TiO_2-graphene nanocomposites. UV-assisted photocatalytic reduction of graphene xxide. ACS Nano, 2, pp. 1487-1491. 2008.

Wu, Y., H. Liu, J. Zhang, F. Chen. Enhanced photocatalytic activity of nitrogen-doped titania by deposited with gold. J. Phys. Chem. C, 113, pp. 14689-14695. 2009.

Xie, Y., K. Ding, Z. Liu, R. Tao, Z. Sun, H. Zhang, G. An. In situ controllable loading of ultrafine noble metal particles on titania. J. Am. Chem. Soc., 131, pp. 6648-6649. 2009.

Xu, H., F. Jia, Z. Ai, L. Zhang. A general soft interface platform for the growth and assembly of hierarchical rutile TiO_2 nanorods spheres. Cryst. Growth Des., 7, pp. 1216-1219. 2007.

Xu, Y. M., C. H. Langford. Enhanced photoactivity of a titanium (IV) oxide supported on ZSM5 and Zeolite A at low coverage. J. Phys. Chem., 99, pp. 11501-11507. 1995.

Xu, Y. M., C. H. Langford. Photoactivity of titanium dioxide supported on MCM-41, Zeolite X and Zeolite Y. J. Phys. Chem. B, 101, pp. 3115-3121. 1997.

Yan, M. C., F. Chen, J. L. Zhang, M. Anpo. Preparation of controllable crystalline titania and study on the photocatalytic properties. J. Phys. Chem. B., 109, pp. 8673-8678. 2005.

Yang, D. J., H. W. Liu, Z. F. Zheng, Y. Yuan, J. C. Zhao, E. R. Waclawik, X. B. Ke, H. Y. Zhu. An efficient photocatalyst structure: TiO_2(B) nanofibers with a shell of anatase nanocrystals. J. Am. Chem. Soc., 131, pp. 17885-17893. 2009.

Yang, H. G., H. C. Zeng. Creation of intestine-like interior space for metal-oxide nanostructures with a quasi-reverse emulsion. Angew. Chem., Int. Ed., 43, pp. 5206-5209. 2004.

Yang, H. G., H. C. Zeng. Preparation of hollow anatase TiO_2 nanospheres via ostwald ripening. J. Phys. Chem. B, 108, pp. 3492-3495. 2004.

Yang, K., Y. Dai, B. Huang, M. H. Whangbo. Density functional characterization of the band edges, the band gap states, and the preferred doping sites of halogen-doped TiO_2. Chem. Mater., 20, pp. 6528-6534. 2008.

Yang, P. D., D. Y. Zhao, D. I. Margolese, B. F. Chmelka, G. D. Stucky. Generalized syntheses of large-pore mesoporous metal oxides with semicrystalline frameworks. Nature, 396, pp. 152-155. 1998.

Yang, P. D., D. Y. Zhao, D. I. Margolese, B. F. Chmelka, G. D. Stucky. Block copolymer templating syntheses of mesoporous metal oxides with large ordering lengths and semicrystalline framework. Chem. Mater., 11, pp. 2813-2826. 1999.

Yoshitake, H., T. Sugihara, T. Tatsumi. Preparation of wormhole-like mesoporous TiO_2 with an extremely large surface area and stabilization of its surface by chemical vapor deposition. Chem. Mater., 14, pp. 1023-1029. 2002.

Yu, J., J. Xiong, B. Cheng, S. Liu. Fabrication and characterization of Ag-TiO_2 multiphase nanocomposite thin films with enhanced photocatalytic activity. Appl. Catal. B: Environ., 60, pp. 211-221. 2005.

Yu, J., S. Liu, H. Yu, Microstructures and photoactivity of mesoporous anatase hollow microspheres fabricated by fluoride-mediated self-transformation. J. Catal., 249, pp. 59-66. 2007.

Yu, J. C., J. Yu, W. Ho, L. Zhang. Preparation of highly photocatalytic active nano-sized TiO_2 particles via ultrasonic irradiation. Chem. Commun., 37, pp. 1942-1943. 2001.

Yu, J. C., J. Yu, W. Ho, Z. Jiang, L. Zhang. Effects of F^- doping on the photocatalytic activity and microstructures of nanocrystalline TiO_2 powders. Chem. Mater., 14, pp. 3808-3816. 2002.

Yu, J. C., L. Zhang, J. Yu. Direct sonochemical preparation and characterization of highly active mesoporous TiO_2 with a bicrystalline framework. Chem. Mater., 14, pp. 4647-4653. 2002.

Yu, J. C., W. K. Ho, J. G. Yu, S. K. Hark, K. Iu. Effects of trifluoroacetic acid modification on the surface microstructures and photocatalytic activity of mesoporous TiO_2 thin films. Langmuir, 19, pp. 3889-3896. 2003.

Yu, J. C., X. C. Wang, L. Wu, W. K. Ho, L. Z. Zhang, G. T. Zhou. Sono- and photochemical routes for the formation of highly dispersed gold nanoclusters in mesoporous titania films. Adv. Funct. Mater., 14, pp. 1178-1183. 2004.

Yu, J. C., X. C. Wang, X. Z. Fu. Pore-wall chemistry and photocatalytic activity of mesoporous titania molecular sieve films. Chem. Mater., 16, pp. 1523-1530. 2004.

Yuan, Z. Y., T. Z. Ren, B. L. Su. Hierarchically mesostructured titania materials with an unusual interior macroporous structure. Adv. Mater., 15, pp. 1462-1465. 2003.

Yue, W. B., X. X. Xu, J. T. S. Irvine, P. S. Attidekou, C. Liu, H. Y. He, D. Y. Zhao, W. Z. Zhou. Mesoporous monocrystalline TiO_2 and its solid-state electrochemical properties. Chem. Mater., 21, pp. 2540-2546. 2009.

Yun, H. S., K. Miyazawa, H. S. Zhou, I. Honma, M. Kuwabara. Synthesis of mesoporous thin TiO_2 films with hexagonal pore structures using triblock copolymer templates. Adv. Mater., 13, pp. 1377-1380. 2001.

Zhang, F., Y. Pi, J. Cui, Y. Yang, X. Zhang, N. Guan. Unexpected selective photocatalytic reduction of nitrite to nitrogen on silver-doped titanium dioxide. J. Phys. Chem. C, 111, pp. 3756-3761. 2007.

Zhang, F., Y. Zheng, Y. Cao, C. Chen, Y. Zhan, X. Lin, Q. Zheng, K. Wei, J. Zhu. Ordered mesoporous Ag-TiO_2-KIT-6 heterostructure: synthesis, characterization and photocatalysis. J. Mater. Chem., 19, pp. 2771-2777. 2009.

Zhang, H., G. Chen, D. W. Bahnemann. Photoelectrocatalytic materials for environmental applications. J. Mater. Chem., 19, pp. 5089-5121. 2009.

Zhang, H., J. F. Banfield. Understanding polymorphic phase transformation behaviour during growth of nanocrystalline aggregates: Insights from TiO_2. J. Phys. Chem. B., 104, pp. 3481-3487. 2000.

Zhang, H., X. Lv, Y. Li, Y. Wang, J. Li. P25-graphene composite as a high performance photocatalyst. ACS Nano, 4, pp. 380-386. 2010.

Zhang, J., Q. Xu, Z. C. Feng, M. J. Li, C. Li. Importance of the relationship between surface phases and photocatalytic activity of TiO_2. Angew. Chem. Int. Ed., 47, pp. 1766-1769. 2008.

Zhang, X., J. H. Pan, A. J. Du, P. F. Lee, D. D. Sun, J. O. Leckie. Aggregating TiO_2(B) nanowires to porous basketry-like microspheres and their photocatalytic properties. Chem. Lett., 37, pp. 424-425. 2008.

Zhang, Y., J. Li, J. Wang, Substrate-assisted crystallization and photocatalytic properties of mesoporous TiO_2 thin films. Chem. Mater., 18, pp. 2917-2923. 2006.

Zhao, Q., M. Li, J. Chu, T. Jiang, H. Yin. Preparation, characterization of Au (or Pt)-loaded titania nanotubes and their photocatalytic activities for degradation of methyl orange. Appl. Surf. Sci., 255, pp. 3773-3778. 2009.

Zheng, Z., B. Huang, X. Qin, X. Zhang, Y. Bai, M. Jiang, P. Wang, M. H. Whangbo. Highly efficient photocatalyst: TiO_2 microspheres produced from TiO_2 nanosheets with a high percentage of reactive {001} facets. Chem. Eur. J., 15, pp. 12576-12579. 2009.

Zhou, J., L. Lv, J. Yu, H. L. Li, P. Z. Guo, H. Sun, X. S. Zhao. Synthesis of self-organized polycrystalline F-doped TiO_2 hollow microspheres and their photocatalytic activity under visible light. J. Phys. Chem. C, 112, pp. 5316-5321. 2008.

Zhou, J., M. Takeuchi, A. K. Ray, M. Anpo, X. S. Zhao. Enhancement of photocatalytic activity of P25 TiO_2 by vanadium-ion implantation under visible light irradiation. J. Colloid Interface Sci., 311, pp. 497-501. 2007.

Zhou, J., M. Takeuchi, X. S. Zhao, A. K. Ray, M. Anpo. Photocatalytic decomposition of formic acid under visible light irradiation over V-ion-implanted TiO_2 thin film photocatalysts prepared on quartz substrate by ionized cluster beam (ICB) deposition method. Catal. Lett., 106, pp. 67-70. 2006.

Zhou, J., Y. Zhang, X. S. Zhao, A. K. Ray. Photodegradation of benzoic acid over metal-doped TiO_2. Ind. Eng. Chem. Res., 45, pp. 3503-3511. 2006.

Zhou, Y., Q. Bao, L. A. L. Tang, Y. Zhong, K. P. Loh. Hydrothermal dehydration for the “green” reduction of exfoliated graphene oxide to graphene and demonstration of tuneable optical limiting properties. Chem. Mater., 21, pp. 2950-2956. 2009.

Zhu, C., S. Guo, P. Wang, L. Xing, Y. Fang, Y. Zhai, S. Dong. One-pot, water-phase approach to high-quality graphene/TiO_2 composite nanosheets. Chem. Commun., 46, pp. 7148-7150. 2010.

APPENDIX

List of publications during my Master Candidature

(1) Porous photocatalysts for advanced water purifications (*an invited review article*). Pan JH, **Dou H**, Xiong Z, Xu C, Ma J and Zhao XS. ***Journal of Materials Chemistry***, 2010, 20, 4512-4528.

(2) Synthesis of mesoporous anatase TiO_2 with a combined template method and photocatalysis. Xiong Z, **Dou H**, Pan JH, Ma J, Xu C and Zhao XS. ***CrystEngComm***, in press.